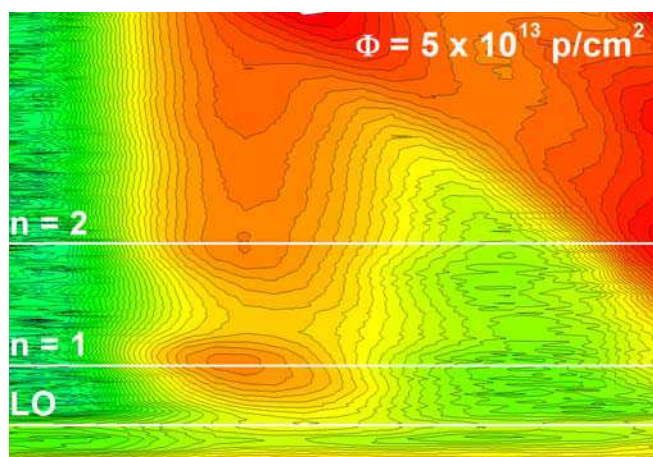




Ana Margarida Rocha
de Oliveira Cavaco

**Defeitos de Irradiação em Estruturas Quânticas de
Semicondutores A_3B_5**

**Radiation-Induced Defects in Quantum-Size
Structures of A_3B_5 Semiconductors**





**Ana Margarida Rocha
de Oliveira Cavaco**

**Defeitos de Irradiação em Estruturas Quânticas de
Semicondutores A_3B_5**

**Radiation-Induced Defects in Quantum-Size
Structures of A_3B_5 Semiconductors**

Dissertação apresentada à Universidade de Aveiro para cumprimento dos requisitos necessários à obtenção do grau de Doutor em Física, realizada sob a orientação científica da Professora Doutora Maria Celeste do Carmo, Professora Catedrática do Departamento de Física da Universidade de Aveiro e do Professor Doutor Nikolai Andreevich Sobolev, Professor Associado do Departamento de Física da Universidade de Aveiro.

Apoio financeiro da FCT no âmbito da
bolsa SFRH/BD/1264/2000.

Financially supported by FCT in the
framework of the bursary
SFRH/BD/1264/2000.

o júri

presidente

Doutor José Manuel Lopes da Silva Moreira
professor catedrático da Universidade de Aveiro

Doutor Axel Hoffmann
professor catedrático do Instituto de Física do Estado Sólido da Universidade Técnica de Berlim,
Alemanha

Doutor Mikhail Igorevich Vasilevskiy
professor catedrático da Universidade do Minho

Doutor Eduardo Jorge da Costa Alves
investigador principal, coordenador da Unidade de Física e Aceleradores do Instituto Tecnológico e Nuclear

Doutora Maria Celeste da Silva Carmo
professora catedrática da Universidade de Aveiro

Doutor Nikolai Andreevich Sobolev
professor associado da Universidade de Aveiro

To my husband and daughter,

Cavaco and Ana Filipe;

To my parents,

Vitor and Jãe;

And my brother,

Rui.

Não é o desafio
que define quem somos
nem o que somos capazes de fazer.
O que nos define é o modo
como enfrentamos esse desafio.

Richard Bach

Nada ao Acaso

.

acknowledgments

I would like to start by saying that during the last years many people contributed to the development of this thesis. I would like to thank to some of them explicitly, and apologize to all those who should also been mentioned. First of all, I want to thank Professor Celeste Carmo and Professor Nikolai Sobolev for the opportunity to develop this work being supervised by both, for the confidence and support.

To Professor Dieter Bimberg and Professor Axel Hoffmann from the Institute of Solid State Physics of the Technical University of Berlin for the possibility of developing experimental work within the Institute and for the supply of samples, and to all research group, namely Robert Heitz[†], Frank Heinrichsdorff, Harald Born, Sven Rodt, Roman Sellin and Florian Guffarth.

To Professor Marius Grundmann from the Institute of Experimental Physics II of the University of Leipzig and his group, namely Jens Bauer and Marc Schillgalies, for fruitful discussions and the opportunity to perform experimental work within the group.

I enjoyed a very fruitful cooperation with Professor Mikhail Vasilevskiy and Adil Chahboun from the Physics Department of the University of Minho and Dr. Nikolay Baidus from N.I. Lobachevsky State University from Nizhni Novgorod. My regards to them and thanks for supplying the samples.

Many friends and colleagues have contributed with their companionship during these years. My special thanks to Rosário and Clarisse.

To all my friends outside university for their steady support, friendship and patience in the past ten years and all my entire life. My special thanks to Maria and Bi.

I gratefully acknowledge a personal grant over a period of four years from the “Fundação para a Ciência e a Tecnologia” and additional travel support in several cases.

palavras-chave

semicondutores, estruturas quânticas, defeitos de irradiação, espectroscopia óptica

resumo

As estruturas quânticas de semicondutores, nomeadamente baseadas em GaAs, têm tido nos últimos vinte anos um claro desenvolvimento. Este desenvolvimento deve-se principalmente ao potencial tecnológico que estas estruturas apresentam. As aplicações espaciais, em ambientes agressivos do ponto de vista do nível de radiação a que os dispositivos estão sujeitos, motivaram todo o desenrolar de estudos na área dos defeitos induzidos pela radiação.

As propriedades dos semicondutores e dos dispositivos de semicondutores são altamente influenciadas pela presença de defeitos estruturais, em particular os induzidos pela radiação. As propriedades dos defeitos, os processos de criação e transformação de defeitos devem ser fortemente alterados quando se efectua a transição entre o semicondutor volumico e as heteroestruturas de baixa dimensão.

Este trabalho teve como principal objectivo o estudo de defeitos induzidos pela radiação em estruturas quânticas baseadas em GaAs e InAs. Foram avaliadas as alterações introduzidas pelos defeitos em estruturas de poços quânticos e de pontos quânticos irradiadas com electrões e com prótons.

A utilização de várias técnicas de espectroscopia óptica, fotoluminescência, excitação de fotoluminescência e fotoluminescência resolvida no tempo, permitiu caracterizar as diferentes estruturas antes e após a irradiação.

Foi inequivocamente constatada uma maior resistência à radiação dos pontos quânticos quando comparados com os poços quânticos e os materiais volumicos. Esta resistência deve-se principalmente a uma maior localização da função de onda dos portadores com o aumento do confinamento dos mesmos. Outra razão provável é a expulsão dos defeitos dos pontos quânticos para a matriz.

No entanto, a existência de defeitos na vizinhança dos pontos quânticos promove a fuga dos portadores dos níveis excitados, cujas funções de onda são menos localizadas, provocando um aumento da recombinação não-radiativa e, conseqüentemente, uma diminuição da intensidade de luminescência dos dispositivos.

O desenvolvimento de um modelo bastante simples para a estatística de portadores fora de equilíbrio permitiu reproduzir os resultados de luminescência em função da temperatura. Os resultados demonstraram que a extinção da luminescência com o aumento da temperatura é determinada por dois factores: a redistribuição dos portadores minoritários entre os pontos quânticos, o poço quântico e as barreiras de GaAs e a diminuição na taxa de recombinação radiativa relacionada com a dependência, na temperatura, do nível de Fermi dos portadores majoritários.

keywords

semiconductors, quantum-size structures, radiation-induced defects, optical spectroscopy

abstract

Quantum size semiconductor structures, namely those based on GaAs, have experienced an outstanding development in the past twenty years. This development is mainly due to the technological potential these structures present. Space-based telecommunications in harsh radiation environments motivated a run off of studies in the field of radiation-induced defects.

Semiconductor properties and semiconductor device performance are highly influenced by the presence of structural defects, particularly those induced by irradiation. Properties as well as processes of creation and transformation of defects are expected to be substantially modified when moving from a bulk semiconductor to corresponding low-dimensionality structures.

The main goal of this work was to study the radiation-induced defects in quantum-size heterostructures composed of GaAs and InAs. The changes introduced by radiation defects have been evaluated in structures comprising quantum dots and quantum wells subjected to irradiation with electron and protons.

The use of several optical spectroscopy techniques, namely photoluminescence, photoluminescence excitation and time-resolved photoluminescence, allowed the characterization of different structures in the as-grown and irradiated state.

A higher radiation hardness of the quantum dots as compared to quantum wells and corresponding bulk materials has been clearly established. This higher resistance is mainly due to the higher localization of the carrier wavefunction with increasing confinement. Another probable reason is the expulsion of mobile defects into the surrounding barrier material.

However, the existence of defects in the neighbourhood of the quantum dots promotes tunnel escape of carriers from the excited dot states, whose wavefunctions are less localized, to the defects, causing an increase in the non-radiative recombination and, consequently, a decrease in device luminescence.

A rather simple model for the carrier statistics out of equilibrium which reproduces quite well the luminescence results as a function of temperature allowed to demonstrate that the quantum dot photoluminescence quenching with increasing temperature is determined by two factors: the minority carrier redistribution between the quantum dots, quantum well and GaAs barriers, and the decrease in the radiative recombination rate related to the temperature dependence of the Fermi level of the majority carriers.

List of publications

A. Chahboun, M.I. Vasilevskiy, N.V. Baidus, A. Cavaco, N.A. Sobolev, M.C. Carmo, E. Alves, B.N. Zvonkov, “*Further insight into the temperature quenching of photoluminescence from InAs/GaAs self-assembled quantum dots*”, Journal of Applied Physics 103, 083548 (2008).

A. Chahboun, N. V. Baidus, P. B. Demina, B. N. Zvonkov, M. J. M. Gomes, A. Cavaco, N. A. Sobolev, M. C. Carmo, and M. I. Vasilevskiy, “*Influence of matrix defects on the photoluminescence of InAs self-assembled quantum dots*”, Physica Status Solidi (a) 203, 1348-1352 (2006).

A. Cavaco, M.C. Carmo, N.A. Sobolev, F. Guffarth, H. Born, R. Heitz, A. Hoffmann, D. Bimberg, “*Intradot carrier relaxation in radiation-damaged InGaAs/GaAs quantum dot heterostructures*”, in: Physics, Chemistry and Application of Nanostructures, World Scientific (Singapore), p.111 (2003).

A. Cavaco, N.A. Sobolev, M.C. Carmo, F. Guffarth, H. Born, R. Heitz, A. Hoffmann, D. Bimberg, “*Carrier dynamics in particle-irradiated InGaAs/GaAs quantum dots*”, Physica Status Solidi (c) 0, 1177 (2003).

N.A. Sobolev, A. Cavaco, M.C. Carmo, M. Grundmann, F. Heinrichsdorff, D. Bimberg, “*Enhanced Radiation Hardness of InAs/GaAs Quantum Dot Structures*”, Physica Status Solidi (b) 224 (1), 93 (2001).

N.A. Sobolev, A. Cavaco, M.C. Carmo, H. Born, M. Grundmann, F. Heinrichsdorff, R. Heitz, A. Hoffmann, D. Bimberg, “*Influence of electron irradiation on carrier recombination and intradot relaxation in InGaAs/GaAs quantum dot*

structures”, in: Physics, Chemistry and Application of Nanostructures, World Scientific (Singapore), p.146 (2001).

List of symbols and acronyms

2D	Two-Dimensional
3D	Three-Dimensional
AFM	Atomic Force Microscopy
AlAs	Aluminium Arsenide
AlGaAs	Aluminium Gallium Arsenide
AP-MOVPE	Atmospheric Pressure Metal-Organic Vapour Phase Epitaxy
Ar	Argon
As _i	Arsine Interstitial
CCl ₄	Tetrachloromethane
CdSe	Cadmium Selenide
CL	Cap layer
CQW	Coupled Quantum Wells
CW	Continuous wave
EBIC	Electron Beam Induced Current
FTIR	Fourier Transform Infrared
FWHM	Full Width at Half Maximum
GaAs	Gallium Arsenide
Ga _i	Gallium Interstitial
GaSb	Gallium Antimonide
Ge	Germanium
GS	Ground State
He	Helium
He-Ne	Helium-Neon
InAs	Indium Arsenide
InGaAs	Indium Gallium Arsenide
InGaAsP	Indium Gallium Arsenide Phosphide
InP	Indium Phosphide

InSb	Indium Antimonide
LD	Laser Diode
LED	Light Emitting Diode
LO	Longitudinal Optical
MBE	Molecular Beam Epitaxy
MCP	Multi-channel Plate
ML	Monolayer
Mn	Manganese
MOCVD	Metal-Organic Chemical Vapour Deposition
OPO	Optical Parametric Oscillator
PD	Photodiode
PL	Photoluminescence
PLE	Photoluminescence Excitation
QD	Quantum Dot
QW	Quantum Well
QWR	Quantum Wire
RHEED	Reflection High-Energy Electron Diffraction
RT	Room Temperature
SAQD	Self-Assembled Quantum Dot
Si	Silicon
SK	Stranski-Krastanow
SRIM	Stopping and Range of Ions in Matter
Te	Tellurium
TEGa	Triethylgallium
TEM	Transmission Electron Microscopy
Ti	Titanium
TMAI	Trimethylaluminium
TMGa	Trimethylgallium
TMIn	Trimethylindium
TRIM	Transport of Ions in Matter
TRPL	Time-Resolved Photoluminescence
TU	Technical University
UHV	Ultra-High Vacuum
UV	Ultra-Violet
V_{As}	Arsine Vacancy
V_{Ga}	Gallium Vacancy

V-I	Vacancy-Interstitial
VCSEL	Vertical-Cavity Surface-Emitting Laser
WL	Wetting Layer
XSTM	Cross-sectional Scanning Tunnelling Microscopy

List of Figures

2.1	Zincblende structure	6
2.2	Band offsets	8
2.3	Density of states for charge carriers in structures with different dimensionality	9
2.4	Schematic representation of energy levels in a single atom, a bulk semiconductor and a quantum dot	10
2.5	Variation of the formation energy of a substitutional Mn impurity in a CdSe nanocrystal as a function of the nanocrystal diameter	14
2.6	Changes in minority-carrier diffusion length	15
2.7	Maximum and average energy transmitted to a silicon atom as a function of the incident energy for electrons, protons and neutrons	16
2.8	TRIM simulations of the depth distribution of the displaced target atoms and implanted atoms	17
2.9	Simulation of the penetration of hydrogen atoms in GaAs	18
3.1	Different growth modes of crystal epilayers on lattice-mismatched substrates	24
3.2	Schematic diagram of a MOCVD growth reactor used for III-V semiconductors growth.	25
3.3	Simplified schematic of the MOCVD setup of the Aix machine used at the Institute of Solid State Physics of the Technical University of Berlin, Germany	29

3.4	Scheme of doping from a bulk elementary source by pulsed laser sputtering in AP-MOVPE process used at the University of Nizhny Novgorod, Russia	30
3.5	Experimental setup for PL measurements using a grating spectrometer	33
3.6	Experimental setup for PL measurements using a Fourier transform infrared spectrometer	34
3.7	Diagram illustrating the photon energy ranges of the sources available for resonant excitation	37
3.8	Schematic representation of the setup used at the Institute of Solid State Physics of the Technical University of Berlin for the PLE experiments	38
3.9	Schematic representation of the setup used, at the Institute of Solid State Physics of the Technical University of Berlin, for the TRPL experiments	39
3.10	The infrared laser system, at the Institute of Solid State Physics of the Technical University of Berlin, for the TRPL experiments	40
4.1	Layer sequence of the laser structure samples	45
4.2	PL spectra of laser heterostructures samples	46
4.3	Gaussian fit of QD PL peak	47
4.4	Temperature dependence of the PL characteristics for the as-grown samples 1×QD, CQW and 5×QD	48
4.5	Layer sequence of the samples with non-uniform WL thickness	50
4.6	Plan view TEM image of sample TU3581.	51
4.7	PL spectrum of the as-grown sample TU5330 taken at 10 K	52
4.8	PL spectrum of the as-grown sample TU5330 taken at 70 K	52
4.9	PL spectrum of the as-grown sample TU5330 taken at 300 K	53
4.10	PL spectra of the as-grown sample TU4738	54
4.11	PL spectra of non-uniform WL thickness samples taken at 10 K	55
4.12	PL and PLE spectra and contour plot of the as-grown sample TU5330 taken at 7 K	56

4.13	Temperature dependence of the integrated PL intensity for different identified QD and WL emissions for the as-grown sample TU5330. . . .	57
4.14	Layer sequence of the sample TU5411	58
4.15	PL spectrum of the as-grown sample TU5411 taken at 10 K	59
4.16	PL spectrum of the as-grown sample TU5411 taken at 300 K	59
4.17	PL spectrum of the as-grown sample TU5411 taken at 300 K	60
4.18	Layer sequence of the samples with different cap layer thicknesses . . .	61
4.19	PL spectra of thin cap layer samples	62
4.20	QD ground state transition energy at room temperature vs. GaAs cap layer thickness.	63
4.21	Temperature dependence results of sample, NN3760, with 10 nm cap layer thickness	64
4.22	PL spectra of thin cap layer samples with different QW thickness and In content in QW	65
4.23	PL spectra of thin cap layer samples with different QW thickness and In content in QW	66
4.24	PLE spectra of samples with different cap layer thickness	67
4.25	PL and PLE spectra of thin cap layer samples with different QW In content	68
4.26	Layer sequence of the samples from CCl ₄ treatment	69
4.27	PL spectra of samples from the # 41 series taken at 12 K	70
4.28	PL spectra of two similar samples taken at 12 K, showing the influence of the CCl ₄ treatment on the QD PL emission.	71
4.29	Temperature dependence of the QD PL emission from samples of the # 41 series. Sample characteristics and labels are according to table 4.2 .	71
5.1	FTIR PL spectra of samples 1×QD, CQW and 5×QD measured at 10 K	80
5.2	PL spectra of samples 1×QD, CQW and 5×QD after irradiation	82
5.3	Plots of k/k_0 vs. electron irradiation fluence for the laser structure samples	83

5.4	Plots of k/k_0 vs. electron irradiation fluence for the laser structure samples at different temperatures	84
5.5	PL spectra of the as-grown sample TU3904 ($1\times$ QD) taken at 10 K for several excitation powers.	85
5.6	Linear fit of the integrated PL intensity vs. excitation power for the as-grown sample TU3904 in order to determine the parameter k	85
5.7	PL spectra of sample TU5330 taken at 10 K after irradiation	86
6.1	Schematic diagram illustrating carrier capture from GaAs barrier into a QD via the wetting layer and carrier relaxation within the QD.	92
6.2	Rise and decay times from TRPL measurements of sample TU5411.	96
6.3	PL and PLE spectra of sample TU5411.	97
6.4	PL and PLE spectra of sample TU5330.	99
6.5	Contour plots of the QD PL intensity for the as-grown and proton-irradiated sample TU5330.	100
6.6	PL transients taken at 2 K of the as-grown and electron-irradiated samples	102
6.7	PL transients taken at 2 K of as-grown and electron-irradiated samples upon resonant excitation	103
6.8	PLE spectra of sample $1\times$ QD for various electron irradiation fluences	104
7.1	Temperature dependence, from 10 to 300 K, of the PL of samples $1\times$ QD (TU3904), as-grown and irradiated	110
7.2	Arrhenius plots of the PL intensity for samples $1\times$ QD (TU3904), as-grown and irradiated. The irradiation fluence is indicated on the graph.	111
7.3	PL spectra of QD/QW heterostructures: NN4190 and NN4184	112
7.4	Temperature dependence of the integrated PL intensity for an as-grown and two proton-irradiated NN4190 samples.	113
7.5	Temperature dependence of the integrated PL intensity for an as-grown and two proton-irradiated NN4184 samples.	114
7.6	Temperature dependence of the integrated PL intensity for the as-grown NN4190 samples for two different excitation densities.	114

7.7	Model band structure of the GaAs/GaInAs(QW)/InAs(QD) heterostructure.	116
7.8	Temperature dependence of I_{QD} and I_{QW} calculated for several defect concentrations	123
7.9	Temperature dependence of I_{QD} and I_{QW} calculated for for different excitation intensities	124
7.10	Temperature dependence of I_{QD} calculated for two different excitation powers of a he-Ne laser and for resonant excitation through the QW . .	124

List of Tables

2.1	Properties of GaAs and InAs	5
3.1	Major differences between MBE and MOCVD growth techniques	26
4.1	Sample characteristics	60
4.2	Sample characteristics	69
6.1	TRPL rise and decay times of proton-irradiated sample	95
6.2	TRPL rise and decay times of electron-irradiated samples upon above-bandgap excitation	103
6.3	TRPL rise and decay times of electron-irradiated samples upon resonant excitation	104
7.1	Material parameters used in the calculations	122

Contents

List of Publications	i
List of symbols and acronyms	iii
List of figures	xi
List of tables	xiii
1 Introduction	1
2 State of the art	5
2.1 Properties of InAs/GaAs heterostructures	5
2.1.1 GaAs and InAs	5
2.1.2 Band offsets	7
2.1.3 Density of states	8
2.1.4 Quantum Dots	9
2.2 Irradiation defects in III-V semiconductors	11
2.2.1 Irradiation defects in quantum-size structures	14
2.2.2 Electron and proton irradiation	16
2.3 Résumé	19
Bibliography	19
3 Sample growth and measurement techniques	23

3.1	Growth	23
3.1.1	Stranski-Krastanow growth mode	24
3.1.2	MOCVD	25
3.1.3	Samples growth	28
3.2	Measurement techniques	31
3.2.1	Photoluminescence	32
3.2.2	Photoluminescence excitation spectroscopy	36
3.2.3	Time-resolved photoluminescence	39
3.3	Résumé	41
	Bibliography	41
4	Characterization of the as-grown samples	45
4.1	Laser structures	45
4.2	Samples with non-uniform WL thickness	49
4.3	TU5411: dots-in-a-well structure	57
4.4	Other dots-in-a-well structures with different cap layer thicknesses . . .	60
4.5	Samples subjected to CCl ₄ treatment	69
4.6	Conclusions	72
	Bibliography	72
5	Radiation hardness	77
5.1	Introduction	77
5.2	Radiation hardness of QDs and QWs	79
5.2.1	k/k_0 Representations	81
5.3	Non-uniform WL thickness samples	85
5.4	Mechanisms of radiation hardness	86
5.5	Conclusions	87
	Bibliography	88

6	Carrier recombination and intradot relaxation	91
6.1	Introduction	91
6.2	Carrier dynamics	92
6.3	Equipment and measurement conditions	93
6.4	Proton-irradiated samples	94
6.4.1	Samples	94
6.4.2	Results	94
6.4.3	Discussion	101
6.5	Electron-irradiated samples	101
6.5.1	Samples	101
6.5.2	Results	102
6.5.3	Discussion	105
6.6	Conclusions	106
	Bibliography	107
7	Influence of defects on the temperature dependence of the PL intensity	109
7.1	Introduction	109
7.2	Equipment and measurement conditions	110
7.3	Experimental results	110
7.3.1	Laser structures	110
7.3.2	Samples subjected to CCl ₄ treatment	111
7.4	Model	115
7.4.1	Heterostructure in equilibrium	115
7.4.2	Heterostructure under illumination	117
7.4.3	Recombination channels	118
7.4.4	Steady-state excitation conditions	120
7.5	Calculated results	121

7.6	Discussion	125
7.7	Conclusions	128
	Bibliography	128
8	Conclusions and Outlook	131
8.1	Summary	131
8.2	Outlook	133
A	Spatial distribution of the minority carriers	135
B	Radiative recombination rates	137

Chapter 1

Introduction

A new class of structures — quantum dots (QDs) — has evolved during the last two decades. These structures combine the advantages of bulk semiconductors with those of isolated atoms. The strong need to miniaturize devices for several applications made the research in this area very promising from a technological but also from a scientific point of view. QDs provide significant improvements in modern devices, such as LEDs, solar cells, infrared detectors, single electron transistors, memories, and QD lasers, especially 1300 nm QD lasers on GaAs substrate, QD vertical cavity surface emitting lasers (VCSELs) and high-power QD lasers. QDs as an active gain medium in semiconductor lasers represent one of the first applications of the nanotechnology within active devices having commercial use. The requirements for this application are: low defect density, high quantum efficiency, high QD density and good size homogeneity.

Semiconductor properties and semiconductor device properties are highly influenced by the presence of structural defects, particularly the ones induced by irradiation with high-energy particles and gamma-rays. The defects' properties, creation and transformation mechanisms should be strongly changed when passing from a bulk semiconductor to a structure having such a low dimensionality as QDs. The device tolerance to the presence of defects, especially radiation-induced ones, is of crucial importance in several applications, such as space-based telecommunications and atomic energy.

A device in an actual space environment is irradiated with a spectrum of proton and electron energies, so that even if shielding is employed, the particles traversing a particular point in the device will possess energies ranging from a few eV up to ~ 100 MeV. So, a systematic study of radiation-induced defects in QD structures and its influence on device characteristics is of major importance not only from a scientific but also from

a technological point of view.

In this thesis, a study of radiation-induced defects in quantum structures of semiconductors is presented. Strained III-V QDs in the (In,Ga)As system, fabricated using Stanski-Krastanow growth mode in connection with self-organization phenomena, will be focused here. Irradiations with electrons and protons were undertaken on various types of samples, and differences are pointed out. The different radiation hardness of quantum dots and quantum wells is pointed out. The influence of the capping layer thickness on the optical properties of the QDs heterostructures was also investigated. The role of the wetting layer thickness on the properties of the QDs was studied as well. A rather simple model for the carrier statistics out of equilibrium which reproduces quite well the luminescence results as a function of temperature in a dots-in-the-well structure was developed in order to explain the trends of the ground-state emission from the QDs.

The present chapter, chapter 1, presents the problem and justifies the topic chosen for this work. It includes a brief description of the structure of this thesis.

In chapter 2, the state of the art is presented, including properties of In(Ga)As/GaAs quantum dot heterostructures and irradiation defects in III-V semiconductors and related quantum-size structures.

In chapter 3, sample growth methods and experimental techniques are presented. The Metal-Organic Chemical Vapour Deposition (MOCVD) technique and the Stranski-Krastanow growth mode are briefly discussed. Several experimental methods were used to characterize the samples under study, namely photoluminescence (PL), photoluminescence excitation (PLE), time-resolved photoluminescence (TRPL) and resonantly excited photoluminescence (REPL).

The characterization of samples prior to irradiation is included and discussed in chapter 4. Samples with different structures were characterized and the results are presented.

Chapter 5 includes results of radiation hardness of quantum structures irradiated with electrons or protons. A higher resistance to radiation-induced defects was observed for the QD-based heterostructures.

Carrier recombination and intradot relaxation were studied in order to understand the role of defects in the mechanisms of carrier relaxation and recombination in the quantum dot heterostructures. Results and possible effects as a function of irradiation fluence are pointed out in chapter 6.

In chapter 7, the influence of defects on the temperature dependence of the PL emission is presented. The quasi-Fermi level position of the minority carriers is discussed and a photocarrier statistical model including both radiative and non-radiative recombination channels is applied to explain the trends of the ground-state emission from a dots-in-the-well structure.

At last, in chapter 8, a brief summary with main conclusions is driven. Suggestions for future work regarding defects and their influence on the properties of quantum structures of semiconductors are proposed.

Chapter 2

State of the art

2.1 Properties of InAs/GaAs heterostructures

2.1.1 GaAs and InAs

One of the most technologically advanced and widely used compound semiconductor is GaAs [Alferov, 1998]. It has a place of honour in semiconductor physics and electronics due to its properties, such as direct band structure, high carrier mobility, among others.

Table 2.1: Properties of GaAs and InAs [Madelung, 1982, 1987]. All values are given for room temperature.

Symbol	Description	Value	Unit
$E_{g,GaAs}$	GaAs bandgap	1.424	eV
a_{GaAs}	lattice constant	0.565	nm
$T_{d,GaAs}$	threshold energy of atomic displacement	$7 - 11^a$	eV
$m_{GaAs,e}^*$	effective mass of electrons in GaAs	0.067^b	m_0
$m_{GaAs,lh}^*$	effective mass of light holes in GaAs	0.08^b	m_0
$m_{GaAs,hh}^*$	effective mass of heavy holes in GaAs	0.47^b	m_0
$E_{g,InAs}$	InAs bandgap	0.354	eV
a_{InAs}	lattice constant	0.605	nm
$T_{d,InAs}$	threshold energy of atomic displacement	$6.7 - 8.3^a$	eV
$m_{InAs,e}^*$	effective mass of electrons in InAs	0.0239	m_0
$m_{InAs,lh}^*$	effective mass of light holes in InAs	0.026	m_0
$m_{InAs,hh}^*$	effective mass of heavy holes in InAs	0.35	m_0

^a[Bourgoin and Lannoo, 1983; Massarani and Bourgoin, 1986]

^b[Basu, 1997]

GaAs and InAs are binary compounds since they consist of two different elements – Ga or In from column III and As from column V of the Periodic table. Gallium has the electron configuration $4s^2 4p^1$, while arsenic has the structure $4s^2 4p^3$. Two silicon-like atoms can be produced from Ga and As by transferring one of the p-electrons from As to an empty p-level in Ga, so that each atom has the configuration $4s^2 4p^2$, similar to that of the group IV atoms [El-Kareh, 1995].

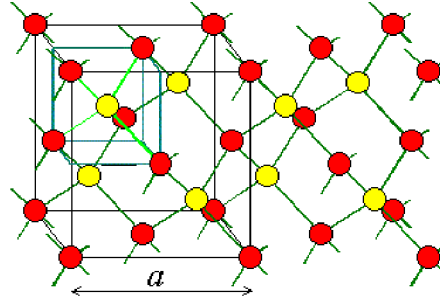


Figure 2.1: Zincblende structure of GaAs and InAs (the red balls belong to one FCC unit and the yellow ones to the other).

GaAs and InAs both crystallize in the zincblende structure which consists of two interpenetrating face-centred cubic (FCC) units (figure 2.1). One of the units is displaced with respect to the other by $a/4 \langle 111 \rangle$, where a is the lattice parameter of the layer. One unit is occupied by group III atoms, whereas group V atoms reside on the second unit. These two compounds are known to be completely miscible to form ternary InGaAs alloys [Stringfellow, 1974].

The advantages of growing strained InAs on GaAs substrates are the ability to utilize strain effects, bandgap discontinuities between InAs and GaAs and integrate InAs based devices with GaAs devices. The strain itself can be useful, since in-plane mobility can be enhanced in two-dimensional electron gases confined in a strained InAs layer embedded in GaAs. The band discontinuities allow confinement of electrons and holes to the InAs layer [Fitzgerald, 1993].

When a thin film of a semiconductor with the lattice constant a_L is deposited on a semi-infinite substrate with the lattice constant a_S , two regimes can be observed. If the thickness of the overlayer is small, the layer is under biaxial strain where the in-plane lattice constant is the same as that of the substrate and the out-of-plane lattice constant is given by the Poisson effect. If the overlayer thickness is too large, a dislocation network is created in the layer. The overlayer thickness separating these two regimes is called the critical thickness and varies inversely with the mismatch between

the substrate and the overlayer. The below-critical thickness regime is the regime of pseudomorphic epitaxy. The mismatch between InAs and GaAs lattice constants is of 6.7 %. The critical thickness for InAs growth on GaAs (001) is ≈ 0.45 nm. An important result has been obtained in 1985: generation of dislocations above the critical thickness can be avoided through the formation of nanoislands — quantum dots [Goldstein et al., 1985]. According to [Bimberg et al., 1999], quantum dots are coherent inclusions in a semiconductor matrix with truly zero-dimensional electronic properties.

The effect of strain is to break the usual cubic symmetry of the crystal lattice. As a result of the strain and symmetry loss there are two important consequences on the band structure: (i) the band edge positions and other high symmetry positions are altered; (ii) degeneracy is lifted. The first effect can be used to tailor the bandgap of the material, while the second can alter the density of states at band edges. The strain can not only modify the bandgap, but, more importantly, can remove the heavy hole–light hole degeneracy and thus alter the density of states of the valence band.

Generally speaking, strained-layer structures offer two broad classes of advantages over lattice-matched systems: first, new bandgaps are accessible through the greater freedom in choice of alloy compositions; and secondly, the strain splitting of the valence band at the Γ point allows valence band engineering with the potential for the highest valence band state to have light hole character in the plane of the well.

Since the recombination occurs in InAs, the emission wavelength will be longer than that of the GaAs band edge emission. Any such optical and electrical device can be integrated with GaAs devices on the same substrate.

2.1.2 Band offsets

The band offset is a consequence of the difference between the energy gaps of the semiconductors making up the structure. The energy gap difference is distributed between a conduction band offset ΔE_C and a valence band offset ΔE_V .

At a type-I interface (see figure 2.2a), both electrons and holes near the junction tend to migrate to the smaller-gap semiconductor. Potential barriers in this case exist for both electrons and holes in going from the smaller-gap semiconductor to the larger-gap one.

Nanometer-sized In(Ga)As QDs in a GaAs matrix represent localization centres for

both electrons and holes, since the bandgap of In(Ga)As is lower than that of the surrounding GaAs matrix and InGaAs/GaAs interfaces are type-I heterojunctions.

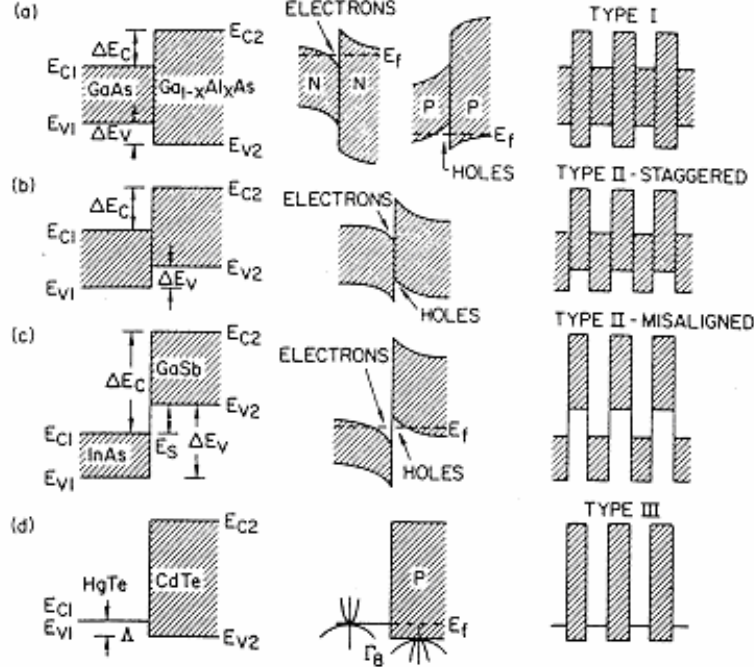


Figure 2.2: Discontinuities of band edge energies at four kinds of hetero-interfaces: band offsets (left), band bending and carrier confinement (middle), and superlattices (right). [Esaki, 1986]

In type-II QDs (see figure 2.2b), e.g. Ge/Si, one charge carrier is localized inside the dot and the other one in the barrier. Due to the Coulomb interaction, the carrier in the barrier becomes bound to the QD; the carrier inside the QD modifies its orbital to increase the probability close to the dot boundary.

Confined charge carriers, i.e. electrons and holes, interact via the Coulomb interaction. The correlation of the carrier motion by the Coulomb interaction not only changes the energy spectrum of the system but also alters the oscillator strength of the transitions, i.e. their lifetime, which is of particular importance for optoelectronic applications [Bimberg et al., 1999]. When the ground states for electrons and holes in a QD are populated by one carrier each, automatically an exciton is formed.

2.1.3 Density of states

Because of full quantization in all three dimensions, the eigenspectrum of a single dot consists of a discrete set of eigenenergies [Grundmann et al., 1995b] depending only on

the number of atoms making up a dot. Variations of strain or shape lead to additional continuous variation of the eigenenergies from dot to dot.

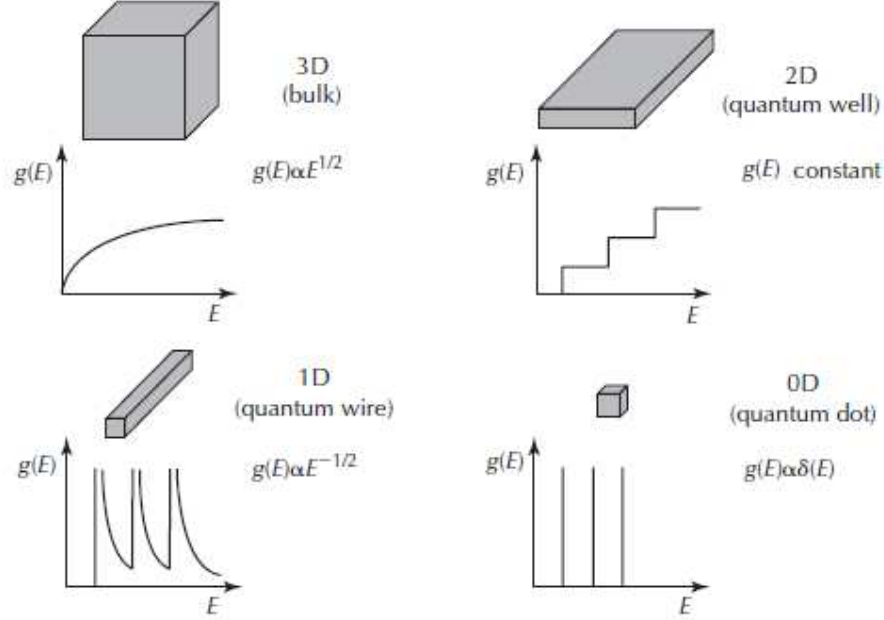


Figure 2.3: Density of states for charge carriers in structures with different dimensionality [Clarke and Murray, 2008].

Due to the QD δ -function-like density of states (see figure 2.3), ultra-narrow cathodoluminescence lines with a full width at half maximum (FWHM) of 0.15 meV or less could be observed for single InAs/GaAs QDs at low temperatures [Grundmann et al., 1995a]; the value of 0.15 meV was limited by the spectral resolution of the setup. A typical *ensemble* of self-organized QDs, however, exhibits a finite size distribution, leading to an inhomogeneous broadening of the transition line, the FWHM of which typically ranges from 25 to 80 meV. Electron and hole levels in QDs as well as transition probabilities between these levels can be calculated within an 8-band $k \cdot p$ framework [Stier, 2001].

2.1.4 Quantum Dots

On the contrary to quantum wells (QWs), where carriers are localized in one direction perpendicular to the layers but move freely in the layer plane, and to quantum wires (QWRs), where the carriers are localized in two directions and move freely along the wire axis, in QDs the carriers are confined in all three directions. So, the QDs can be considered as “artificial atoms” with a totally discrete energy spectrum. The physical

properties of QDs in many respects, although not all, resemble those of an atom in a cage [Bimberg et al., 1999].

Since the lateral extension of self-organized QDs is comparable to the exciton Bohr radius, the electronic levels of both electron and hole states are substantially determined by the size, shape and chemical composition of the QDs [Grundmann et al., 1996]. Therefore, QDs have more in common with the electronic structure of atoms than of solids (see figure 2.4).

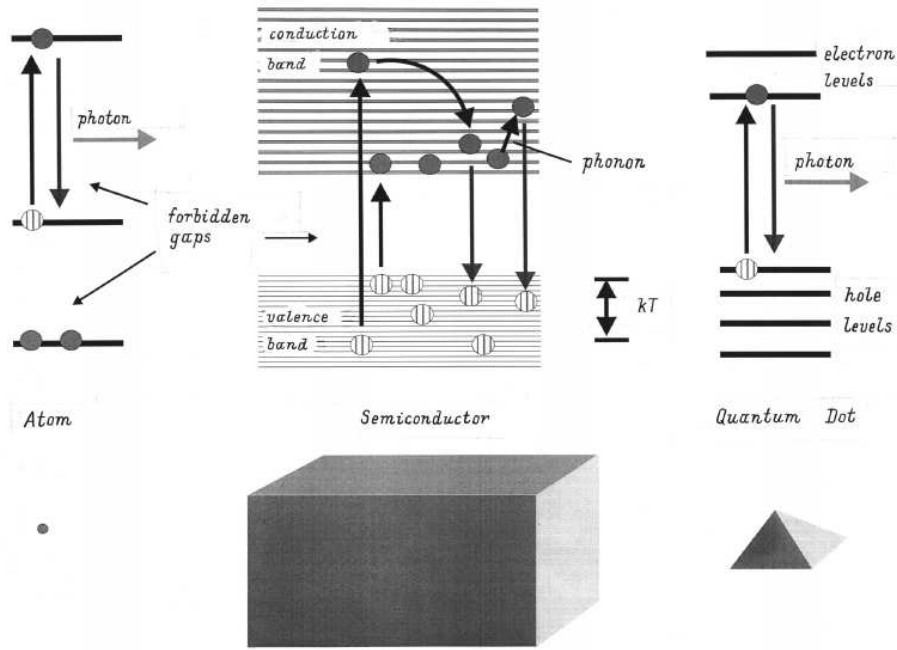


Figure 2.4: Schematic representation of energy levels in a single atom, a bulk semiconductor and a quantum dot [Bimberg et al., 1999].

A decisive difference between QDs and atoms is the lower spatial symmetry of QDs which are not spherically symmetric. Moreover, the strain in self-organized III-V QDs induces a piezoelectric field, owing to the strain-related relative displacements of the anion and cation sub-lattices. This further reduces the QD symmetry. None of the transition selection rules valid for atoms exist for QDs, so that transitions from any electron state to any hole state are essentially possible [Stier, 2001]. The transition matrix elements are in good approximation proportional to the spatial overlap integrals of the respective electron and hole wavefunctions.

In order to make QDs useful for devices at room temperature, they should fulfil the following requirements [Bimberg et al., 1999]: (i) sufficiently deep localizing potential and small QD size; (ii) high uniformity of the QD ensemble and a high volume filling

factor; (iii) the material should be coherent with the surrounding matrix without defects like dislocations.

There have been predictions that, even if ideal QDs could be fabricated, they could be hardly used for real devices, as ultra-long relaxation times between electron sublevels should be expected, “phonon bottleneck” [Benisty et al., 1991]. However, soon this idea was technically surpassed with the realization of a QD laser with low threshold current density based on self-organized QDs in 1994 [Kirstaedter et al., 1994]. More recent results [Heitz et al., 2002] show that the existence of a phonon bottleneck may depend on the QD shape.

Many different shapes have been reported for InAs QDs grown on GaAs using MBE [Bimberg et al., 1999], from disks [Legrand et al., 1998; Wu et al., 1997] to pyramids [Maximov et al., 2000] passing through truncated pyramids [Guffarth et al., 2001]. The growth of InAs QDs on GaAs starts with the formation of a planar layer, called the wetting layer (WL), before the elastic strain relaxation promotes the 3D islands appearance (see section 3.1 for a more detailed discussion on growth conditions and mechanisms). Transmission electron microscopy (TEM) images of MBE grown InAs/GaAs QDs show, for a wetting layer thickness of 1.2 nm, a pyramidal shape with a base length of 12 ± 1 nm and a density of $\sim 10^{11}$ dots/cm² [Grundmann et al., 1995a]. Cross-sectional scanning tunnelling microscopy (XSTM) techniques allow yielding detailed information on both structural properties and composition of QDs. TEM and XSTM from InAs QDs grown using MOCVD show a truncated pyramid shape [Eisele et al., 1999; Heinrichsdorff et al., 1997; Yoon et al., 1999]. However, the shape can change with InAs amount deposited [Jin et al., 2000], going from a round base shape to a triangular base shape passing through an ellipsoidal base, and growth interruption time [Pötschke et al., 2004], going from truncated pyramids to fully developed pyramids for growth interruption times ranging from 2 to 270 s.

2.2 Irradiation defects in III-V semiconductors

The content of this section is mainly based on the book [Claeys and Simoen, 2002].

Light-emitting diodes (LEDs), laser diodes (LDs) and photodetectors (PDs) are examples of semiconductor devices used in opto-electronic components with space applications. III-V semiconductors, namely GaAs and related compounds, are in most cases the materials chosen for such applications. The main characteristics leading to

this choice are the direct bandgap, yielding high quantum efficiency, and the superior radiation tolerance.

The result of irradiating a semiconductor material with energetic particles or γ -quanta will depend on radiation type, its mode (pulsed, continuous) and type of interaction with the material, as well as the material type. The two main radiation interaction types with materials are atomic displacements, giving rise to atoms which are displaced from their usual lattice sites, and ionization which creates free electron-hole pairs by disrupting electronic bonds. All particles (electrons, protons, heavy ions and photons ranging from UV to γ energies) except neutrons produce ionization effects in materials [Bourgoin and Lannoo, 1983].

According to the interaction types, the energy losses mainly occur through two nearly independent processes: (i) elastic collisions with the nuclei known as nuclear energy loss, and (ii) inelastic collisions of the highly charged projectile with the atomic electrons of the matter known as electronic energy loss.

In the inelastic collision, the energy is transferred from the projectile to the atoms through excitation and ionization of the surrounding electrons.

The atomic displacements occur due to the transfer of momentum of the incident particle to the atoms of the target material (nuclear energy loss). Provided an atom subjected to such a collision receives sufficient kinetic energy, called the displacement threshold energy, it will be removed from its position and leave behind a vacancy (V). The atom and the vacancy form a Frenkel pair. If the energy transferred is not enough to displace the atom far enough from its position, immediate recombination of the Frenkel pair may occur. The removed atom may meet another such vacancy and recombine or lodge in an interstitial position in the lattice (a self-interstitial, I) or be trapped by an impurity atom. The vacancies may be mobile, too, and either combine with impurity atoms and/or cluster with other vacancies. Defects that are stable at the irradiation temperature may become mobile upon subsequent heating. The probability for such atomic displacements is higher for higher incident particle energy and mass. However, for proton irradiation in Si, only 1 % of the energy loss goes into displacement processes for a wide range of particle energies [Dale and Marshall, 1991].

Regardless of whether an atom is displaced as part of a damage cascade or as an individual low energy primary knock-on atom, most of the initial vacancy-interstitial pairs recombine and no permanent disorder results. Only a small fraction of V-I pairs survives and migrates in the material, where they can undergo different types of in-

teractions with impurities in the lattice. In the end, more stable radiation damage is formed, which consists generally of small point defect complexes.

For opto-electronic components, beside the degradation of the electrical parameters, optical material properties are also of concern. The main effects of processing- or radiation-induced defects are reduction of the carrier density termed carrier removal and reduction of the mobility caused by displacement damage. The reduction of the carrier density is a net result of carrier trapping by radiation-induced trap levels and charge compensation by created defects with opposite character. The mobility degradation is caused by Coulomb scattering at charged centres, which include the created traps.

While in elemental semiconductors one only has to deal with vacancies and interstitials, the situation is more complex in III-V semiconductors. In GaAs, the simple point defects that can be observed are the As vacancy and interstitial, usually denoted by V_{As} and As_i , and the Ga vacancy and interstitial (V_{Ga} and Ga_i). In addition, the antisite defects, i.e. an As atom on a Ga site and vice versa, these are abbreviated as As_{Ga} and Ga_{As} , should be considered. Antisite defects are characterized by 4 nearest neighbours of the same element and are also noted as $AsAs_4$, for example. The defects produced in *n*- and *p*-type GaAs by electron irradiation consist in a distribution of vacancy-interstitial pairs in the As sub-lattice. The vacancy-interstitial pairs in the Ga sub-lattice recombine immediately after their creation at RT [Pons and Bourgoin, 1985].

For the evaluation of the radiation damage in solids the mobility of the defects is of paramount importance. In semiconductors such as Si, Ge, GaAs, GaSb, InP, InAs, AlAs, and InSb a large part of the primary defects undergoes annihilation even below room temperature. The radiation defects in these materials, which are found at room temperature, consist mainly of secondary and tertiary complexes formed by migration and agglomeration of vacancies and interstitials with each other and with impurities [Sobolev, 2008]. According to [Claeys and Simoen, 2002], a close connection between the grown-in point defects and the radiation-induced ones exists, allowing inferring that there will be a strong impact of the starting material growth techniques on the built-in devices radiation hardness.

2.2.1 Irradiation defects in quantum-size structures

In order to predict the radiation damage in quantum-size structures, first of all knowledge of the creation, transformation, and annihilation processes of radiation defects in corresponding bulk materials including alloys is needed (see section 2.2).

Since the primary defects are mobile at RT in GaAs and certainly in InAs, it is very likely that they are captured at the interfaces (cf. [Sobolev et al., 1996]). Moreover, the defects raise the crystal's free energy, so that it is only natural that the QDs expulse mobile defect components into the matrix. An effect called “self-purification” [Dalpian and Chelikowsky, 2006] has been identified as being an intrinsic property of defects in semiconductor nanocrystals, since the defects formation energies increase as the size of the nanocrystals decreases (see figure 2.5). A very recent publication [Bai et al., 2010] shows the role of grain boundaries in copper as effective sinks for radiation-induced defects.

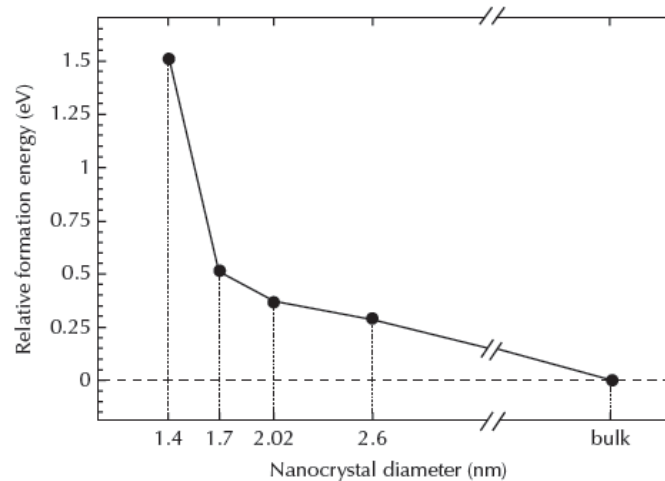


Figure 2.5: Variation of the formation energy of a substitutional Mn impurity in a CdSe nanocrystal as a function of the nanocrystal diameter [Dalpian and Chelikowsky, 2006].

To solve the problem of the radiation hardness of a device, one has to establish which layer (or layers) in a concrete, probably very complicated, structure predominantly determines the device parameters degradation. In devices like light-emitting diodes (LEDs) or lasers containing low-dimensional active layers it is important to know which is the volume sampled by the wavefunction of the electrons and holes participating in the radiative recombination. Finally, the role of the Fermi level position, hetero-interfaces and strain in the defect evolution and defect reactions, the mutual influence of the adjacent layers, and the impact of the quantum confinement on the structure and

properties of local defects, which are supposed to be already known from the studies of the corresponding bulk semiconductors, have to be elucidated [Sobolev, 2008].

Modern LEDs are often based on quantum well structures in the InGaAs/GaAs/AlGaAs system, active around 875 nm. The operation of a LED is characterized by the light output versus the applied forward bias. The light output is proportional to the radiative recombination current and degrades if the non-radiative recombination current increases. The latter occurs when deep-level generation-recombination centres are induced by displacement damage [Claeys and Simoen, 2002].

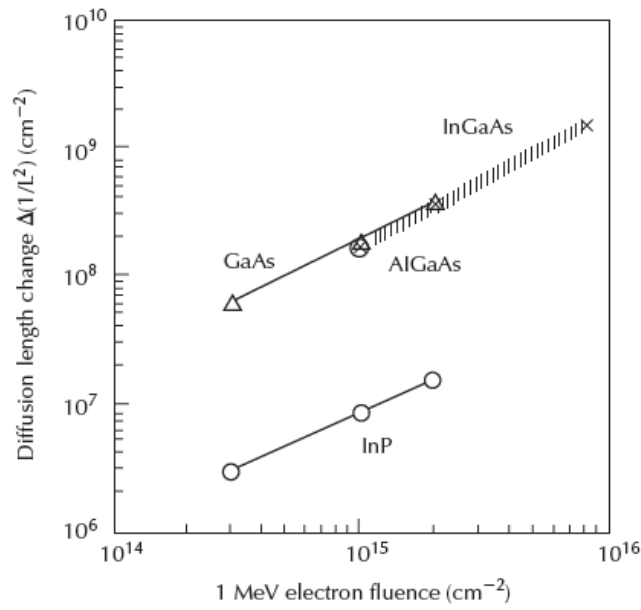


Figure 2.6: Changes in minority-carrier diffusion length L , determined by the EBIC method, for $\text{Al}_{0.35}\text{Ga}_{0.65}\text{As}$, $\text{In}_{0.15}\text{Ga}_{0.85}\text{As}$ and GaAs due to 1 MeV electron irradiations as a function of electron fluence in comparison with those of InP [Yamaguchi, 1995].

$\text{In}_{0.47}\text{Ga}_{0.53}\text{As}$ is one of the III-V compounds used for PDs due to the bandgap position, ~ 0.75 eV, making possible the absorption of wavelengths in the range 900 to 1600 nm, and the possibility of lattice matched deposition on InP SI substrates. Although a PD is a device with a surface active layer (junction), the light is absorbed much deeper in the material. Electron-hole pairs are thus generated at depths much larger than the depletion region, so that the carriers have to diffuse to the active region to be collected. The collection efficiency strongly depends on the minority carrier diffusion length, which depends on the damage produced by particle irradiation, as shown in figure 2.6 for electron irradiation [Yamaguchi, 1995].

From what was stated, it clearly follows that the recombination lifetime of the active

material plays a dominant role in the operation of opto-electronic components.

The following useful information can be learned from irradiation studies [Sobolev, 2008]:

(i) influence of the defects on the electronic properties of quantum-size structures and the corresponding device parameters; (ii) elucidation of the electronic structure of quantum-size structures as well as their carrier transport, relaxation and recombination processes using defects as microprobes; (iii) diffusion processes in quantum-size structures; (iv) novel technological processes of micro-, nano- and optoelectronics.

2.2.2 Electron and proton irradiation

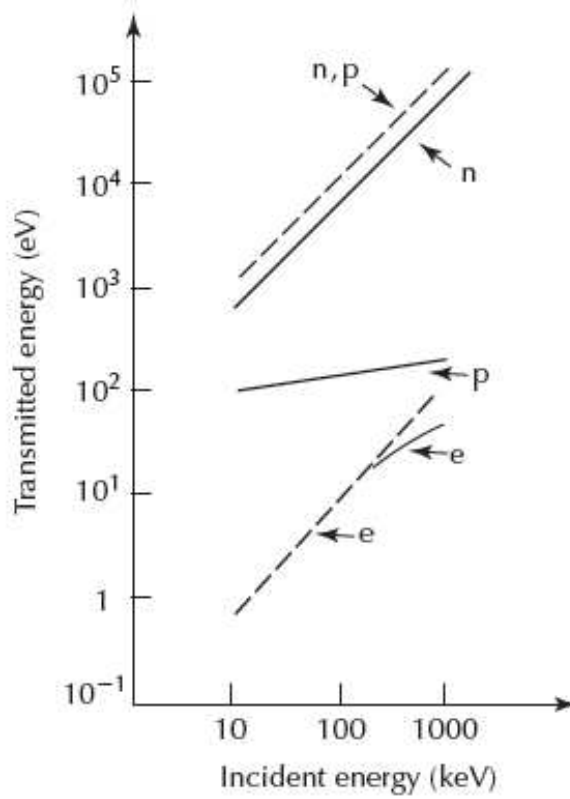


Figure 2.7: Maximum (dashed line) and average (full line) energy transmitted to a silicon atom as a function of the incident energy for electrons (e), protons (p) and neutrons (n) [Bourgoin and Lannoo, 1983].

Electron irradiation is an easy way to introduce simple intrinsic defects, i.e. vacancies and interstitials, in semiconductor structures in controlled quantities [Bourgoin and Lannoo, 1983]. This is due to the fact that the impinging electrons carry just enough kinetic energy to displace one single atom in one collision event with the atoms of the

solid. Moreover, the electron energy losses are such that the displacements are created homogeneously at a rather large depth (≈ 0.1 mm at 1 MeV) [Pons and Bourgoïn, 1985].

The peculiarities of the passage of electrons through matter are directly due to them being light particles. First of all, the character of their ionization stopping and multiple scattering differs from what is known about protons. An example of these differences can be observed in figure 2.7 for the energy transmitted to a silicon atom. The maximum energy transmitted can be as much as three orders of magnitude higher for protons than for electrons. Owing to the small electron mass, large-angle scattering turns out to be so essential when electrons pass through matter that, unlike the case of heavy charged particles, an electron loses any memory of its initial direction of motion upon having undergone a certain number of collisions. The second peculiarity, also related to its low mass, consists in another stopping mechanism added to it, namely, radiative stopping (bremsstrahlung) [Balashov, 1997].

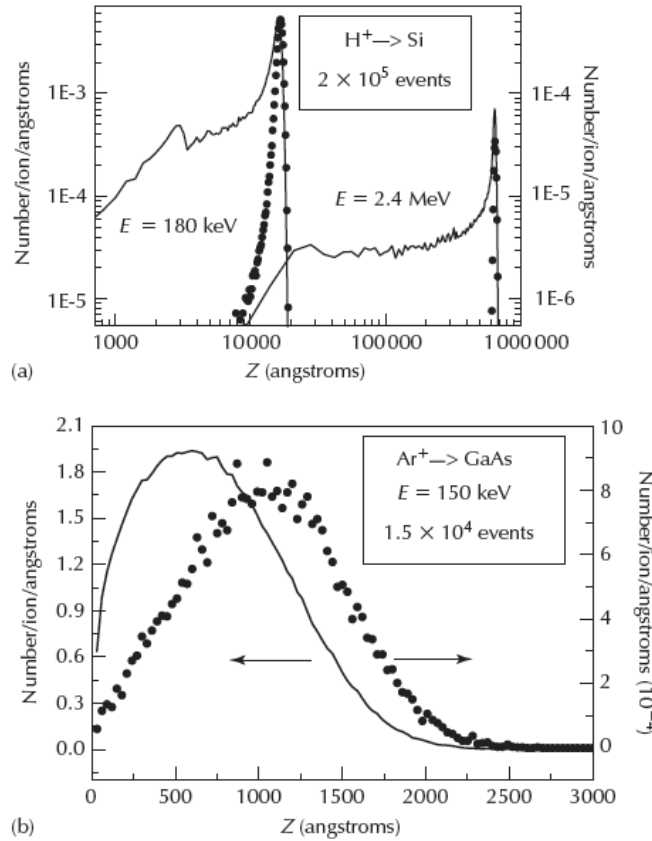


Figure 2.8: TRIM simulations of the depth distribution of the displaced target atoms (solid lines, left scale) and implanted atoms (dots, right scale) for the implantation of 180 keV and 2.4 MeV H^+ in Si (a) and 150 keV Ar^+ in GaAs (b). [Sobolev, 2008]

The displacement damage associated with electrons is more uniform along their trajectory than in the case of proton irradiation. As a consequence, no clear damage peak is formed [Claeys and Simoen, 2002].

On the contrary, the proton-induced damage profile (see figure 2.8a)) is highly non-uniform with a sharp maximum near the projected range R_p (penetration depth) so that the damage density at depths well below R_p can decrease with increasing proton energy, despite the increase of the total energy deposited in elastic collisions. However, it can be deduced that in the tail region the damage is quite uniform, while a peak is obtained around R_p where the particle comes to rest in the material. Most of the energy loss will take place in the final part, in a narrow interval around the projected range. This fact must be taken into account when irradiating nanometre thick layers containing QDs and situated near the sample surface. The resulting damage along an individual particle path becomes quite complex and may be composed of the initial cascade and branching terminal sub-clusters. This is also often termed cluster damage. A damage cluster in this context can be considered as an aggregate of several different lattice defects such as vacancies, dopant atoms, interstitials and site impurities [Claeys and Simoen, 2002].

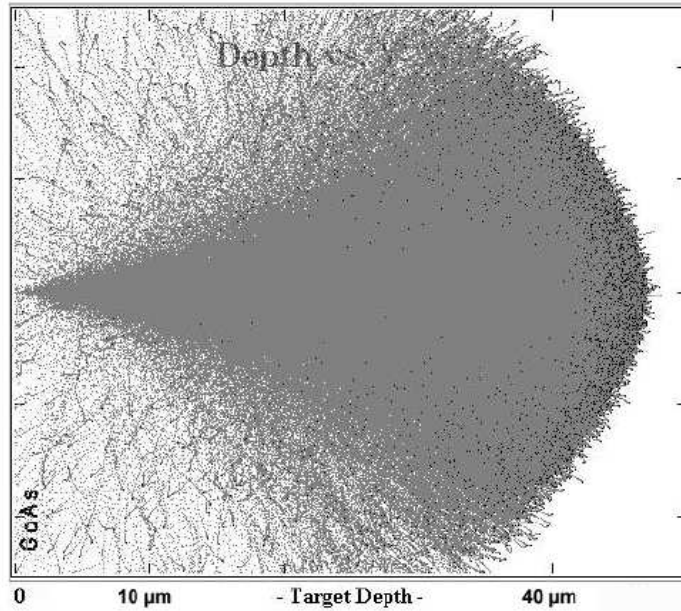


Figure 2.9: Simulation of the penetration of hydrogen atoms (2.4 MeV) in GaAs using the program SRIM2000. [Ziegler et al., 1985]

Figure 2.8 shows three examples of the primary damage and implanted ion concentration profiles calculated by TRIM for Si and GaAs. Figure 2.9 shows a simulation of

the penetration of a million hydrogen atoms with an energy of 2.4 MeV in GaAs. The mean penetration depth is $\approx 43 \mu\text{m}$.

2.3 Résumé

The current chapter presented a brief overview of the state of the art regarding properties of In(Ga)As/GaAs quantum dot heterostructures as well as radiation-induced defects in III-V semiconductors and related quantum-size structures. First, the main properties of GaAs and InAs were presented regarding structure and technological relevance. Then, the different type of heterostructures interfaces and band offsets were briefly reviewed. The changes in the density of states with increasing quantum confinement was discussed. Quantum dots were then introduced together with some issues relevant to this work. The second part of this chapter was related to radiation-induced defects. General notions were presented followed by a discussion of issues arising from irradiating quantum-size structures. Finally, particular aspects of irradiation of semiconductors irradiation with electrons and protons were discussed.

Bibliography

- Alferov, Z. (1998). *Semiconductors*, 32(1):1.
- Bai, X.-M., Voter, A., Hoagland, R., M., N., and Uberuaga, B. (2010). *Science*, 327:1631.
- Balashov, V. (1997). *Interaction of Particles and Radiation with Matter*. Springer, Germany.
- Basu, P. (1997). *Theory of Optical Processes in Semiconductors*. Clarendon, Oxford.
- Benisty, H., Sotomayor-Torres, C., and Weisbuch, C. (1991). *Physical Review B*, 44(19):10945.
- Bimberg, D., Grundmann, M., and Ledentsov, N. (1999). *Quantum Dot Heterostructures*. John Wiley & Sons, Chichester.
- Bourgoin, J. and Lannoo, M. (1983). *Point Defects in Semiconductors. II, Experimental Aspects.*, volume 35 of *Springer Series in Solid State Science*. Springer, Berlin.

- Claeys, C. and Simoen, E. (2002). *Radiation Effects in Advanced Semiconductor Materials and Devices*. Springer, Berlin et al.
- Clarke, E. and Murray, R. (2008). *Handbook of Self Assembled Semiconductor Nanostructures for Novel Devices in Photonics and Electronics*, chapter 3 – Optical Properties of In(Ga)As/GaAs Quantum Dots for Optoelectronic Devices, page 84. Elsevier, The Netherlands.
- Dale, C. and Marshall, P. (1991). In *Proceedings SPIE Charged-Coupled Devices and Solid State Optical Sensors II*, volume 1447, page 70.
- Dalpian, G. and Chelikowsky, J. (2006). *Physical Review Letters*, 96:226802.
- Eisele, H., Flebbe, O., Kalka, T., Preinerberger, C., Heinrichsdorff, F., Krost, A., Bimberg, D., and Dähne-Prietsch, M. (1999). *Applied Physics Letters*, 75:106.
- El-Kareh, B. (1995). *Fundamentals of Semiconductor Processing Technologies*. Kluwer Academic Publishers, Massachusetts.
- Esaki, L. (1986). *IEEE Journal of Quantum Electronics*, 22:1611.
- Fitzgerald, E. (1993). *Properties of lattice-matched and strained Indium Gallium Arsenide*, page 6. inspec.
- Goldstein, L., Glas, F., Marzin, J., Charasse, M., and Le Roux, G. (1985). *Applied Physics Letters*, 47:1099.
- Grundmann, M., Christen, J., Ledentsov, N., Bohrer, J., Bimberg, D., Ruvimov, S., Werner, P., Richter, U., Gosele, U., Heydenreich, J., Ustinov, V., Egorov, A., Zhukov, A., Kop'ev, P., and Alferov, Z. (1995a). *Physical Review Letters*, 74:4043.
- Grundmann, M., Ledentsov, N., Stier, O., Bohrer, J., Bimberg, D., Ustinov, V., Kop'ev, P., and Alferov, Z. (1996). *Physical Review B*, 53(16):R10509.
- Grundmann, M., Stier, O., and Bimberg, D. (1995b). *Physical Review B*, 52:11969.
- Guffarth, F., Heitz, R., Schliwa, A., Stier, O., Ledentsov, N., Kovsh, A., Ustinov, V., and Bimberg, D. (2001). *Physical Review B*, 64(8):085305.
- Heinrichsdorff, F., Krost, A., Kirstaedter, N., Mao, M.-H., Grundmann, M., Bimberg, D., Kosogov, A., and Werner, P. (1997). *Japanese Journal of Applied Physics*, 36:4129 – 4133.

- Heitz, R., Born, H., Guffarth, F., Stier, O., Schliwa, A., Hoffmann, A., and Bimberg, D. (2002). *Physica Status Solidi A*, 190:499–504.
- Jin, Z., Yang, S., Liu, B., Li, M., Wang, X., Li, Z., Du, G., and Liu, S. (2000). *Optical Materials*, 14:211.
- Kirstaedter, N., Ledentsov, N., Grundmann, M., Bimberg, D., Ustinov, V., Ruvimov, S., Maximov, M., Kop'ev, P., Alferov, Z., Richter, U., Werner, P., Gösele, U., and Heydenreich, J. (1994). *Electronic Letters*, 30:1416.
- Legrand, B., Grandidier, B., Nys, J., Stievenard, D., Gerard, J., and Thierry-Mieg, V. (1998). *Applied Physics Letters*, 73:96.
- Madelung, O., editor (1982). *Landolt-Börnstein Numerical Data and Functional Relationships in Science and Technology*, volume III, chapter Semiconductors: Physics of Group IV Elements and III-V Compounds. Springer-Verlag, Berlin.
- Madelung, O., editor (1987). *Landolt-Börnstein Numerical Data and Functional Relationships in Science and Technology*, volume III, chapter Semiconductors: Intrinsic Properties of Group IV Elements and II-V, II-VI and I-VII Compounds, pages 82 – 94. Springer-Verlag, Berlin.
- Massarani, B. and Bourgoin, J. (1986). *Physical Review B*, 34:2470.
- Maximov, M., Tsatsulnikov, A., Volovik, B., Sizov, D., Shernyakov, Y., Kaiander, I., Zhukov, A., Kovsh, A., Mikhlin, S., Ustinov, V., Alferov, Z., Heitz, R., Shchukin, V., Ledentsov, N., Bimberg, D., Musikhin, Y., and Neumann, W. (2000). *Physical Review B*, 62:16671.
- Pons, D. and Bourgoin, J. (1985). *Journal of Physics C: Solid State Physics*, 18:3839.
- Pötschke, K., Müller-Kirsch, L., Heitz, R., Sellin, R., Pohl, U., Bimberg, D., Zakharov, N., and Werner, P. (2004). *Physica E*, 21:606.
- Sobolev, N. (2008). *Handbook of Self Assembled Semiconductor Nanostructures for Novel Devices in Photonics and Electronics*, chapter 13 – Radiation Effects in Quantum Dot Structures, page 392. Elsevier, The Netherlands.
- Sobolev, N., Korshunov, F., Sauer, R., Thonke, K., König, U., and Presting, H. (1996). *Journal of Crystal Growth*, 167:502.

BIBLIOGRAPHY

- Stier, O. (2001). *Electronic and Optical Properties of Quantum Dots and Wires in Berlin Studies in Solid State Physics*, volume 7. Wissenschaft & Technik Verlag, Berlin.
- Stringfellow, G. (1974). *Journal of Crystal Growth*, 27:21.
- Wu, W., Tucker, J., Solomon, G., and Harris, J. (1997). *Applied Physics Letters*, 71:1083.
- Yamaguchi, M. (1995). *Journal of Applied Physics*, 78:1476.
- Yoon, S., Moon, Y., Lee, T.-W., Hwang, H., Yoon, E., and Kim, Y. (1999). *Thin Solid Films*, 357:81.
- Ziegler, J., Biersack, J., and Littmark, U. (1985). *The Stopping and Range of Ions in Solids*. Pergamon Press, New York.

Chapter 3

Sample growth and measurement techniques

3.1 Growth

The growth of high-quality films in terms of purity, morphology and freedom from crystalline defects requires careful preparation of the growth face of the substrates, from polishing to in-situ cleaning stage. The surface must be free from any damage, contamination, and inhomogeneities as they tend to produce surface defects.

As a strained layer is deposited, the strain energy increases, and, at some thickness termed the critical thickness, it will be energetically advantageous to introduce misfit dislocations. The mismatch between InAs and GaAs is around 6.7 % and high misfit systems do contain many edge misfit dislocations. With such a misfit, the InAs growth is typically three-dimensional and the critical thickness is small, as thin as 1.7 ML [Gerard, 1992; Reithmaier et al., 1991; Toyoshima et al., 1993; Wang et al., 1991]. If the InAs thickness is below the critical thickness, no dislocations can be formed. So, good-quality layers are possible in InAs/GaAs heterostructures when the lattice mismatch between GaAs and InAs is totally accommodated by the elastic strain [Dutta and Pamulapati, 1993].

QDs for the application in optoelectronic devices are fabricated using a self-organization concept: a thin semiconductor film is epitaxially deposited on a substrate having a different lattice constant. Driven by the strain arising from the lattice mismatch, three-dimensional QDs are formed by material redistribution and agglomeration at

spontaneously defined nucleation sites on the surface [Bimberg et al., 1999; Ledentsov et al., 2002].

Generally, the goal is to fabricate QD arrays with a high QD density, a small size spread, and a low density of defects such as dislocations, coalesced QDs or dislocated clusters.

3.1.1 Stranski-Krastanow growth mode

If a layer of a material having a different lattice constant from the substrate is deposited, the growth of a strained material varies according to the relation between substrate surface energy (γ_1), epitaxial layer surface energy (γ_2) and interface energy (γ_{12}). If

- $\gamma_2 + \gamma_{12} > \gamma_1 \implies$ Volmer-Weber growth (figure 3.1a)
- $\gamma_2 + \gamma_{12} < \gamma_1$
 - lattice match \implies Frank van der Merve growth mode (figure 3.1b)
 - lattice mismatch \implies Stranski-Krastanow growth (figure 3.1c)

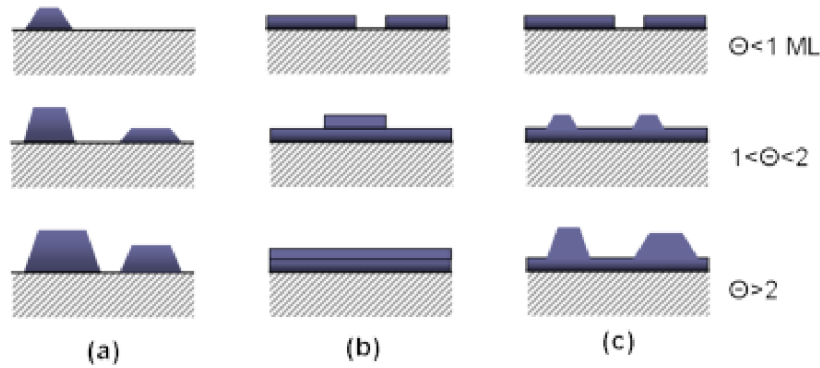


Figure 3.1: Different growth modes of crystal epilayers on lattice-mismatched substrates. a) Volmer-Weber mode b) Frank-van der Merve mode c) Stranski-Krastanow mode. For the Stranski-Krastanow growth, surface wetting and a large lattice mismatch are necessary.[Wikipedia, 2010]

The driving force for the formation of three-dimensional islands is related to elastic strain relaxation. A thicker layer has a higher elastic energy, and the elastic energy tends to be reduced via formation of isolated islands. In these islands the elastic strain relaxes and, correspondingly, the elastic energy increases — Stranski-Krastanow growth

mode. The transition from 2D to 3D growth depends on the main growth parameters: substrate temperature, arsenic pressure and film thickness [Goldstein et al., 1985].

The Stranski-Krastanow (SK) growth mode of InAs on GaAs has been shown to form three-dimensional InAs QDs spontaneously on top of an initial planar InAs WL, driven by the accumulated strain energy from a large 6.7 % lattice mismatch between InAs and GaAs. For self-organized QDs, larger quantization effects, higher localization energies and sublevel separations are observed than for any other classes of dots [Bimberg et al., 1999].

The discovery of this so-called Stranski-Krastanow (SK) growth mode was a major breakthrough in the development of QD lasers since only self-organized QDs have the crystalline quality required for the realization of the theoretical advantages of QD lasers [Bimberg, 2001].

3.1.2 MOCVD

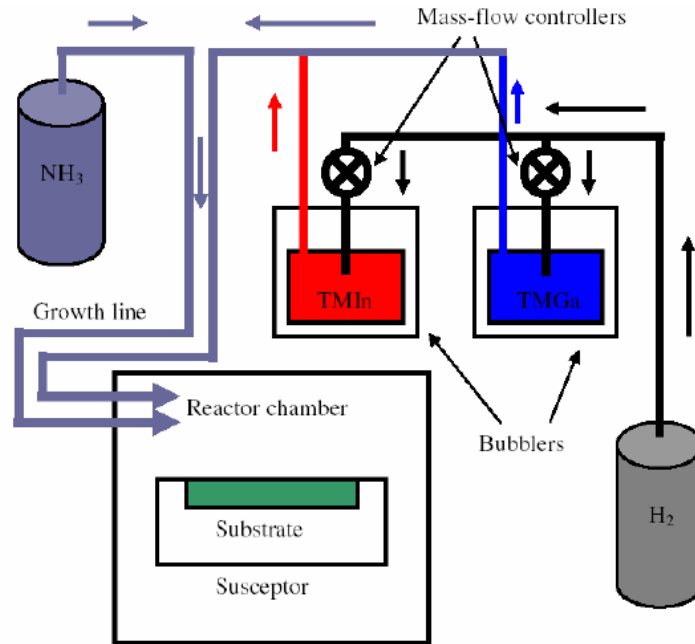


Figure 3.2: Schematic diagram of a MOCVD growth reactor used for III-V semiconductors growth [Pereira, 2005].

MOCVD (Metal-Organic Chemical Vapour Deposition) is an important commercial large-scale fabrication technology for electronic and optoelectronic semiconductor devices.

3.1. GROWTH

The elements required for MOCVD growth are produced by the thermal decomposition of source gases on a heated substrate (figure 3.2). This process requires organometallic source materials (precursors) of high purity, whose decomposition leads to the production of the desired material, such as InAs or InGaAs.

Table 3.1: Major differences between MBE and MOCVD growth techniques [Sellin, 2003].

MBE	MOCVD
extensive baking-out of substrates previous to growth	very high deposition rates
UHV	No UHV
growth conditions can very accurately be defined, controlled, and monitored	growth is more difficult to control
reactants can be supplied in elemental form by molecular beams	reactants are supplied as organic or hydride precursors that are thermally cracked by the heated substrate susceptor into growth-reactive species, making the fraction of reactants in the gas phase a function of temperature
growth process is controlled by substrate temperature and molecular flows only	aside from the choice of precursor molecules, total pressure and total gas flow are additional parameters that have to be controlled
RHEED – most important in-situ characterization tools allows to monitor surface reconstructions, surface smoothness on an atomic scale, surface diffusion lengths and deposition rates	in-situ monitoring like RHEED is not available (is not a UHV technique)

Depending on the growth techniques, mainly MBE and MOCVD, the islands differ in size, shape, chemical composition and lattice strain. Table 3.1 presents the major differences between MBE and MOCVD growth techniques according to [Sellin, 2003].

Thermodynamic and kinetic ordering mechanisms together can create unique three dimensionally patterns of islands within a matrix for many material systems. Formation of QD is, in many cases, an equilibrium process.

Temperature influence

The temperature window for the fabrication of high-quality QDs is narrow. The dot density and their relative geometrical arrangement were found to be strongly dependent on the substrate temperature [Heinrichsdorff et al., 1996]. Particularly in MOCVD of QDs for optoelectronic applications, a compromise between growth temperature, QD crystalline quality and QD size must be found. This window ranges from 500 to 600 °C. Growth temperatures lower than 500 °C would lead to a drastic decrease of the crystal quality. This effect is particularly pronounced in MOCVD where the organic parts of the metal-organic precursors can lead to significant carbon doping. The QD deposition temperature of about 500 °C is already very low as compared to temperatures of more than 600 °C used for GaAs layers to obtain optimum crystalline quality. Low crystal quality leads to a reduced radiative efficiency of the QDs. At temperatures significantly higher than 500 °C, self-organization of QDs in the SK growth mode is not possible due to thermodynamic arguments. In addition, even a slight temperature increase may lead to a drastic enhancement of the probability of cluster formation [Sellin, 2003]. According to [Heinrichsdorff et al., 1998a], a low growth temperature provides the conditions for the acquirement of high carrier localization energies in the QDs, and a high growth temperature allows achieving high material quality of the cap layers leading to the need of establishing a compromise for the choice of the growth temperature in order to fabricate QD based devices.

Amount of deposited material

The amount of deposited material has a strong influence on the QD density. For In-GaAs/GaAs it has been shown [Leon et al., 1999] that after the critical layer thickness is reached, the QD density quickly increases and then reaches a saturation density for a layer thickness of 1.1 times the critical thickness. The density is not significantly increased if the deposition continues. Similar results were obtained by Sellin [Sellin, 2003] with $\text{In}_{0.8}\text{Ga}_{0.2}\text{As}$, where the QD density changed from $2.2 \times 10^{10} \text{ cm}^{-2}$ to $3.3 \times 10^{10} \text{ cm}^{-2}$ with an increase in deposition amount of only 6%.

Growth interruption

During growth interruption, the QDs grow in size at the expense of the WL thickness [Heinrichsdorff et al., 1997], which translates into an increase of the ground state tran-

sition wavelength. The duration of the interruption has no effect on the dot density for InGaAs, suggesting that kinetic effects dominate the adjustment of the island density during or shortly after the deposition of the QD material [Heinrichsdorff et al., 1997; Sellin, 2003]. During the growth interruption the arsine flux has to be switched off in order to avoid the formation of incoherent clusters [Heinrichsdorff et al., 1998b].

Growth rate

The QD density and the PL efficiency of the QD layers also depend on the growth rate. So if the growth of QD layers for applications in laser diodes is the goal, both these dependences must be considered. Laser diode structures are optimized to maximum radiative efficiency. Higher densities are found with larger deposition rates both for MOCVD [Sellin, 2003] and MBE [Joyce et al., 2001] grown QD samples.

3.1.3 Samples growth

The samples studied during this work were obtained from different sources to which there were cooperation programs going on, namely Technical University of Berlin, Germany, and University of Nizhni Novgorod, Russia. The samples used were grown by Metal-Organic Chemical Vapour Deposition (MOCVD) through the Stranski-Krastanow growth mode.

Technical University of Berlin

At the Technical University of Berlin, arsine (AsH_3) was used as arsenic precursor. Trimethylgallium (TMGa, $(\text{CH}_3)_3\text{Ga}$), trimethylaluminium (TMAI, $(\text{CH}_3)_3\text{Al}$) and trimethylindium (TMIn, $(\text{CH}_3)_3\text{In}$) were used as group-III precursors. An Aixtron Aix200 MOCVD machine with a horizontal quartz-glass reactor at 20 mbar total pressure with graphite susceptor was used (figure 3.3).

For the deposition of ternary InGaAs QDs around 500 °C, TMGa was used. It has been reported that the use of TMGa at such growth temperatures leads to strong carbon incorporation and thus to significant intrinsic *p*-doping which would strongly decrease the radiative efficiency of InGaAs QD layers. This problem is reported not to occur if triethylgallium (TEGa, $(\text{C}_2\text{H}_5)_3\text{Ga}$) is used instead of TMGa [Stringfellow, 1999]. However, a more recent work [Sellin, 2003] presenting a comparative study of InGaAs

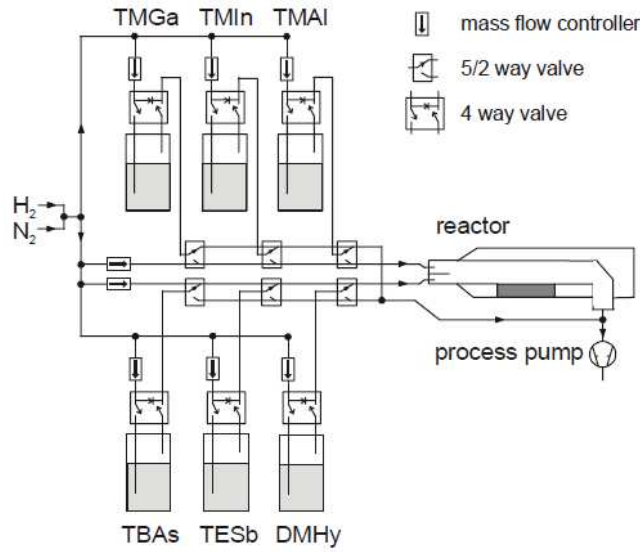


Figure 3.3: Simplified schematic of the MOCVD setup of the Aix machine used at the Institute of Solid State Physics of the Technical University of Berlin, Germany [Sellin, 2003].

QD grown with TMGa and TEGa shows no difference in radiative efficiency of both structures.

After deposition of the GaAs buffer layer at 640 °C, the growth was stopped, and the temperature was lowered to 425–525 °C for the QD layer growth. The growth rate for the dot layer was varied between 0.5–0.03 monolayers per second (ML/s). After the QD deposition, a growth interruption between 4 and 14 s was applied with both the group-III and group-V precursors switched off. Subsequently, the QDs were overgrown with a GaAs cap layer at the same temperature. After QD formation, the temperature can not be increased to prevent intermixing with the GaAs cap layer. For some samples, additional AlGaAs layers were introduced below and above the QD layer to act as blocking layers against carrier diffusion to the surface and into the substrate, thus increasing the luminescence efficiency at elevated temperatures.

University of Nizhni Novgorod

At Nizhni Novgorod, the precursors used were Trimethylgallium (TMGa, $(\text{CH}_3)_3\text{Ga}$), trimethylindium (TMIIn, $(\text{CH}_3)_3\text{In}$) for the group-III materials and Arsine (AsH_3) with H_2 being the gas carrier in a fused silica tube reactor. The InAs QDs were grown in an alternating monolayer epitaxy mode. TMIIn and AsH_3 were introduced in the

reactor separately switching the flows alternatively with a few seconds of pause between them. The flow rates of the precursors were adjusted so that 1 monolayer (ML) of InAs was deposited in a cycle. The pauses were to enrich the growing surface with In to stimulate the QDs formation. The InGaAs QWs and GaAs cladding layers were grown in a conventional MOVPE mode at the same temperature as the QDs [Karpovich et al., 2004].

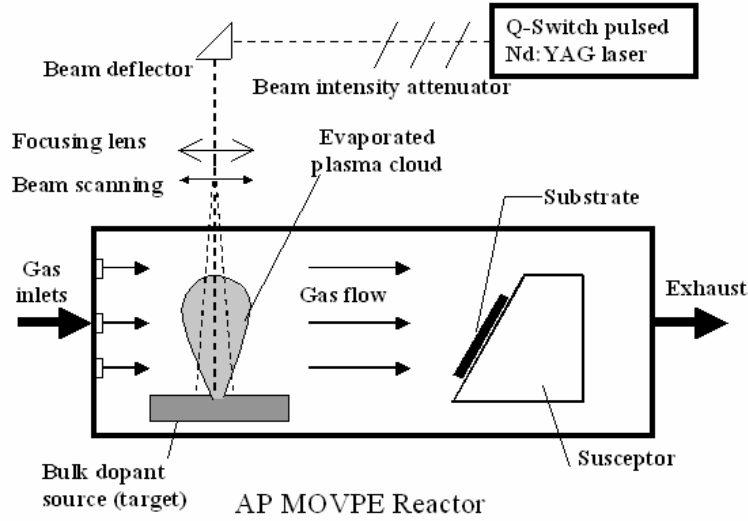


Figure 3.4: Scheme of doping from a bulk elementary source by pulsed laser sputtering in AP-MOVPE process used at the University of Nizhny Novgorod, Russia [Karpovich et al., 2004].

The QD structures were grown using Bi as a surfactant that has increased the QD uniformity and dumped the coalescence of the InAs nanoclusters [Zvonkov et al., 2000]. Bismuth was deposited onto the InAs growing surface by pulsed laser sputtering of a bulk Bi target placed in a cold zone of the reactor (figure 3.4). The resulting cloud of single Bi atoms was carried to the substrate by the gas flow [Karpovich et al., 2004]. The mechanism for the effect of Bi on the QDs morphology is that Bi decreases the surface mobility of the In atoms on the growing surface, preventing the coalescence of the QDs. Because of its rather large covalent radius (compared with that of As), Bi is not incorporated into the QDs material segregating on the growing surface [Zvonkov et al., 2000].

3.2 Measurement techniques

Among characterization methods, optical techniques stand out because of their very unique features. These methods require little sample preparation in contrast to other techniques, such as electrical measurements (need for contacts) or structural characterization procedures (TEM) which are time consuming. The sample is generally unaltered during the measuring procedure, allowing the same sample to be analysed using several different methods, and the measurement itself does not cause damage. The optical beam is easily manipulated, which provides a mean to examine different parts of a structure and/or to two-dimensionally map properties in the plane of the sample. Spatial resolution is determined by the wavelength of the light, and the penetration depth of the light depends on its wavelength and on the sample properties, making it possible to differentiate properties along the third dimension, as the light propagates into the sample.

Optical techniques are particularly well suited to reveal the unique electronic properties of zero-dimensional systems. The size dependence of the shift and splitting of the energy states is directly visualized by the optical spectra; continuous-wave luminescence, absorption, reflection and excitation spectroscopy probe ground and excited QD electronic states, state filling, and energy relaxation amongst other properties. Carrier dynamics, namely capture, relaxation and recombination, are experimentally accessed using time-resolved PL (TRPL) [Bimberg et al., 1999].

The response of carriers in semiconductors to external applied stimuli depends directly on the electron and hole masses. The ability to modify the carrier masses, therefore, has profound implications for electronic and optoelectronic devices. In recent years, strained epitaxy has emerged as a powerful technique to modify the carrier effective mass.

Spectroscopy is basically an experimental subject and is concerned with the absorption, emission, or scattering of electromagnetic radiation by atoms or molecules.

Whenever the carrier concentrations are disturbed from their equilibrium values, they attempt to return to equilibrium. The time the carrier concentration takes to return to equilibrium depends on the carrier diffusion length (L), carrier lifetime (τ) and diffusion coefficient (D), with

$$L = \sqrt{D \cdot \tau} \quad (3.1)$$

In the case of injection of excess carriers, introduced by light or by a forward biased

pn junction, the return to equilibrium occurs through recombination of the injected minority carriers with the majority carriers.

Recombination of carriers plays an important role in semiconductor physics as well as in operation devices such as semiconductor lasers. For example, the relative importance of the radiative and non-radiative processes determines the quantum efficiency and threshold of lasers. The non-radiative process includes recombination at deep traps such as impurities or defects, recombination at the surface, Auger recombination, and leakage of minority carriers to the Ohmic contacts. Thus, both L and τ are very sensitive to the bulk and surface properties of the material, and are often used to characterize the material quality.

Although almost no sample preparation is required for the optical techniques applied during this study, some considerations have to be made regarding the acquisition of the best results. Surface smoothness and flatness are important for accurate optical measurements.

Sample cooling is also an issue to consider. Experience shows that the best optical spectra are acquired using temperatures below room temperature (RT). As the temperature is reduced, the thermal broadening of the excited carrier energies also reduces, as it goes with $k_B T$. This means that at room temperature the broadening would be of around 25 meV, going down to 6 meV at 77 K and to less than 1 meV for temperatures around liquid helium. Cooling the sample has other advantages, such as reducing the role of competing non-radiative paths for recombination, giving a higher efficiency for the PL process, which results in an improved signal-to-noise ratio and preventing impurity centres from undergoing thermal ionization.

Whenever necessary for further evaluation, the PL spectra have been corrected for the spectral response of the detector.

3.2.1 Photoluminescence

Luminescence is a widely used tool for examining intrinsic and extrinsic semiconductor properties: band characteristics, transport behaviour, impurities and defects.

The principle of PL measurements is to create carriers by optical excitation with a photon energy above the bandgap of the quantum structure, whether quantum dot or quantum well. Electrons and holes relax to their respective ground states in the conduction and valence band. They can then recombine radiatively as free carriers or

excitons.

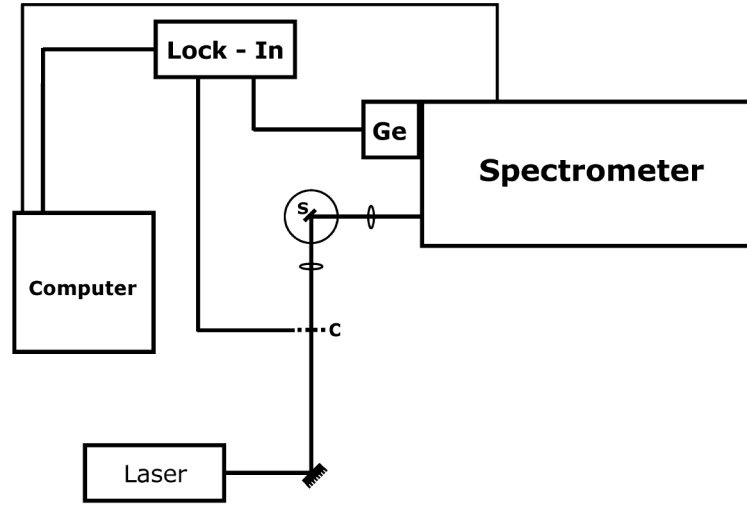


Figure 3.5: Experimental setup for PL measurements (both above-bandgap and resonant excitation) using a grating spectrometer. S \equiv sample; C \equiv chopper; Ge \equiv Germanium detector.

PL spectroscopy allows the following properties to be evaluated:

- The energy position of the PL peaks reflects the strained bandgap plus the confinement energies minus the exciton binding energy.
- The quality of the quantum structure can be evaluated through the width and intensity of the luminescence signal.
- Optical transitions between excited states may be detected for high excitation intensities.

Figure 3.5 shows a schematic representation of the experimental setup used for the PL measurements. The excitation is performed using an argon-ion (Ar^+) laser, Spectra Physics model 2016 at a wavelength ranging from 457.9 nm to 514.5 nm. Its output power can be regulated in the range of a few mW (or much less using neutral density filters) to 1.5 W. The beam from the Ar^+ laser is chopped by a mechanical chopper and then focused onto the sample. The sample is mounted on the cold finger of a closed-cycle He cryostat, kept in vacuum (10^{-5} to 10^{-6} Torr) with a vacuum system, which includes rotary and turbomolecular pumps, allowing 12 K for the lowest temperature achievable. The emission is spectrally dispersed by a 1.0 m grating monochromator, with a linear dispersion of 1.6 nm/mm, and detected with a cooled Ge pin diode using

lock-in techniques. PL was measured at sample temperatures ranging from 12 K to 300 K. The grating monochromator has been calibrated using the Ar^+ and He-Ne laser lines.

Fourier Transform Infrared Spectroscopy – FTIR

Figure 3.6 schematically represents the Fourier transform (FTIR) spectrometer (Bruker Optics IFS66v FTIR spectrometer) used in the PL experiments. A cooled Ge pin diode detector is used as detection.

A Fourier spectrometer's main components are a Michelson interferometer, an infrared source, an infrared detector, electronics and a PC for data acquisition and control of the spectrometer.

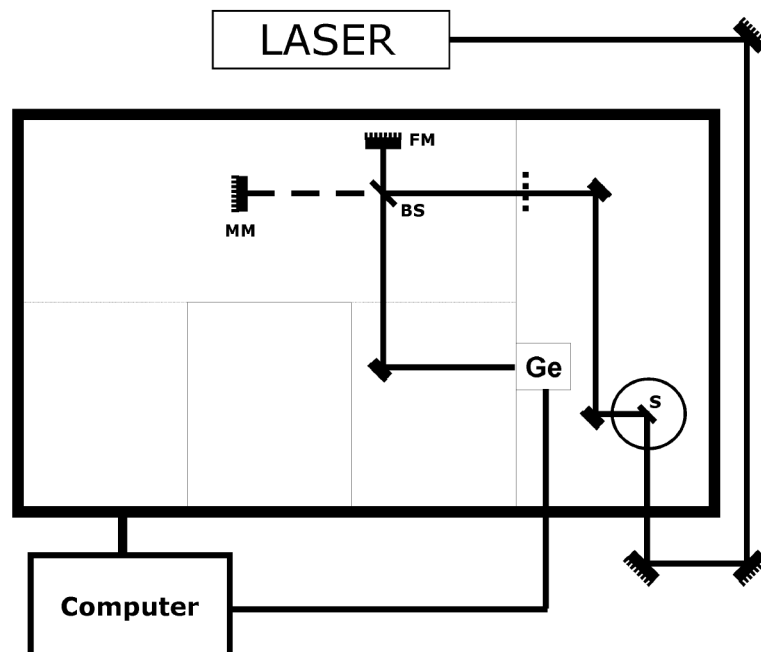


Figure 3.6: Experimental setup for PL measurements using a Fourier transform infrared spectrometer. S \equiv sample; BS \equiv beam splitter; FM \equiv fixed mirror; MM \equiv movable mirror; Ge \equiv Germanium detector. The continuous wave PL experiments were performed in a continuous flow He cryostat at temperatures between 7 and 300 K. The system is controlled by a PC.

The Michelson interferometer consists of a fixed mirror, a moving mirror and a beam splitter. After being reflected or transmitted by the beam splitter, the two beams recombine at the beam splitter after reflection at each mirror. The recombined beam then follows to the detector. There the two beams interfere and yield the total intensity.

For different positions of the movable mirror, the two partial waves get different phase shifts with respect to each other. Therefore, on the detector the radiation field is superimposed with a time-delayed copy of itself. Hence, what is basically measured when the detector signal is recorded while the mirror moves is the autocorrelation function of the radiation field (which is called the interferogram in FTIR spectroscopy). The Fourier transform of this autocorrelation function is the desired power spectrum in the frequency domain.

If the moving mirror is at the same optical distance from the beam splitter as the fixed mirror, a constructive interference takes place in the recombined beam, because the path difference is zero for all wavelengths. But if the moving mirror is displaced by a distance D , the two beams cover different distances, and the intensity of the interfered beam changes. The phase difference depends on the displacement of the mirror, D , as

$$\Phi = \frac{2\pi D}{\lambda} = 2\pi kD \quad (3.2)$$

where $k = \frac{1}{\lambda}$ is the wavenumber.

Assuming the transmission coefficient of the beam splitter to be 50 %, the detected intensity on the detector for a wavenumber k is:

$$I = 0.5I_0(1 + \cos(2\pi kD)) \quad (3.3)$$

The detector signal hence represents the interference signal of the two beams coming from the fixed and the moving mirrors and is therefore dependent on the position of the moving mirror. If the input beam is not monochromatic, but a spectrum with a spectral density $S(k)$ — which is, for a FTIR spectrometer, in the IR region — the detected intensity is

$$I(D) = 0.5 \int S(k)[1 + \cos(2\pi kD)]dk. \quad (3.4)$$

After eliminating the constant part of the signal which is independent of D , the source spectrum can be obtained by an inverse Fourier transformation

$$S(k) = 2 \int I(D) \cos(2\pi kD)dD. \quad (3.5)$$

The rapid scan function mode of the FTIR spectrometer was used during this work. In

the rapid scan mode, the mirror rapidly oscillates between the limits. The sampling of all points is done during one pass of the mirror meaning that the measuring time at each point is quite short and there is much noise in the spectrum. To obtain a better signal-to-noise ratio, a mean spectrum of multiple spectra is a result of, say, one hundred accumulations. The rapid scan mode is used for standard spectroscopy because of the following reasons: (i) the reduction of the dynamical range of the interferogram with electrical filters before the analogue-digital conversion, (ii) elimination of low frequency noise (source fluctuations, electronic and detector deviations, mechanical vibrations, etc.), and (iii) faster measurements.

The spectral resolution in FTIR is determined by the inverse of the total path of the movable mirror. In the FTIR spectrometer the calibration of the wavelength scale is done automatically through the internal He-Ne laser.

The use of a Fourier spectrometer has two main advantages [Bauer and Richter, 1996]: the multiplex advantage that results from the fact that the light coming from all spectral intervals contributes to the detector signal; and the throughput advantage, since no slit is necessary, large apertures can be realized resulting in a large throughput. These features reduce considerably the time needed to record a spectrum.

Resonant Excitation

The experiments under resonant excitation were performed using the setup of figure 3.5. The resonant excitation was possible using a tuneable Ti:Sapphire laser ($\lambda = 850\text{--}1000\text{ nm}$, Spectra Physics 3900S) which is pumped with an Ar^+ laser (Spectra Physics, model 2085, multiline, CW). PL was measured at sample temperatures ranging from 12 to 300 K. Figure 3.7 presents a diagram illustrating the photon energy ranges of the sources available for resonant excitation.

3.2.2 Photoluminescence excitation spectroscopy

PLE is a powerful tool for the characterization of an inhomogeneous QD ensemble giving access to the shape non-uniformity of the islands, the carrier relaxation processes, and non-radiative recombination. Each single PL spectrum compares QDs with different ground state transition energies, whereas in PLE a subset of the QD ensemble defined by the ground state transition energy is probed.

Through the choice of a subset of QDs with one and the same ground state energy

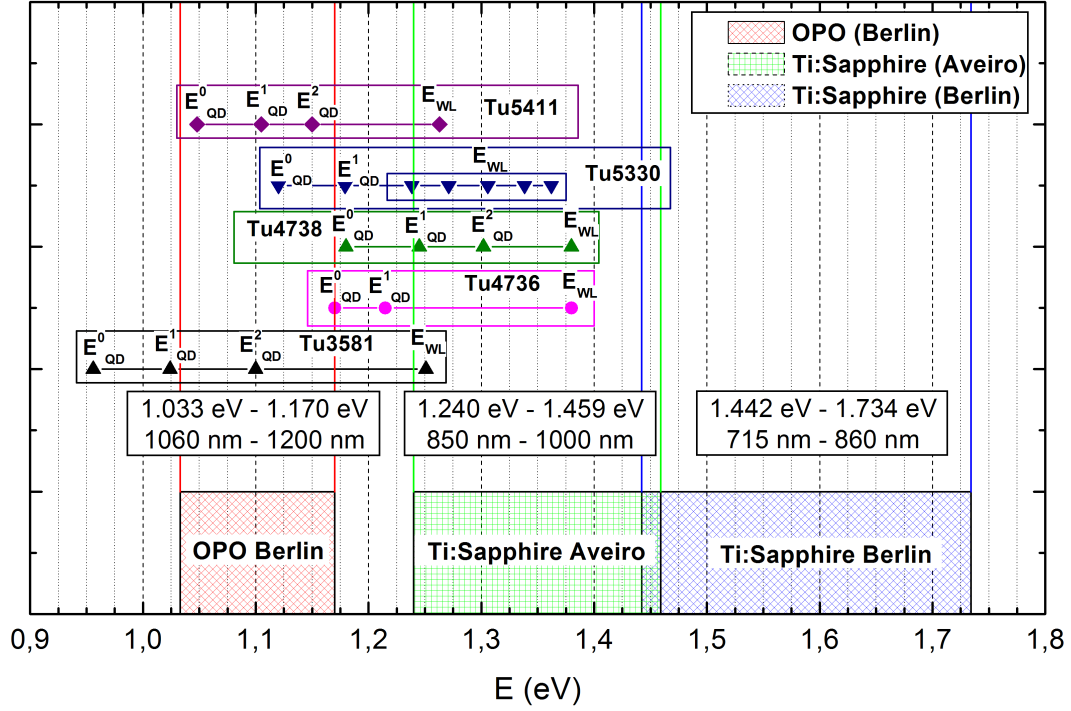


Figure 3.7: Diagram illustrating the photon energy (wavelength) ranges of the sources available for resonant excitation. The diagram includes sources available in Aveiro and Berlin at the time of the development of the experimental studies. The Ti:Sapphire laser in Aveiro was used as a resonant excitation source in PL experiments, and the OPO in Berlin was used as a resonant excitation source for the TRPL experiments. The above-bandgap excitation TRPL experiments were performed with the Ti:Sapphire laser from Berlin. The figure includes also the emission energies of some of the samples in study. The Ar^+ laser is not included since it only allowed above-bandgap excitation.

from a heterogeneous QD distribution, an improvement of the energy resolution in the investigation of the excited states is possible, as compared to the usual PL spectroscopy with above-bandgap excitation.

On the contrary to the PL spectroscopy, where the excitation energy is kept constant and the spectrum is recorded as a function of the detection energy, in the PLE spectroscopy the detection energy is kept constant and the excitation energy is varied. To ensure a PLE measurement, one has to fulfil three conditions: 1) the excitation light must be absorbed, 2) the produced electron-hole pairs (excitons) must relax into the ground state of the QD and 3) the excitons in the QD ground state must undergo radiative recombination. The main factor affecting the emission intensity in the PLE

experiments is the efficiency of the light absorption that in turn strongly depends on the density of states. That is why the absorption is strongest in the bulk matrix, typically an order of magnitude weaker in the WL and another order of magnitude weaker in the QDs. This technique offers advantages since it allows resonant excitation at important PL features such as QD or QW peaks.

Along with the excited states, also phonon-assisted processes can contribute to the PLE spectra. Therefore we usually observed in the PLE spectra of our InAs/GaAs QD samples a peak 36 meV above the detection energy caused by the LO-phonon assisted light absorption in the ground state.

Is there another non-radiative relaxation process, e.g. through the defect levels, also multi-phonon peaks can be observed [Heitz et al., 1997; Steer et al., 1996] as it occurs in our irradiated samples.

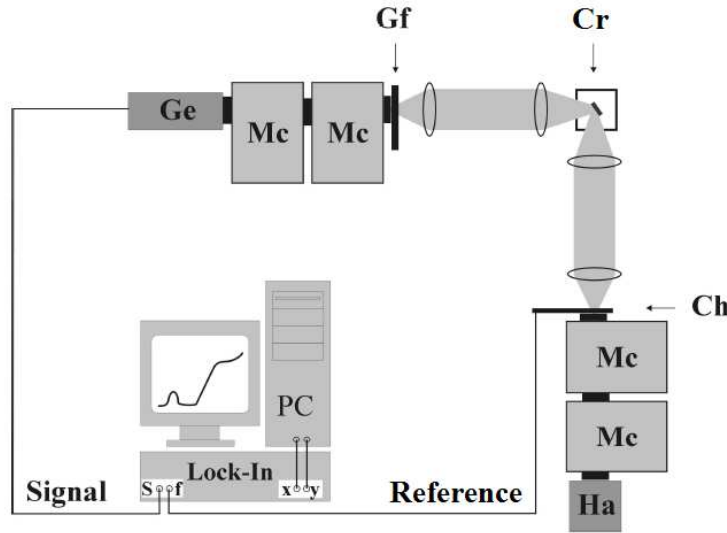


Figure 3.8: Schematic representation of the setup used, at the Institute of Solid State Physics of the Technical University of Berlin, for the PLE experiments. Cr \equiv cryostat and sample; Ch \equiv chopper; Gf = neutral density filter. The neutral density filter is used for an enhancement of the dynamical range of the system.

The PLE experiments were performed in a continuous flow He cryostat between 7 and 300 K. A tungsten lamp dispersed by a 0.27 m double-grating monochromator (Acton Research 275i) served as a low density, tunable light source. To suppress the stray light, a double monochromator (Acton Research 300i) was used for the detection of the emitted light combined with a nitrogen cooled Ge pin diode detector (North Coast, spectral range 800-1700 nm). In order to enhance the signal-to-noise ratio, a lock-in

amplifier (Stanford Research 830) was used. The spectrometer has been controlled by a PC (figure 3.8).

PLE contour plots were also acquired using this setup. In a PLE contour plot, both excitation and detection energy are varied. For every detection energy value, the excitation energy is varied from the detection energy to beyond the GaAs bandgap energy.

3.2.3 Time-resolved photoluminescence

The TRPL allows the determination of the recombination and relaxation times through the choice of the excitation and detection energies. The dynamical properties of the systems under investigation can be analysed.

In the present work, the TRPL detection was realized through the single photon counting technique. The scheme of the corresponding facility is represented in figure 3.9. In this arrangement, a standard PL facility is completed by a reference arm with a trigger diode and a rapid detector (Multi-channel plate, MCP). As a dispersion element, a subtractive grating spectrometer was used because it does not reduce the time resolution of the system. Thus, the PL dynamics could be combined with spectral selectivity.

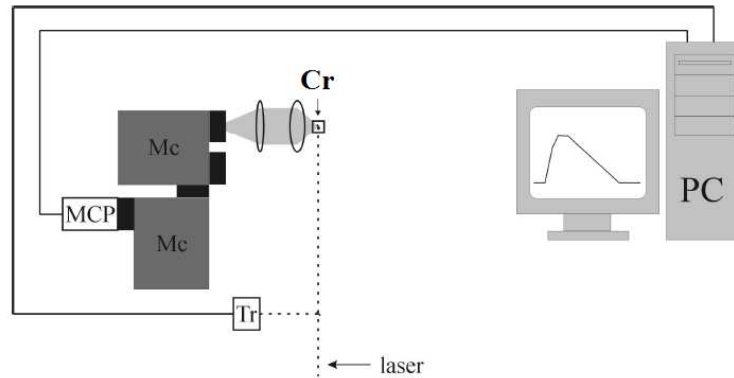


Figure 3.9: Photon counting system. Schematic representation of the setup used at the Institute of Solid State Physics of the Technical University of Berlin for the TRPL experiments. A part of the excitation laser beam is directed to the trigger diode (Tr). The laser pulses induce a resistance change of the biased diode that are transformed into voltage pulses and yield a fixed reference time for the excitation of the sample. The laser excites the sample in the cryostat (Cr), and the emitted PL is spectrally dispersed by the monochromators (Mc) and guided to the detector. The MCP (Multi-channel plate) detector transforms the incident photons into current pulses that are in turn transformed into voltage pulses by an amplifier. The registered pairs of pulses are combined to yield the time response of the observed PL.

The excitation was performed by a Ti:Sapphire laser and an Optical Parametric Oscillator (OPO) (see figure 3.10). The system functions at a fixed frequency of 80 MHz. As a pumping laser an Ar⁺ laser (450-514 nm, < 16 W, CW) has been used. The Ti:Sapphire laser (715-850 nm, < 4 W, CW and 80 MHz, < 50 fs to \approx 2 ps pulses) could be used directly as an excitation source or as a pump laser for the OPO. For the available excitation energy (wavelength) range, see figure 3.7.

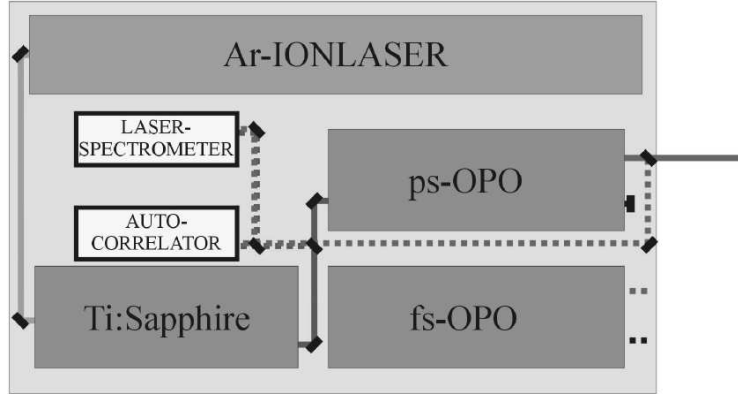


Figure 3.10: The infrared laser system. The Ar⁺ laser (multiline, 450-514 nm) continuously pumps the Ti:Sapphire laser (690-1000 nm). The latter can oscillate in the CW or pulsed (ps or fs) regime. Because of the different pulse energies in the ps and fs regimes as well as the necessary spectral compensation in the latter, there are two different OPO systems. The system with the higher requirements to the pumping intensity and beam quality is placed in a way that the beam must not be redirected. For wavelengths below 1130 nm the time drift of the autocorrelation of the OPO could be monitored.

Before striking the sample, the laser beam is divided, thus producing a reference pulse and an excitation pulse that are time correlated. The reference pulse is transformed through the trigger diode in an electrical pulse and serves as a time reference. The PL signal is dispersed by a subtractive double-grating monochromator and detected by the MCP and appears as an electrical pulse per optical event. The time calibration of the facility was performed through the detection of the excitation laser. The pulse full width at half maximum (FWHM) of the latter was 1–3 ps, i.e. much shorter than the response time of the signal electronics (\approx 18 ps). The time resolution of the detecting system was about 30 ps. The averaged excitation density within the pulse was 250 W/cm².

The samples have been mounted in a bath cryostat at 2 K in superfluid helium in order to ensure an efficient cooling under intense excitation and reduce the bubble noise.

The TRPL spectra have been evaluated using a fitting procedure based on the expo-

nential dynamics of a two-level system. The system response measured using excitation laser pulses served as a starting point for the fitting. As several transitions can contribute to the observed PL signal at a given wavelength, up to four amplitudes with corresponding time constants have been considered in the fittings. The calculated result has been fitted to the experimental one through successive iterations. The basic formula used for calculations was

$$I(t) = \int \{L(t - \mu, s) + B_2\} \cdot \sum_{i=1}^n A_i e^{(-\mu/\tau_i)} d\mu + B_1 \quad (3.6)$$

Here, $I(t)$ is the total amplitude at the time t . A_i and τ_i are the amplitudes and the time constants of different two-level systems contributing to the signal and L a correlation function. Some additional corrections are necessary. The used detector yields a timely uncorrelated background signal. The latter was determined separately and considered through the constant B_1 (equation (3.6)). The contribution of the background to the measurement of the system response was considered through the constant B_2 (equation (3.6)). The measurements of the system response and PL were performed at different detection energies and variable intensities. As the light velocity in air and glass is subjected to a dispersion, a time shift of the $t=0$ points occurs when different lenses and filters are used. This shift is accounted for through the variable s (equation (3.6)). The fitting was performed using the commercial software “Fluofit”.

3.3 Résumé

Experimental setups and growth mechanisms and techniques were briefly reviewed in this chapter. Growth methods and conditions were also reported. The Stranski-Krastanow growth mode and the Metal-Organic Chemical Vapour Deposition were the techniques presented. Several experimental methods were used to characterize the samples under study. The techniques employed and discussed in this chapter were: photoluminescence with above-bandgap and resonant excitation, photoluminescence excitation and time-resolved photoluminescence spectroscopy.

Bibliography

- Bauer, G. and Richter, W., editors (1996). *Optical Characterization of Epitaxial Semiconductor Layers*. Springer Verlag.
- Bimberg, D. (2001). In *Proceedings of the 28th International Symposium on Compound Semiconductors*, page 485, Tokyo, Japan.
- Bimberg, D., Grundmann, M., and Ledentsov, N. (1999). *Quantum Dot Heterostructures*. John Wiley & Sons, Chichester.
- Dutta, M. and Pamulapati, J. (1993). *Properties of lattice – matched and strained Indium Gallium Arsenide*, page 199. inspec.
- Gerard, J.-M. (1992). *Applied Physics Letters*, 61:2096.
- Goldstein, L., Glas, F., Marzin, J., Charasse, M., and Le Roux, G. (1985). *Applied Physics Letters*, 47:1099.
- Heinrichsdorff, F., Grundmann, M., Stier, O., Krost, A., and Bimberg, D. (1998a). *Journal of Crystal Growth*, 195:540.
- Heinrichsdorff, F., Krost, A., Bimberg, D., Kosogov, A., and Werner, P. (1998b). *Applied Surface Science*, 123/124:725 – 728.
- Heinrichsdorff, F., Krost, A., Grundmann, M., Bimberg, D., Bertram, F., Christen, J., Kosogov, A., and Werner, P. (1997). *Journal of Crystal Growth*, 170:568.
- Heinrichsdorff, F., Krost, A., Grundmann, M., Bimberg, D., Kosogov, A., and Werner, P. (1996). *Applied Physics Letters*, 68:3284.
- Heitz, R., Veith, M., Ledentsov, N., Hoffmann, A., Bimberg, D., Ustinov, M., Kop'ev, P., and Alferov, Z. (1997). *Physical Review B*, 56:10435.
- Joyce, P., Krzyzewski, T., Bell, G., Jones, T., Le Ru, E., and Murray, R. (2001). *Physical Review B*, 64:235317.
- Karpovich, I., Zvonkov, B., Baidus, N., Tikhov, S., and Filatov, D. (2004). *Trends in Nanotechnology Research*, chapter Tuning the energy spectrum of the InAs/GaAs Quantum dot structures by varying the thickness and composition of a thin double GaAs/InGaAs cladding layer, page 173. Nova Science, New York.

- Ledentsov, N., Bimberg, D., Ustinov, V., Alferov, Z., and Lott, J. (2002). *Japanese Journal of Applied Physics*, 41:949.
- Leon, R., Lobo, C., Liao, X., Zou, J., Cockayne, D., and Fafard, S. (1999). *Thin Solid Films*, 357:40.
- Pereira, S. (2005). private communication.
- Reithmaier, J.-P., Riechert, H., Schlötterer, H., and Weimann, G. (1991). *Journal of Crystal Growth*, 111:407.
- Sellin, R. (2003). *Metalorganic Chemical Vapor Deposition of High-Performance GaAs-Based Quantum-Dot Lasers*. PhD thesis, von der Fakultät II – Mathematik und Naturwissenschaften – der Technischen Universität Berlin, Berlin.
- Steer, M., Mowbray, D., Tribe, W., Skolnick, M., Sturge, M., Hopkinson, M., Cullis, A., Whitehouse, C., and Murray, R. (1996). *Physical Review B*, 54:17738.
- Stringfellow, G. (1999). *Organometallic Vapor-Phase Epitaxy*. Academic Press, 2nd edition.
- Toyoshima, H., Niwa, T., Yamazaki, J., and Okamoto, A. (1993). *Applied Physics Letters*, 63:821.
- Wang, S., Andersson, T., and Ekenstedt, M. (1991). *Applied Physics Letters*, 59:2156.
- Wikipedia (2010). Stranski-krastanow growth. <http://en.wikipedia.org/wiki/Stranski-Krastanov-growth>.
- Zvonkov, B., Karpovich, I., Baidus, N., Filatov, D., Morozov, S., and Gushina, Y. (2000). *Nanotechnology*, 11.

BIBLIOGRAPHY

Chapter 4

Characterization of the as-grown samples

4.1 Laser structures

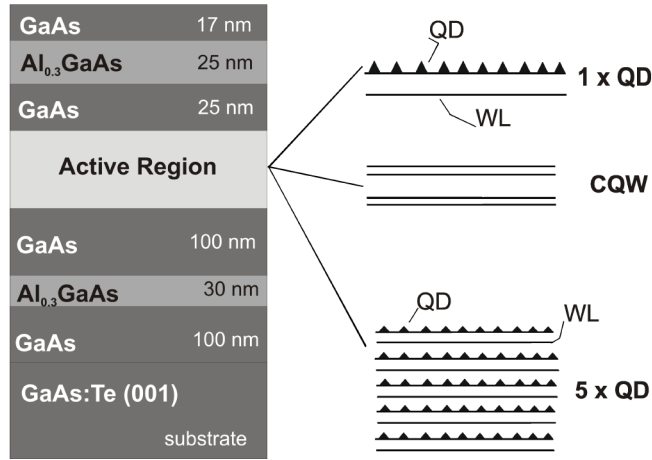


Figure 4.1: Layer sequence of the laser structure samples.

Three types of samples were grown using MOCVD under identical conditions according to the layer sequence shown in figure 4.1. The samples differ only with respect to the active region: sample 1×QD is composed of one layer of self-assembled InAs/GaAs QDs on a thin WL; sample CQW is formed by two coupled InAs QWs separated by 1 nm GaAs; sample 5×QD contains five QD layers separated by 20 nm GaAs. The active layer together with the GaAs cladding layers is placed between two Al_{0.3}Ga_{0.7}As barriers for the optimization of carrier capture since this kind of layer sequence is used

in laser structures [Heinrichsdorff et al., 1997b]. The structure was grown on top of a GaAs substrate and a GaAs buffer layer. TEM results on similar samples give typical QD densities of $5 \times 10^{10} \text{ cm}^{-2}$ [Heinrichsdorff et al., 1998b, 1997b,c].

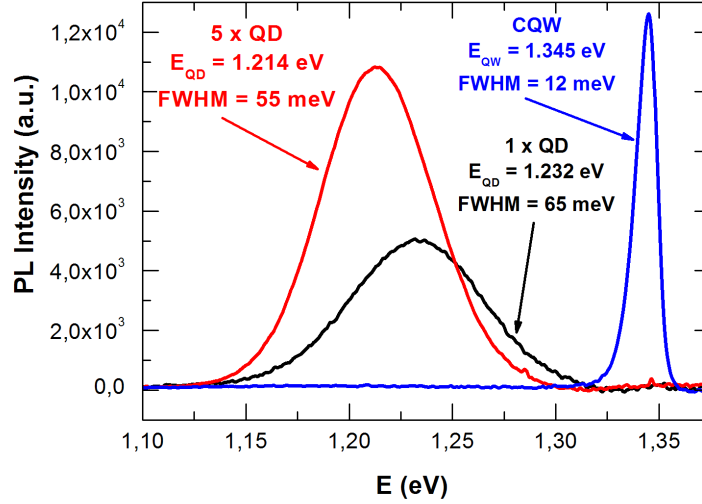


Figure 4.2: FTIR PL spectra of as-grown (before irradiation) samples 1×QD, CQW and 5×QD measured at 10 K upon excitation with the 457.9 nm line of an Ar^+ laser. The PL intensity is normalized to the excitation power. The latter did not exceed $\approx 10^2 \text{ W/cm}^2$ to avoid PL and detector saturation.

Upon excitation above the GaAs bandgap (1.5192 eV at $T = 2 \text{ K}$ [Madelung, 1987]) with the 457.9 nm (2.7 eV) line of an Ar^+ laser, strong QW and QD PL bands emerge due to exciton transitions involving electrons and holes in the ground state (figure 4.2). The QD emissions lead, for samples 5×QD and 1×QD, to peaks at 1.214 and 1.232 eV with FWHMs of 55 and 65 meV, respectively. Sample CQW exhibits a PL emission at 1.345 eV with a FWHM of 12 meV (figure 4.2). The QD PL peaks are of Gaussian shape (see fittings in figure 4.3).

The growth of several layers of QDs allows a significant increase of the total number of QDs, giving rise to an enhancement of the QD PL intensity, as shown in figure 4.2 for sample 5×QD. The barrier thickness determines the degree of vertical alignment and electronic coupling. Sample 5×QD has 20 nm thick GaAs barriers between layers of QDs. For this thickness the alignment is already lost, as shown by TEM results in similar samples [Heinrichsdorff et al., 1997b; Xie et al., 1995].

No PL due to excited states or WL could be seen at low excitation densities, indicating rapid carrier transfer from the WL to the QDs and high density of dots. A slightly larger

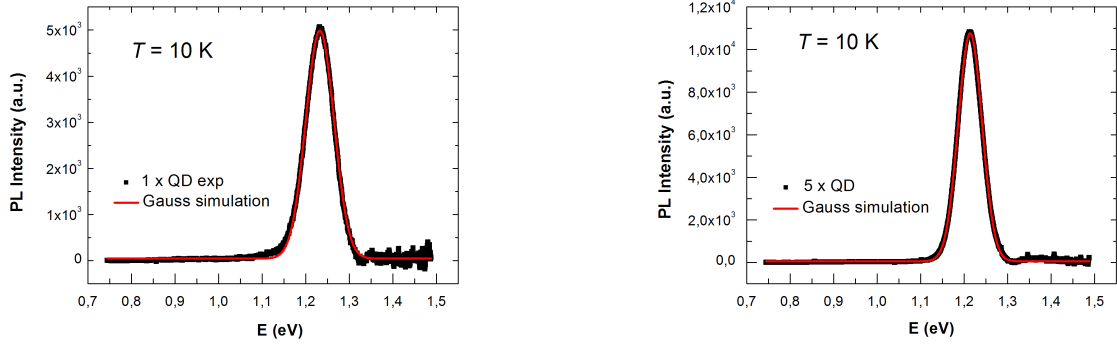


Figure 4.3: PL spectra of samples 1×QD (left) and 5×QD (right), both as-grown, showing the fit used to determine the peak position and FWHM. A Gaussian function was used to perform the fit.

average InAs island size in sample 5×QD as compared to sample 1×QD can be inferred from the peak energy position, as well as a higher homogeneity of the dots from the FWHM. Each QD has its particular set of energy levels. The distribution of these levels among the QD ensemble gives rise to different values of FWHM. For larger ensembles of QDs, the inhomogeneous line broadening may be due to fluctuations of size, shape, and chemical composition [Bimberg et al., 1999]. The shape of the QDs is the main factor governing the strain distribution, not the size [Grundmann et al., 1995]. Theoretical calculations performed using effective mass approximation [Grundmann et al., 1995] and eight-band k·p theory [Stier et al., 1999] predict for the observed QD ground state energies (figure 4.2) pyramid base lengths of 9 and 10 nm, respectively. The different base length values are related to different band offsets used in the calculations. According to the latter, it was not possible to establish different pyramid base length for the samples under study due to the small difference between the peak energies. An important note is that both calculations were performed for pyramid shape QDs and not for truncated pyramids. The luminescence efficiency obtained from these QD arrays is similar to that of the QW sample. The predicted primary consequence of a phonon bottleneck, completely quenched luminescence efficiency [Benisty et al., 1991] is not observed. As proposed in many different works, several relaxation mechanisms can provide the non-existence of this phonon bottleneck (see discussion of the carrier dynamics in section 6.2).

Figure 4.4 shows the temperature dependence of the integrated PL intensity (top), FWHM (middle) and peak position (bottom) of the QD or QW emission, according to the sample. For the QD samples, the FWHM goes to a minimum value at a temperature of ≈ 150 K in agreement with other works on similar samples [Lubyshev et al.,

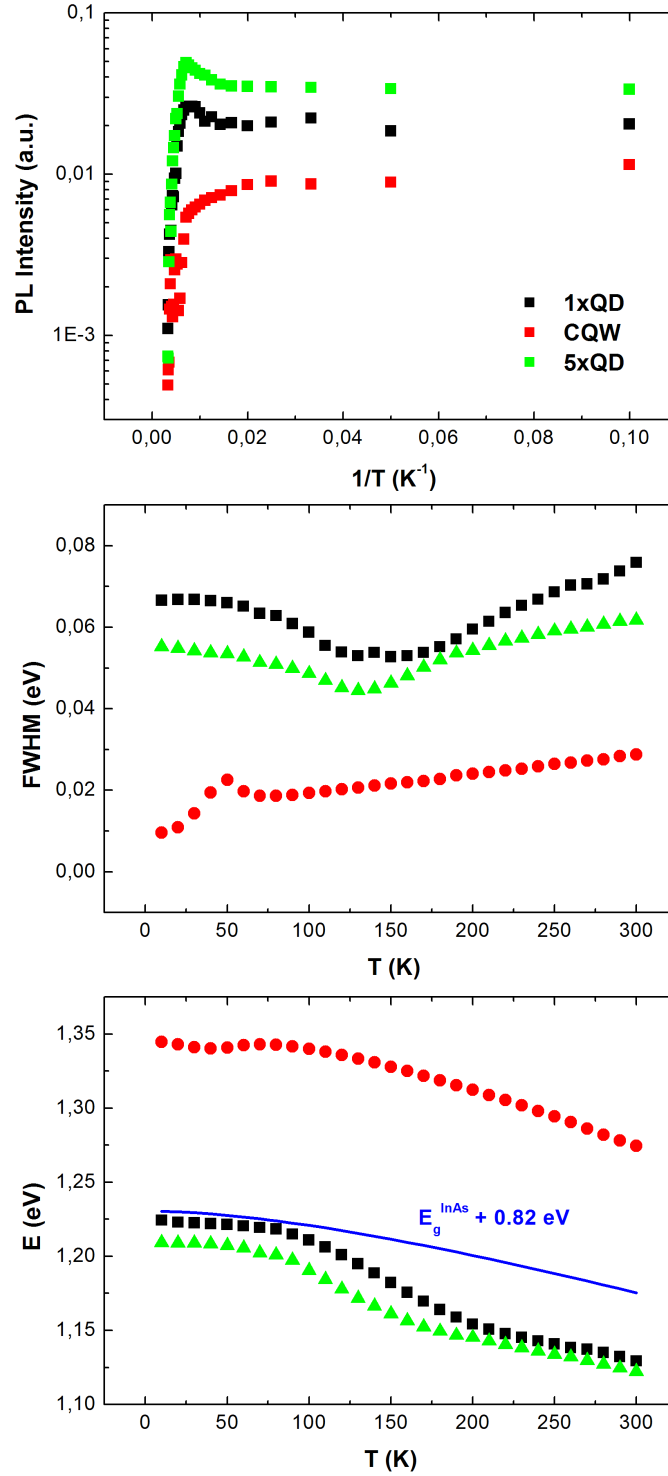


Figure 4.4: Temperature dependence, between 10 and 300 K, of the PL characteristics for the as-grown samples 1×QD, CQW and 5×QD. Top: integrated PL intensity, middle: full width at half maximum (FWHM), and bottom: QD or QW band peak position. For comparison the variation of the InAs bandgap (+0.82 eV), calculated using Varshni's law with the InAs parameters [Varshni, 1967], is shown as a blue line in the bottom graph of the figure.

1996; Patanè et al., 1997; Xu et al., 1998]. Assuming a uniform energy barrier of the wetting layer, the thermal activation energy differs from dot to dot due to the size distribution. As the temperature increases, excitons at shallow potential minima can easily be thermally activated out to the energy barrier produced by the wetting layer, and then recombine radiatively or non-radiatively there, and/or transfer and relax into energetically low-lying states. Consequently, high energy components in the PL spectrum shrink much faster than the low energy components, resulting in the fast red shift of the PL peak energy, faster than for the InAs energy gap (see figure 4.4 bottom), and reduction of the FWHM (figure 4.4 middle). The carrier redistribution between dots is also evident from the temperature dependence of the integrated PL intensity (figure 4.4 top). As the PL line width (FWHM) shrinks, the integrated PL intensity reaches a maximum due to carriers feeding into the lower energy dots from the higher energy ones. This redistribution of carriers between dots can also explain the behaviour of the QD band position with temperature as referred before. If this redistribution process would be absent, the QD PL peak position would follow the band-gap thermal shrinkage for all temperatures, as has been seen in the temperature dependence of the absorption-like spectra [Aigouy et al., 1997].

The exponentially decreasing temperature dependence of the QD PL intensity observed for samples TU3904 and TU3972 is quite common and has been modelled in several publications [Altieri et al., 2002; Brusaferrri et al., 1996; Chang et al., 2005; Le Ru et al., 2003; Lee et al., 2008; Wasilewski et al., 1999; Wei et al., 2005]. The main problem is that for similar samples, quite different results have been found. For a discussion of the influence of defects on the temperature dependence of the PL intensity see chapter 7.

4.2 Samples with non-uniform WL thickness

Some samples studied in this thesis had a non-uniform WL thickness. In these samples the WL assumes a complex structure containing growth islands. The latter have different thicknesses, going from 5 to 9 ML. The occurrence of this monolayer splitting of the WL is dependent on the substrate temperature during the growth [Heinrichsdorff et al., 1996]. These samples were used to gain additional insight into the influence of the WL thickness on the thermal carrier/exciton redistribution within the QDs.

The samples used were grown by MOCVD and have the following structure (figure 4.5): a GaAs buffer layer was grown on top of a GaAs:Te substrate, the active layer

4.2. SAMPLES WITH NON-UNIFORM WL THICKNESS

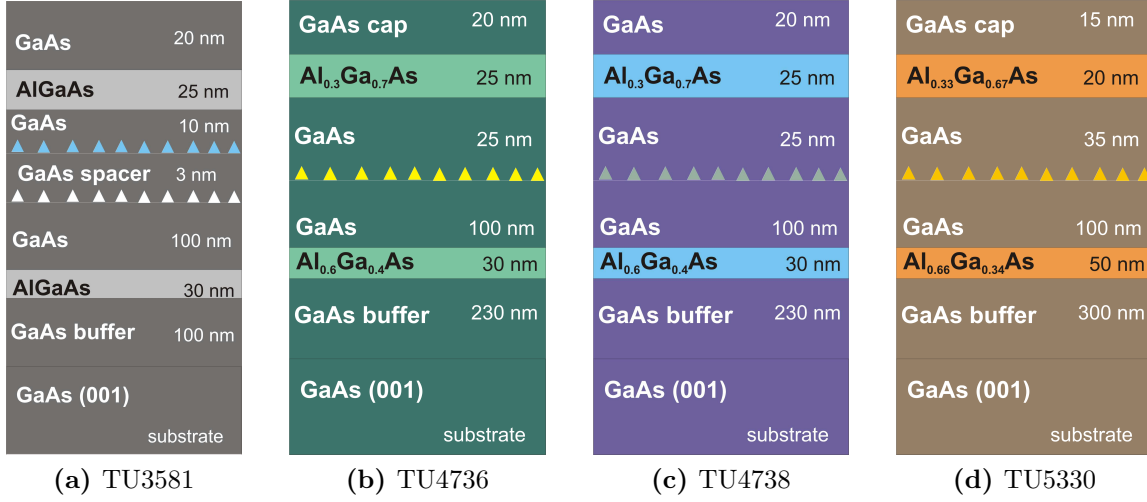


Figure 4.5: Layer sequence of the samples with non-uniform WL thickness. The active layers are composed of $\text{In}_{0.6}\text{Ga}_{0.4}\text{As}$ QDs grown at temperatures between 490 and 525 °C. Layer thicknesses and compositions are indicated in the diagrams.

together with GaAs cladding layers were placed between two AlGaAs barriers, with a GaAs capping layer on top of the whole structure. After the active layer growth, an interruption between 4.6 and 16.6 s was performed in order to allow the QDs to grow [Heinrichsdorff et al., 1997a].

Sample TU3581 has a low density of QDs, less than the other samples of this group, with large-size QDs. In the TEM image (figure 4.6), two classes of three-dimensional objects can be distinguished. Besides the QDs, large clusters can be observed with no uniform shape and which size is far beyond the critical size for dislocation generation. Thus, the strain is relieved by plastic relaxation and a minimization of strain energy plays no role for these clusters.

Samples TU4736 and TU5330 have a dot density of $\approx 10^9 \text{ cm}^{-2}$ and sample TU4738 has a dot density $< 10^9 \text{ cm}^{-2}$, all samples with an active layer composed by a single QD layer.

Figures 4.7, 4.8 and 4.9 show PL spectra of the as-grown sample TU5330 taken at 10, 70, and 300 K, respectively. The spectra were obtained at a FTIR spectrometer with the 457.9 nm line of an Ar^+ laser as excitation source and detected by a liquid-nitrogen cooled Ge detector. The sample was mounted in a He flux cryostat that allows measurements in the temperature range from 10 to 300 K. In each spectrum, QD and WL emission energies are identified. The energy peaks were determined using Gaussian

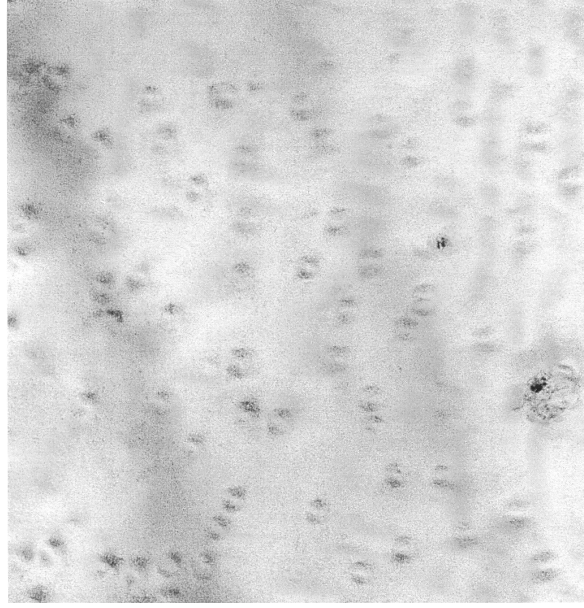


Figure 4.6: Plan view TEM image of sample TU3581.

fit functions (green curves in the figures) for each emission.

At 10 K, the luminescence of the QD ensemble appears as a double-peaked band centred between 1.1 and 1.2 eV. The low-energy peak at 1.120 eV with a FWHM of 46 meV corresponds to the ground state transition; the peak at 1.179 eV originates from excited states and is visible due to state filling effects favoured by the low QD density [Grundmann et al., 1996] and the slowed down relaxation from the first excited to the ground state, as will be discussed in section 6.4.1. For lower excitation densities, the peak at 1.179 eV is absent. The more dominant feature of the spectrum is a multi-peaked band with the individual maxima centred between 1.238 and 1.362 eV which stem from the WL. Beside the two main peaks at 1.306 and 1.338 eV, three additional peaks can be observed. All these peaks are attributed to a monolayer (ML)-sized splitting of the WL.

At 70 K, the same structure of bands is observed (figure 4.8), though here the resolution is worse than at 10 K. At 300 K, another QD-related band arises which is attributed to the second excited state (figure 4.9). The QD emission is now stronger than the WL emission. This is so due to the lower localization energy for the carriers in the WL and to the higher thermal excitation energy available at room temperature.

Similar results were observed for other samples (see an example in figure 4.10). Figure 4.10a shows PL spectra of sample TU4738 taken at different temperatures indicated in

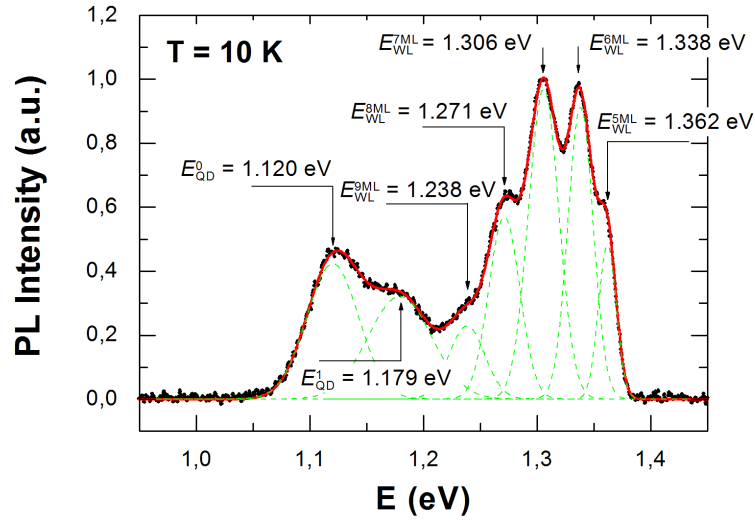


Figure 4.7: PL spectrum of the as-grown sample TU5330 taken at 10 K.

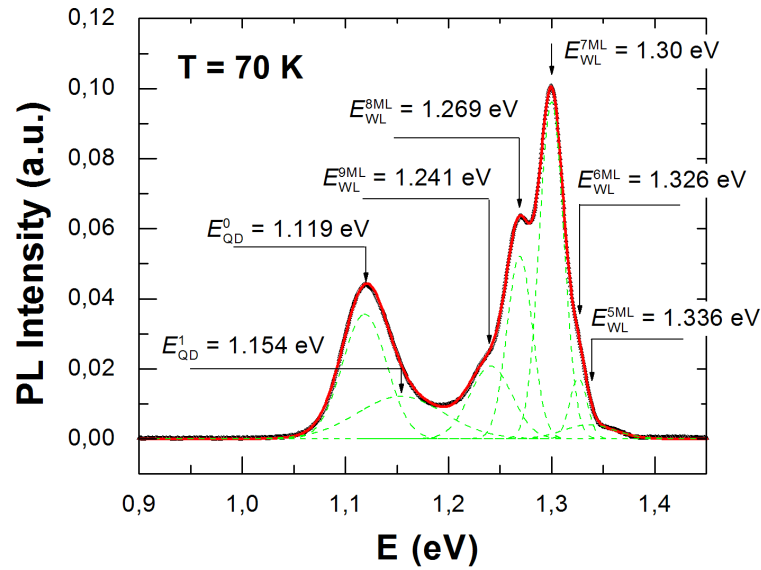


Figure 4.8: PL spectrum of the as-grown sample TU5330 taken at 70 K.

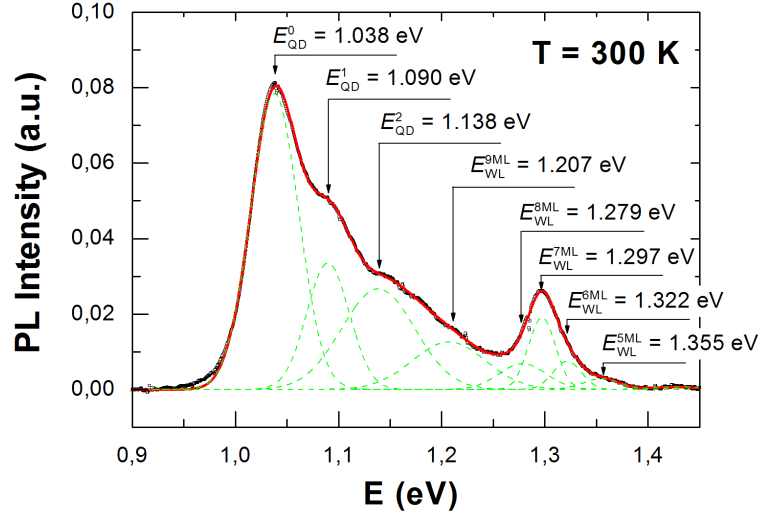


Figure 4.9: PL spectrum of the as-grown sample TU5330 taken at 300 K.

the figure. The curves are vertically shifted for clarity. The WL PL emission quenching is visible and only one rather broad band remains at 300 K. At 70 K (figure 4.10b) one emission band from QDs and four emission bands from the WL can be identified.

Samples TU4738 and TU4736 are very similar. The main difference is the dot density which can be corroborated by the intensity of the QD PL band, since TU4736 has a higher density and hence a higher relative QD PL intensity (figure 4.11).

Sample TU3581 has the largest QD size which can be inferred from the lowest QD peak energy, around 0.95 eV at 300 K.

Figure 4.12a shows PL and PLE spectra of the as-grown sample TU5330 taken at 7 K. The PL spectrum was obtained with above-GaAs bandgap excitation. The PLE spectrum was detected at the QD PL maximum. In this spectrum a GaAs LO-phonon emission can be observed. From this spectrum it can be concluded that the QD ground state is fed with carriers from the GaAs barrier, the WL and the QD excited states. Figure 4.12b shows a PLE contour plot of the same sample. For the as-grown sample no resonance at the QD first excited state can be observed. For a more detailed discussion of these results see section 6.4.

To study in more detail the emissions attributed to the WL, PL spectra were taken at temperatures between 10 K and room temperature. The temperature dependence of the integrated intensities of the different PL peaks is displayed in figure 4.13. The

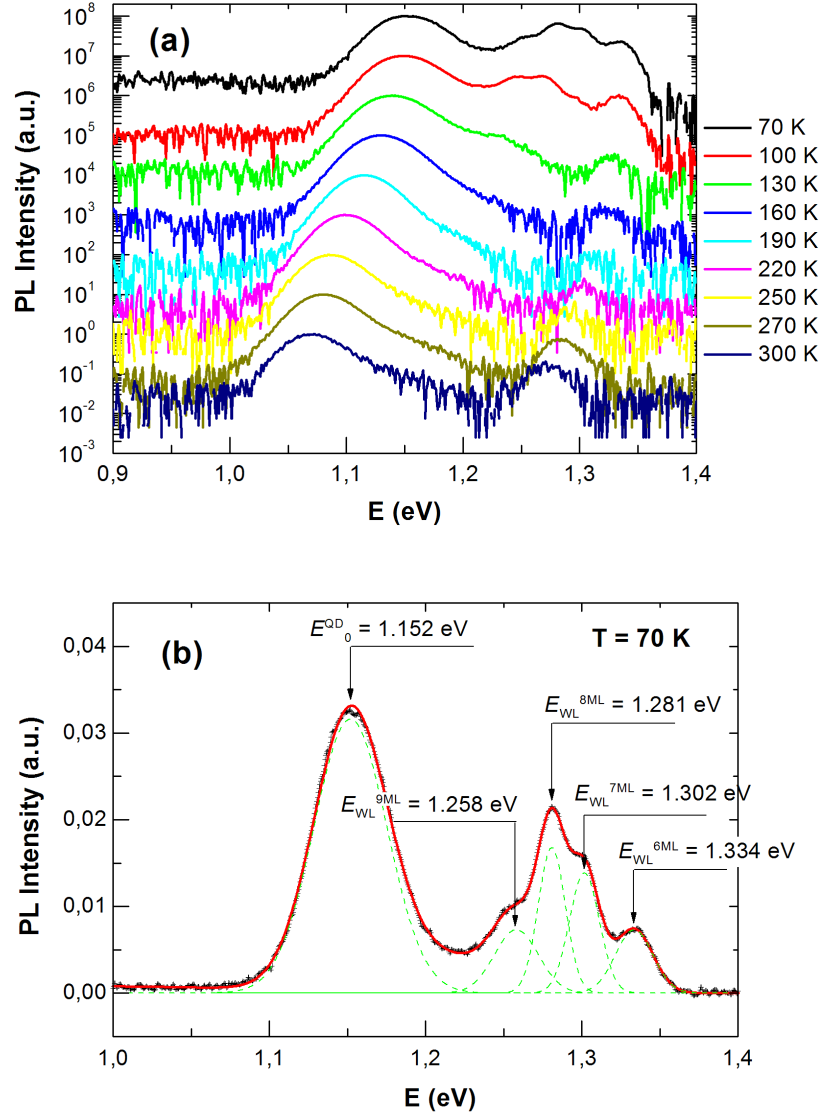


Figure 4.10: (a) PL spectra of the as-grown sample TU4738 taken at different temperatures as indicated in the figure. Note the logarithmic intensity scale. The curves are vertically shifted for clarity. (b) PL spectrum of the same sample taken at 70 K with indication of the peak positions for the QD ground state- and WL-related emissions.

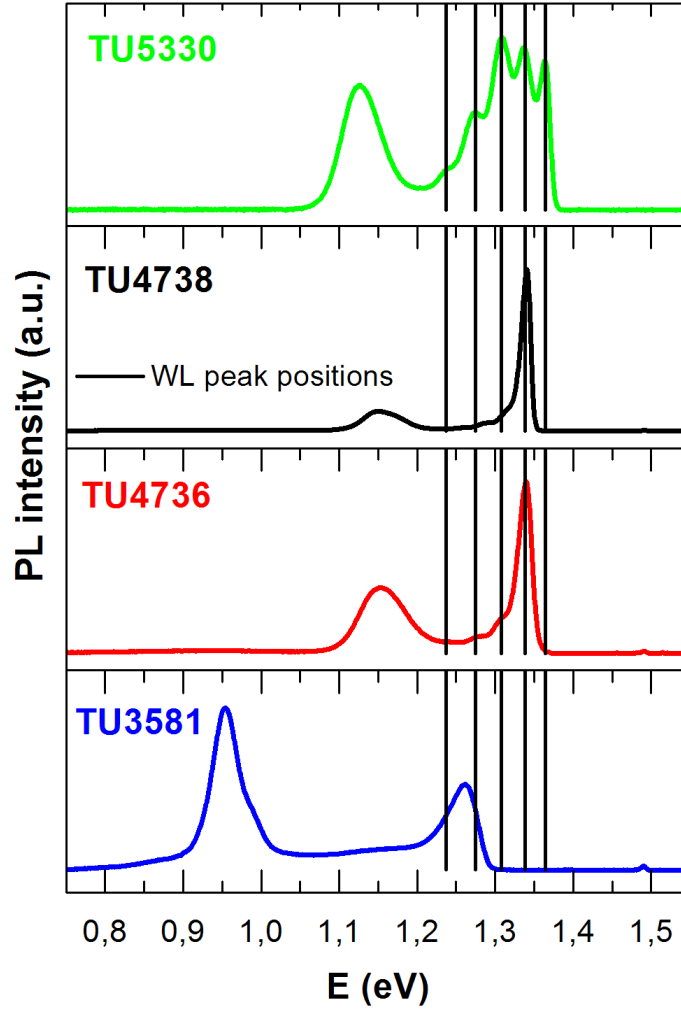


Figure 4.11: PL spectra of different as-grown samples taken at 10 K. The vertical lines indicate the WL peak positions for 5, 6, 7, 8, and 9 ML thick WL islands determined for the sample TU5330.

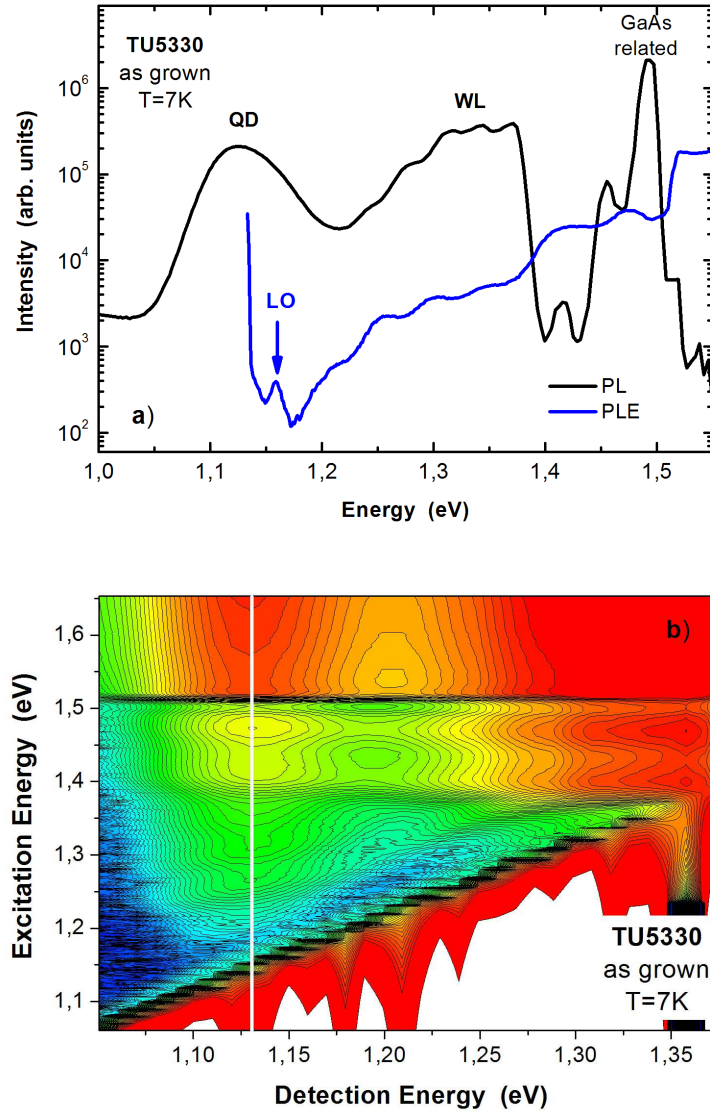


Figure 4.12: (a) PL and PLE spectra of the as-grown sample TU5330 taken at 7 K. QD-, WL- and GaAs-related emission bands are identified. (b) Contour plot of the QD PL intensity measured at 7 K as a function of the detection and the excitation energy for the as-grown sample TU5330. The white line denotes the position of the QD ground state emission maximum.

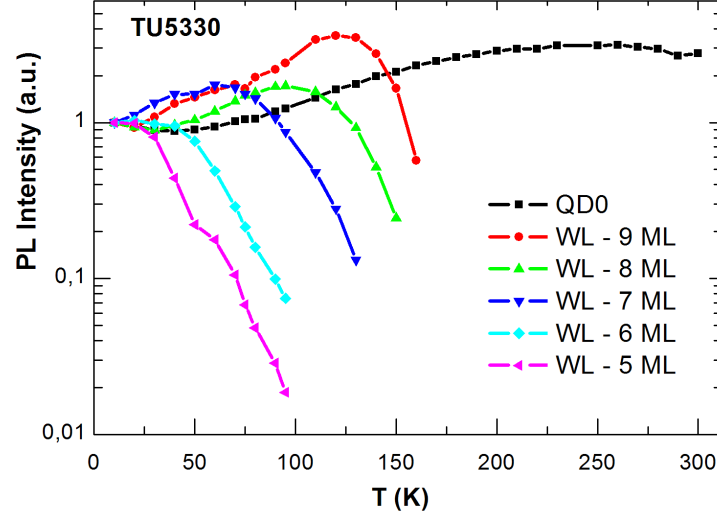


Figure 4.13: Temperature dependence of the integrated PL intensity for different identified QD and WL emissions for the as-grown sample TU5330. For peak positions at 10 K see figure 4.7. The intensities were all normalized to the 10 K value.

intensity of the luminescence of the 5 and 6 ML WL parts drops continuously with rising temperature. The intensities related to the 7, 8 and 9 ML thick WL regions rise with increasing temperature up to a certain point and then drop quite quickly. The temperature at which the luminescence intensity reaches its maximum is the higher the thicker the WL region is. It is a manifestation of the Maxwell-Boltzmann distribution of excitons over WL parts of different thickness and, consequently, different well depths. With increasing temperature the peaks attributed to the thicker parts of the WL gain luminescence intensity (figure 4.13) at the expense of the peaks of the thinner parts. Above 150 K the luminescence of the WL peaks disappears completely. The intensity of the QD peak rises continuously with increasing temperature until 260 K, starting to decrease after that.

4.3 TU5411: dots-in-a-well structure

Sample TU5411 was grown using MOCVD and has the structure seen in figure 4.14. After the 200 nm GaAs buffer layer grown on top of a GaAs substrate, an AlGaAs barrier followed by 100 nm GaAs were grown at 600 °C. Subsequently, the temperature was lowered to 485 °C for the deposition of ≈ 2.1 monolayers (ML) of InAs forming

the initial InAs islands. The islands were capped by a 2 nm thick $\text{In}_{0.25}\text{Ga}_{0.75}\text{As}$ layer. Finally, the temperature was raised to 600 °C for the growth of 50 nm GaAs, an AlGaAs barrier and a 20 nm GaAs protection layer. The lateral density of the QDs determined from plane-view TEM images was $\approx(3-5)\times 10^{10} \text{ cm}^{-2}$. The InAs QDs are embedded in a QW formed by the original InAs WL and the $\text{In}_{0.25}\text{Ga}_{0.75}\text{As}$ cap layer. For the investigated samples TEM results suggest a flat truncated shape of the overgrown InAs QDs with a base length between 12 nm and 14 nm and an estimated height around 3 nm.

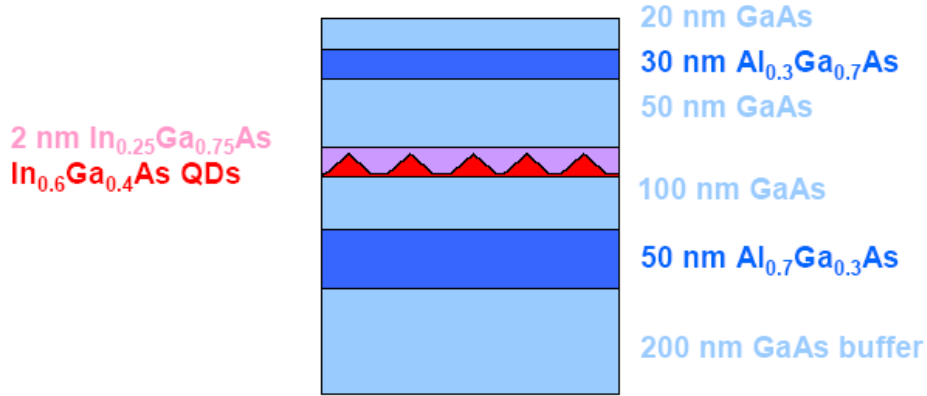


Figure 4.14: Layer sequence of the sample TU5411.

The high QD density does not allow the observation of PL bands related to excited states in a low excitation regime. Figure 4.15 shows a FTIR PL spectrum of sample TU5411 taken at 10 K upon excitation with the 488 nm line of an Ar^+ laser. A single QD band is observed at 1.04 eV. The other energy positions identified, $E = 1.12 \text{ eV}$ and $E = 1.14 \text{ eV}$, are assigned to sub-levels of the first excited state which have been investigated in the TRPL experiments described in section 6.4. This sample was measured at TU Berlin by Dr. Roman Sellin in the high excitation regime, using an excitation power of 500 mW, at room temperature, and two excited states and a WL band could be identified (figure 4.16). The emission around 1.4 eV is GaAs-related.

Figure 4.17 shows PL and PLE spectra of the as-grown sample TU5411 taken at 7 K. The PL spectrum was obtained with above-bandgap excitation. A band originating at the QD ground state and the GaAs barrier-related emission can be identified in this spectrum. The PLE spectrum was detected at the QD PL maximum position. It shows LO-phonon-assisted ground state absorption at 1.08 eV, two bands arising from the first and second excited QD states and a WL/QW-related band around 1.3 eV.

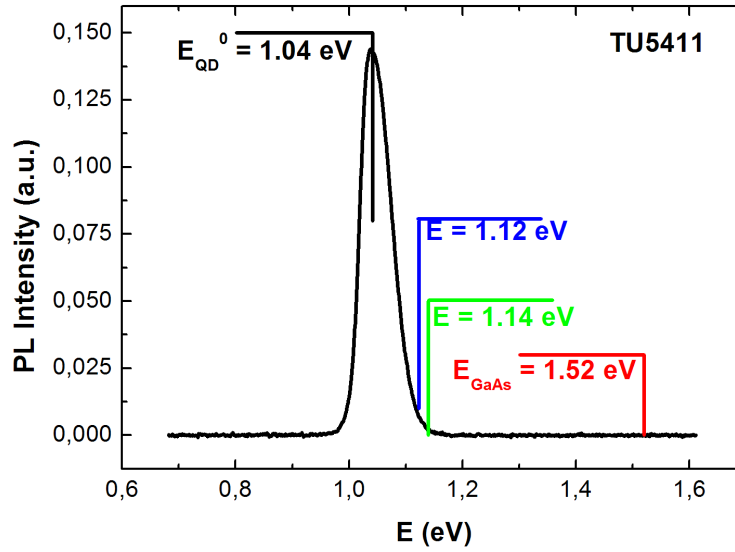


Figure 4.15: FTIR PL spectrum of the as-grown sample TU5411 taken at 10 K upon excitation with the 488 nm line of an Ar^+ laser.

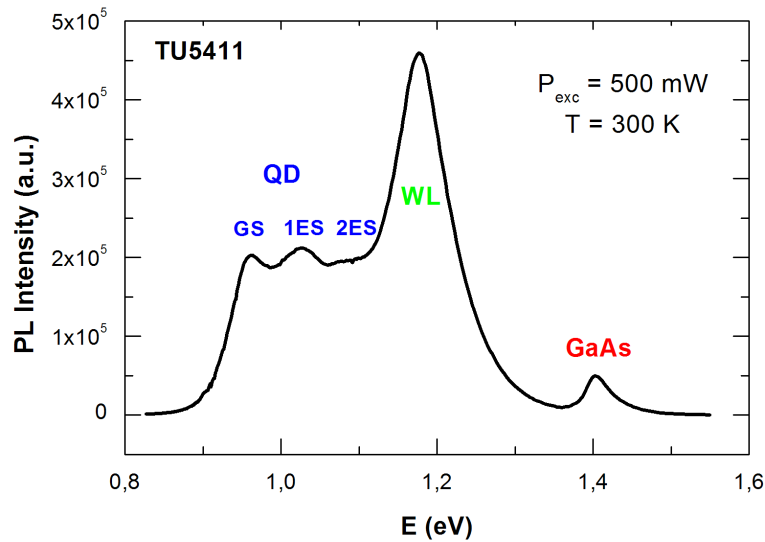


Figure 4.16: PL spectrum of the as-grown sample TU5411 taken at 300 K with an excitation power of 500 mW. This spectrum was obtained at TU Berlin and kindly made available by Dr. Roman Sellin.

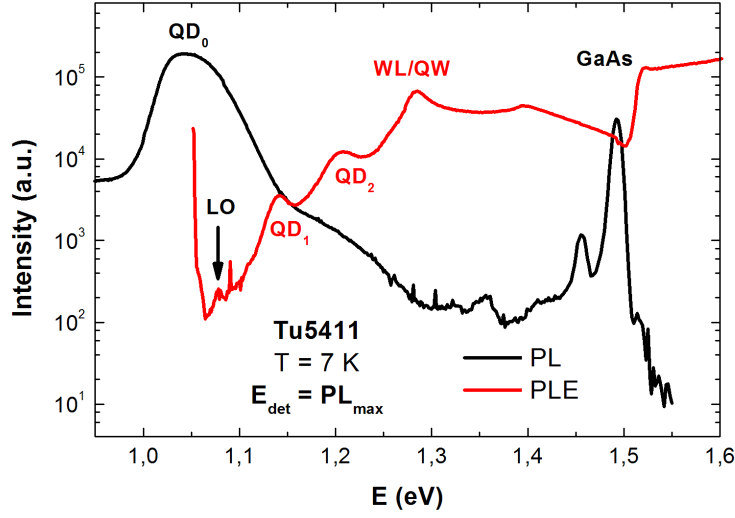


Figure 4.17: PL and PLE spectra of the as-grown sample TU5411 taken at 7 K. For the PLE spectrum the detection energy was set at the QD PL maximum position. The PL spectrum was obtained with above-bandgap excitation.

4.4 Other dots-in-a-well structures with different cap layer thicknesses

Table 4.1: Sample characteristics.

Sample	d_c (nm)	L (nm)	x
NN3649	5	4	0.2
NN3652	5	2	0.2
NN3653	5	2	0.3
NN3654	5	4	0.3
NN3753	20	2	0.3
NN3756	5	2	0.3
NN3760	10	2	0.3
NN3761	7	2	0.3
NN3762	3	2	0.3

Growing the InAs/GaAs QDs emitting in the optical silica glass fibre transparency windows at 1.3 (0.9 eV) and 1.55 μm (0.8 eV) still remains an important technological problem. One of the approaches to this problem is growth of an $\text{In}_x\text{Ga}_{1-x}\text{As}$ quantum well over the QDs, which results in a red shift of the QD ground state [Kovsh et al.,

1999; Nishi et al., 1999; Volovik et al., 1999]. The samples studied differed in thickness and In content of the QW overgrowing the dots as well as the thickness of the capping layer. This study allowed a better understanding of the influence of the parameters referred before on the energy spectrum of the QDs.

The samples used in this study were grown at Nizhny Novgorod University by atmospheric pressure metal organic vapour phase epitaxy (AP-MOVPE). On top of the GaAs substrate, a 600 nm GaAs buffer layer was grown. Then the deposition of InAs began in order to form a wetting layer and the QDs layer. An InGaAs layer was grown on top of the QDs, placed between the QDs layer and the GaAs cap layer (see figure 4.18). Differences between samples (see figure 4.18 and table 4.1) are related to variations of the QW thickness (L), QW indium content (x) and GaAs capping layer thickness (d_c).

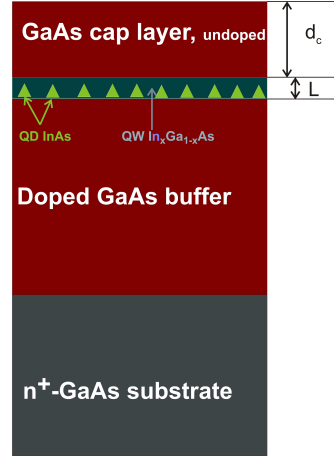


Figure 4.18: Layer sequence of the samples with different cap layer thicknesses. Samples are labelled after table 4.1, where d_c is the cap layer thickness, L is the $\text{In}_x\text{Ga}_{1-x}\text{As}$ QW thickness and x is the In content in the QW.

As expected, decreasing the GaAs cap layer thickness results in a red shift of the ground state transition energy (figures 4.19 and 4.20) due to increased compressive strain, but the emission intensity from the capped QDs is enhanced as fewer carriers undergo non-radiative recombination at surface states [Saito et al., 1998]. No emission from the WL or the QW was observed at room temperature for any of the samples under study. At low temperature (4.4 K), in the PL spectrum of sample NN3753 ($d_c = 20$ nm) an emission band around 1.3 eV can be observed (see figure 4.23) that can be attributed to the QW/WL.

The decrease of the cap layer thickness from 20 to 3 nm results in a decrease of the

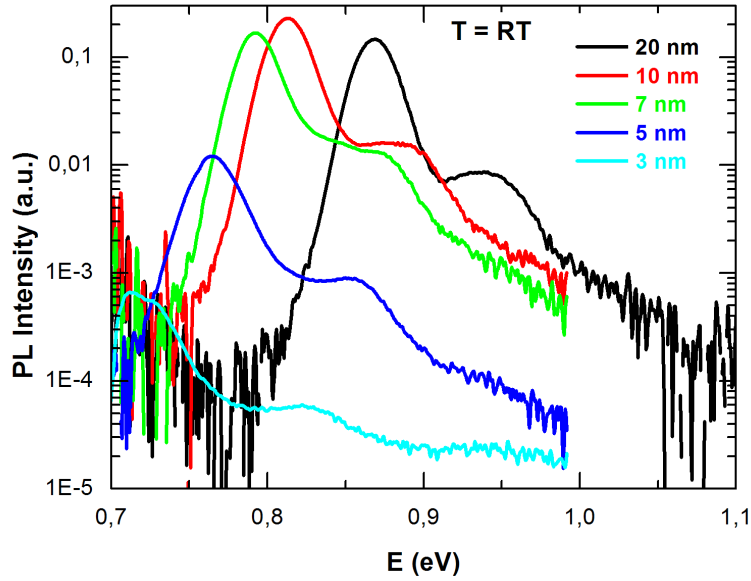


Figure 4.19: PL spectra of thin cap layer samples. The cap layer thickness is identified in the figure. The spectra were obtained with a 457.9 nm line of an Ar^+ laser as excitation source. Samples with $L = 2$ nm (InGaAs QW thickness) and $x = 0.3$ (In content of QW).

QD ground state transition energy from 0.87 to 0.715 eV (figures 4.19 and 4.20). A shoulder at higher energies can be observed in the PL spectra (figure 4.19), probably arising from excited QD states but this was not explored. The decrease of the ground state luminescence (figure 4.19) with decreasing cap layer thickness can be attributed to an additional non-radiative recombination channel: direct tunnelling of the photo-excited carriers from the QD ground state to the surface. As the cap layer thickness decreases, the tunnelling transitions of the electrons from the confined QD levels to the surface states followed by their non-radiative recombination become possible. AFM measurements performed in similar samples revealed a typical lateral base size of the QDs of 40 to 50 nm and height varying from 4 to 6 nm depending on the QDs origin being a surface layer or an etched one [Karpovich et al., 2001].

The temperature dependence of the QD ground state PL emission of the 10 nm cap layer sample (NN3760) was investigated and is shown in figure 4.21. The temperature was varied between 10 and 150 K; above 160 K no luminescence could be seen due to thermal quenching. The difference in the behaviour of the transition energy with temperature between samples TU3904 and NN3760 (cf. figures 4.4 and 4.21) is obviously related to the different energy spacing between the QD and QW/WL ground states which is

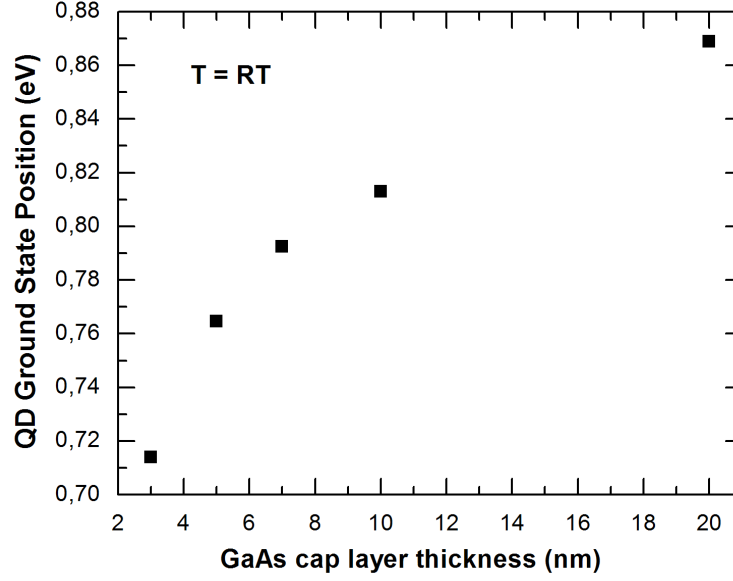


Figure 4.20: QD ground state transition energy at room temperature vs. GaAs cap layer thickness.

much larger in the latter sample.

The influence of the QW thickness and In content in the QW for samples having the same GaAs cap layer thickness is shown in figure 4.22. From these results a shift toward lower energies is observed with the increase of the QW thickness and the increase in In content in the QW. The QW thickness appears to have a different influence depending on the In content, showing a higher band shift for the 30% In content.

The QD ground state of these samples seems to be only excited through the GaAs barrier and the WL as can be seen in the PLE spectra (see figures 4.23, 4.24 and 4.25). Within most of the spectra no fine structure related to excitation via excited states could be observed. However, sample NN3760 ($d_c = 10$ nm) is an exception. The PLE spectrum shows two peaks (denoted by red arrows in figure 4.23 top) spaced by ≈ 70 meV which can arise from QD excited states. The poor signal-to-noise ratio in these experiments hampered the quantitative evaluation of the emissions.

As a function of temperature the PLE (figure 4.24) spectra show almost no differences between 4 and 160 K for the samples with 10 and 20 nm of capping layer thickness. At 200 K, only the 20 nm capping layer sample spectrum is shown since the PL of the 10 nm capping layer sample is already quenched. As stated before, the temperature

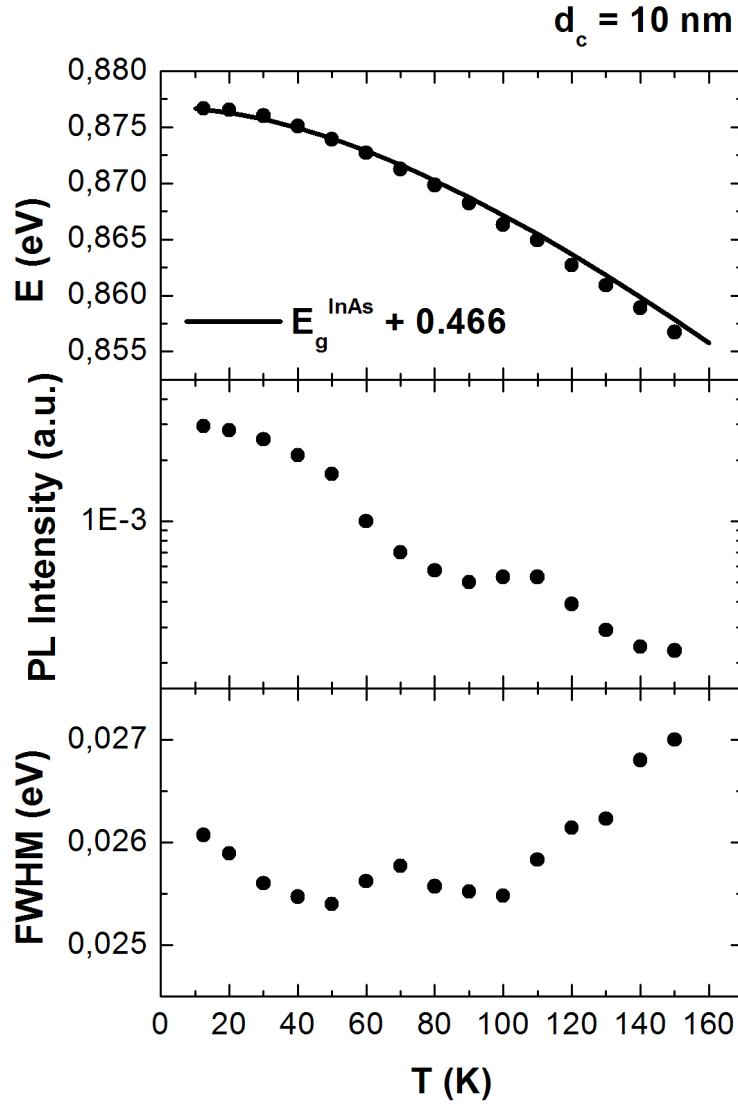


Figure 4.21: Temperature dependence results for sample NN3760 with 10 nm cap layer thickness. Top: QD ground state peak energy position. Middle: integrated PL intensity. Bottom: full width at half maximum (FWHM). For comparison the variation of the InAs bandgap (+0.466 eV), calculated using Varshni's law with the InAs parameters [Varshni, 1967], is shown as a solid line in the top graph of the figure.

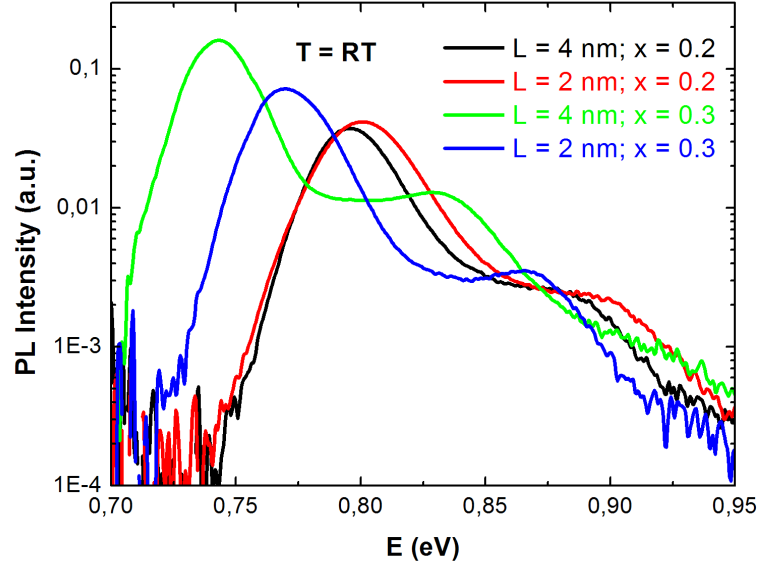


Figure 4.22: PL spectra of thin cap layer samples with different QW thickness and In content in QW, both indicated in the figure. The cap layer thickness is 5 nm. The spectra were obtained at RT with the 457.9 nm line of an Ar^+ laser as excitation source.

increase does not reveal any fine structure arising from excitation via QD states.

Decreasing the In content in the InGaAs QW induces a red shift of the QD ground state (identified in the PL spectrum, figure 4.25 bottom) and QW emission (identified in the PLE spectrum, figure 4.25 top).

The changes in the QD energy spectrum were attributed to the variation of the elastic strain in the pseudomorphic QDs [Karpovich et al., 2004].

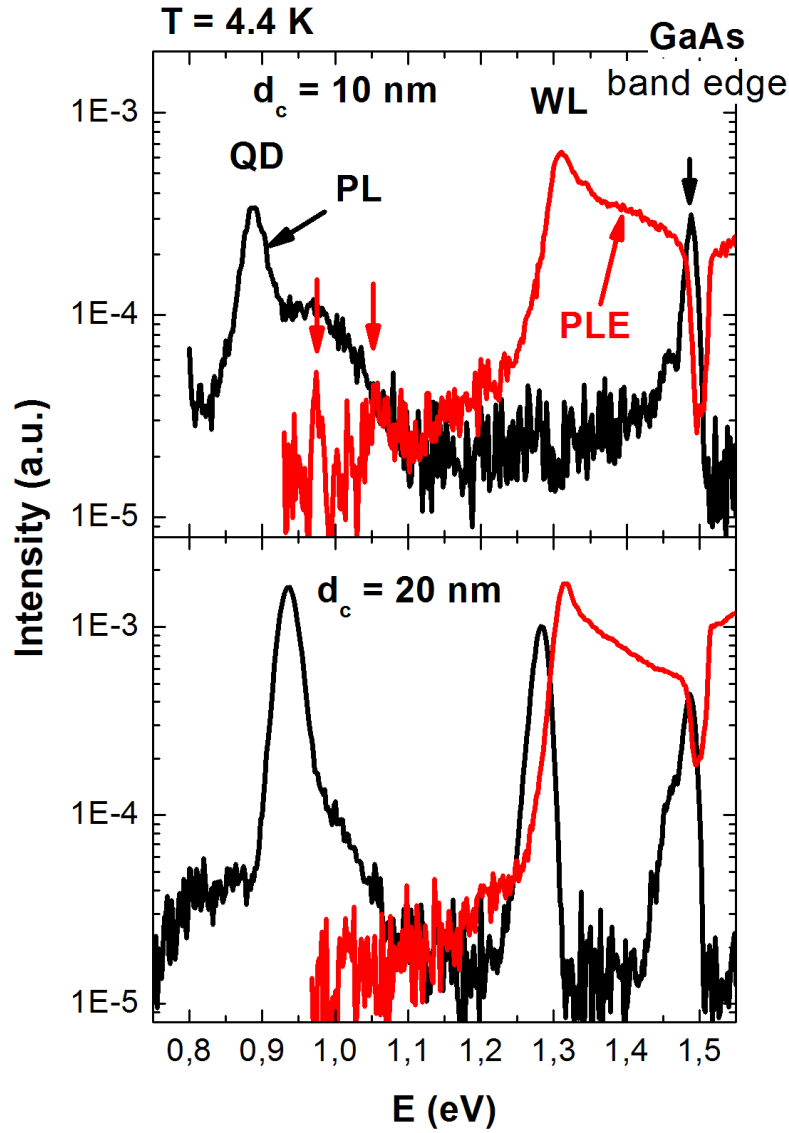


Figure 4.23: PL (black curves) and PLE (red curves) spectra of samples NN3753 ($d_c = 20$ nm, bottom graph) and NN3760 ($d_c = 10$ nm, top graph) taken at 4.4 K. The samples have $L = 2$ nm (InGaAs QW thickness) and $x = 0.3$ (In content in QW). The peaks related to the QDs, WL and GaAs band edge emission are clearly seen.

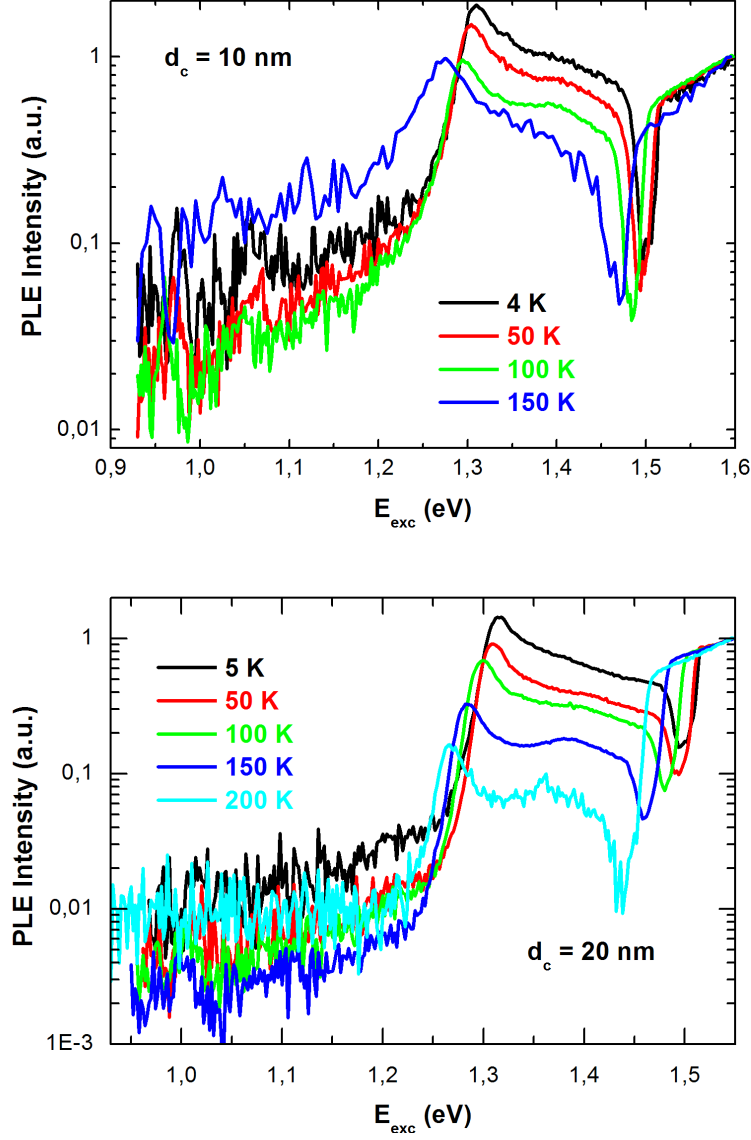


Figure 4.24: PLE spectra of samples with different cap layer thicknesses, indicated in the figure (top: NN3760 – $d_c = 10$ nm and bottom: NN3753 – $d_c = 20$ nm). All samples have $L = 2$ nm (InGaAs QW thickness) and $x = 0.3$ (In content of QW). The spectra are normalized to the intensity above the GaAs bandgap. Note the shift of the GaAs bandgap with temperature.

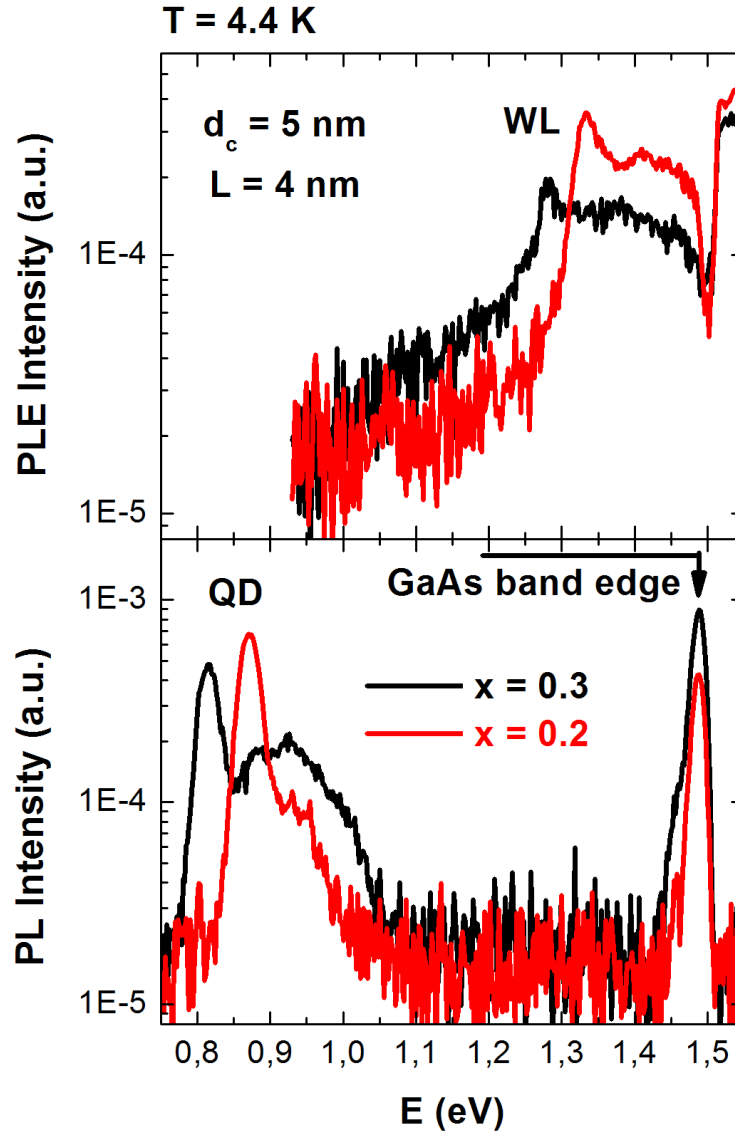


Figure 4.25: PLE (upper panel) and PL (lower panel) spectra taken at 4.4 K on samples with a cap layer thickness of 5 nm and QW thickness $L = 4$ nm. The samples have different In content in the QW, as indicated in the figure.

4.5 Samples subjected to CCl_4 treatment



Figure 4.26: Layer sequence of the samples belonging to the CCl_4 treatment series. Samples are named after table 4.2. The dashed line indicates the stage of the heterostructure growth at which the CCl_4 treatment was applied.

Table 4.2: Sample characteristics.

Sample	d_c (nm)	CCl_4 treat	Type
NN4180	100	yes	n
NN4181	300	no	n
NN4184	30	yes	p
NN4189	100	yes	p
NN4190	30	no	p

InAs/GaAs self-assembled QD heterostructures were grown by atmospheric pressure metal organic vapour phase epitaxy (AP-MOVPE). Two kinds of samples were prepared, with QDs overgrown by an $\text{In}_x\text{Ga}_{1-x}\text{As}$ QW layer at 520 °C ($x = 0.2\text{--}0.3$, thickness of 2–3 nm) and covered with a GaAs capping layer (CL). Samples with no treatment with tetrachloromethane (CCl_4) were grown in standard conditions. Samples with a treatment with tetrachloromethane (CCl_4), which had been shown to decrease the defect concentration in the GaAs matrix [Baidus et al., 2005], were grown slightly different: after the deposition of 2–3 nm of InGaAs (QW) and 10 nm of GaAs onto the QD layer, the growth was interrupted and tetrachloromethane (CCl_4) was introduced into the reactor at 580 °C for 20 s. Finally, the rest of the CL was grown at a temperature somewhat higher than for the other samples. In both cases, the buffer layer was

p-type doped by laser-assisted evaporation of Zn during its growth. This resulted in an acceptor concentration of 10^{17} cm^{-3} in the buffer layer, while the capping layer was not intentionally doped.

The CCl₄ post-growth treatment helps to dissolve the InGaAs clusters as was established by means of AFM [Karpovich et al., 2004]. The morphology of the SAQDs and the roughness of the top surface were explored by AFM. AFM images of uncovered SAQDs, grown under the same conditions, have shown a high size and shape uniformity [Karpovich et al., 2004]. The (uncovered) dot density was measured to be $1.6 \times 10^{10} \text{ cm}^{-2}$.

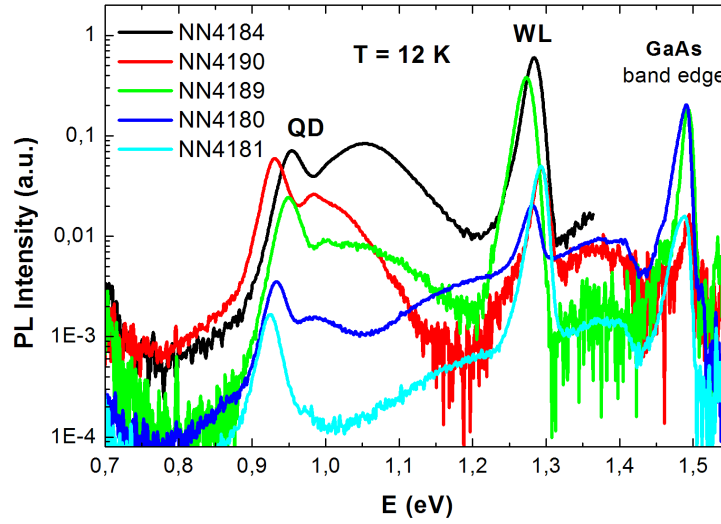


Figure 4.27: PL spectra of samples from the # 41 series taken at 12 K. Sample characteristics and labels are according to table 4.2 and the spectra are all normalized to the incident power.

Figure 4.27 shows PL spectra of samples from the # 41 series taken at 12 K. Figure 4.28 shows PL spectra of samples NN4184 and NN4190 taken at 12 K. These samples are similar differing only in the CCl₄ treatment, as indicated in the figure. The QD PL band shifts to higher energies when submitted to the CCl₄ treatment. The increased temperature used after the CCl₄ treatment explains this shift [Heinrichsdorff et al., 1998a].

The PL intensity temperature dependence is discussed in a dedicated chapter (chapter 7). There more results on these samples and their discussion can be found.

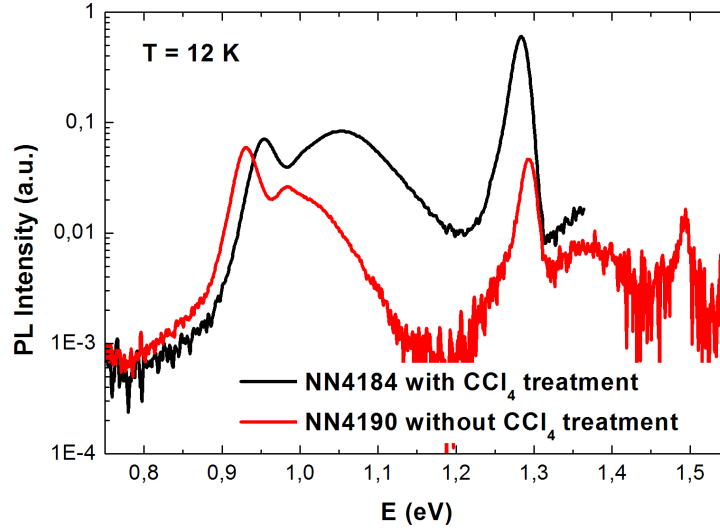


Figure 4.28: PL spectra of two similar samples taken at 12 K, showing the influence of the CCl₄ treatment on the QD PL emission.

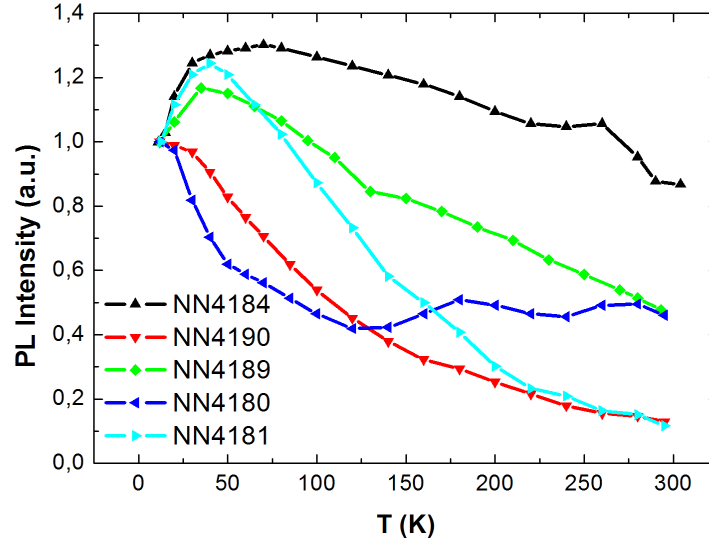


Figure 4.29: Temperature dependence of the QD PL emission from samples of the # 41 series. Sample characteristics and labels are according to table 4.2 .

4.6 Conclusions

The characterization of samples prior to irradiation is presented and discussed in this chapter. Samples with different structures were characterized and the results are presented here. The chapter includes results obtained on laser structure samples and samples with non-uniform wetting layer thickness, as well as samples where the influence of the cap layer thickness and of the treatment with CCl_4 on the quantum dot emission was investigated.

The samples used in this thesis were described and characterized prior to irradiation. The sample structures were presented and the main growth conditions introduced. The influence of parameters such as wetting layer and cap layer thickness, treatment with CCl_4 during the growth and In content on the QD and QW PL emission was investigated. The QD and QW PL emission temperature dependence was also presented for some of the samples.

The study of the laser structures showed that the growth of several layers of QDs allows a significant enhancement of the QD PL intensity. A process of carrier redistribution between dots can explain the behaviour of the QD band emission with temperature.

For the sample with non-uniform wetting layer thickness, the PL spectrum shows a multi-peaked band with the individual maxima centred between 1.238 and 1.362 eV which stem from the WL. Beside the two main peaks at 1.306 and 1.338 eV, three additional peaks can be observed. All these peaks are attributed to a monolayer (ML)-sized splitting of the WL.

The high QD density found in sample TU5411 does not allow the observation of PL bands related to excited states in the low-excitation regime. However, an efficient feeding of carriers from the excited states to the ground state could be found in PLE experiments.

The decrease of the cap layer thickness from 20 to 3 nm results in a decrease of the QD ground state transition energy from 0.87 to 0.715 eV. The decrease of the ground state luminescence intensity with decreasing cap layer thickness can be attributed to an additional non-radiative recombination channel: direct tunnelling of the photo-excited carriers from the QD ground states to the surface. Decreasing the In content in the InGaAs QW induces a red shift of the QD ground state

A blue shift of the QD ground state emission was found when the structure was submitted to the CCl_4 treatment.

Bibliography

- Aigouy, L., Holden, T., Pollak, F., Ledentsov, N., Ustinov, V., Kop'ev, P., and Bimberg, D. (1997). *Applied Physics Letters*, 70:3329.
- Altieri, P., Gurioli, M., Sanguinetti, S., Grilli, E., Guzzi, M., Fiogeri, P., and Franchi, S. (2002). *The European Physical Journal B*, 28:157.
- Baidus, N., Chahboun, A., Gomes, M., Vasilevskiy, M., Demina, P., Uskova, E., and Zvonkov, B. (2005). *Applied Physics Letters*, 87(5):053109.
- Benisty, H., Sotomayor-Torres, C., and Weisbuch, C. (1991). *Physical Review B*, 44(19):10945.
- Bimberg, D., Grundmann, M., and Ledentsov, N. (1999). *Quantum Dot Heterostructures*. John Wiley & Sons, Chichester.
- Brusaferri, L., Sanguinetti, S., Grilli, E., Guzzi, M., Bignazzi, A., Bogani, F., Carraresi, L., Colocci, M., Bosacchi, A., Frigeri, P., and Franchi, S. (1996). *Applied Physics Letters*, 69:3354.
- Chang, K., Yang, S., Chuu, D., Hsiao, R., Chen, J., Wei, L., Wang, J., and Chi, J. (2005). *Journal of Applied Physics*, 97:083511.
- Grundmann, M., Ledentsov, N., Stier, O., Bohrer, J., Bimberg, D., Ustinov, V., Kop'ev, P., and Alferov, Z. (1996). *Physical Review B*, 53(16):R10509.
- Grundmann, M., Stier, O., and Bimberg, D. (1995). *Physical Review B*, 52:11969.
- Heinrichsdorff, F., Grundmann, M., Stier, O., Krost, A., and Bimberg, D. (1998a). *Journal of Crystal Growth*, 195:540.
- Heinrichsdorff, F., Krost, A., Bimberg, D., Kosogov, A., and Werner, P. (1998b). *Applied Surface Science*, 123/124:725 – 728.
- Heinrichsdorff, F., Krost, A., Grundmann, M., Bimberg, D., Bertram, F., Christen, J., Kosogov, A., and Werner, P. (1997a). *Journal of Crystal Growth*, 170:568.
- Heinrichsdorff, F., Krost, A., Grundmann, M., Bimberg, D., Kosogov, A., and Werner, P. (1996). *Applied Physics Letters*, 68:3284.

- Heinrichsdorff, F., Krost, A., Kirstaedter, N., Mao, M.-H., Grundmann, M., Bimberg, D., Kosogov, A., and Werner, P. (1997b). *Japanese Journal of Applied Physics*, 36:4129 – 4133.
- Heinrichsdorff, F., Mao, M.-H., Kirstaedter, N., Krost, A., Bimberg, D., Kosogov, A., and Werner, P. (1997c). *Applied Physics Letters*, 71(1):22 – 24.
- Karpovich, I., Baidus, N., Zvonkov, B., Morozov, S., Filatov, D., and Zdoroveishev, A. (2001). *Nanotechnology*, 12:425.
- Karpovich, I., Zvonkov, B., Baidus, N., Tikhov, S., and Filatov, D. (2004). *Trends in Nanotechnology Research*, chapter Tuning the energy spectrum of the InAs/GaAs Quantum dot structures by varying the thickness and composition of a thin double GaAs/InGaAs cladding layer, page 173. Nova Science, New York.
- Kovsh, A., Zhukov, A., Maleev, N., Mikhlin, S., Ustinov, V., Tsatsul'nikov, A., Maksimov, M., Volovik, B., Bedarev, D., Shernyakov, Y., Kondrat'eva, E., Ledentsov, N., Kop'ev, P., Alferov, Z., and Bimberg, D. (1999). *Semiconductors*, 33:929.
- Le Ru, E., Fack, J., and Murray, R. (2003). *Physical Review B*, 67:245318.
- Lee, E.-K., Tsybeskov, L., and Kamins, T. (2008). *Applied Physics Letters*, 92:033110.
- Lubyshev, D., González-Borrero, P., Marega Jr., E., Petitprez, E., La Scala Jr., N., and Basmaji, P. (1996). *Applied Physics Letters*, 68:205.
- Madelung, O., editor (1987). *Landolt-Börnstein Numerical Data and Functional Relationships in Science and Technology*, volume III, chapter Semiconductors: Intrinsic Properties of Group IV Elements and II-V, II-VI and I-VII Compounds, pages 82 – 94. Springer-Verlag, Berlin.
- Nishi, K., Saito, H., Sugou, S., and Lee, J.-S. (1999). *Applied Physics Letters*, 74:1111.
- Patanè, A., Grassi Alessi, M., Intonti, F., Polimeni, A., Capizzi, M., Martelli, F., Geddo, M., Bosacchi, A., and Franchi, S. (1997). *Physica Status Solidi A*, 164:493.
- Saito, H., Nishi, K., and Sugou, S. (1998). *Applied Physics Letters*, 73:2742.
- Stier, O., Grundmann, M., and Bimberg, D. (1999). *Physical Review B*, 59(8):5688–5701.
- Varshni, Y. (1967). *Physica (Amsterdam)*, 34:1499.

- Volovik, B., Tsatsul'nikov, A., Bedarev, D., Egorov, A., Zhukov, A., Kovsh, A., Ledentsov, N., Maksimov, M., Maleev, N., Musikhin, Y., Suvorova, A., Ustinov, V., Kop'ev, P., Alferov, Z., Bimberg, D., and Werner, P. (1999). *Semiconductors*, 33:901.
- Wasilewski, Z., Fafard, S., and McCaffrey, J. (1999). *Journal of Crystal Growth*, 201:1131.
- Wei, Z., Xu, S., Duan, R., Li, Q., Wang, J., Zeng, Y., and Lin, H. (2005). *Journal of Applied Physics*, 98:084305.
- Xie, Q., Madhukar, A., Cheng, P., and Kobayashi, N. (1995). *Physical Review Letters*, 75:2542.
- Xu, Z., Lu, Z., Yuan, Z., Yang, X., Zheng, B., Xu, J., Ge, W., Wang, Y., Wang, J., and Chang, L. (1998). *Superlattices and Microstructures*, 23:381.

Chapter 5

Radiation hardness

5.1 Introduction

The term “radiation hardness” describes the ability of a structure’s property to withstand the deteriorating action of radiation. The recombination parameters of semiconductors are much more sensitive to radiation defects than, e.g. equilibrium carrier concentration or mobility. Radiation defects with deep levels in the bandgap act as non-radiative recombination centres (lifetime killers) limiting the photoluminescence intensity.

At this point, it is worth noting that there apparently is a general trend for low-dimensional structures to be more defect free than corresponding bulk materials. The increased tolerance of defects is one of the most important promises of the self-assembled QD nanotechnology [Weisbuch and Nagle, 1990]. The basic argument is that more strongly localized carriers exhibit reduced migration to non-radiative centres.

The radiation resistance against damage due to 50 keV manganese ion implantation [Wellmann et al., 1998] and the defects created by 300 eV argon ions [Schoenfeld et al., 1998] was found to be greater for QDs than for QWs. Parallel to the beginning of this work studies of 1.5 MeV proton irradiation of InGaAs/GaAs QD structures were undertaken, and enhanced radiation tolerance of QDs as compared to analogous QWs was reported [Leon et al., 2000]. The effect of irradiation with 8.56 MeV phosphorous ions and 2.4 MeV protons on the properties of QD and QW lasers was investigated [Piva et al., 2000; Ribbat et al., 2001]. A higher stability of the QD devices has been found. The results obtained on QD lasers have recently been confirmed and developed

[Mares et al., 2008].

The tolerance of materials and devices to radiation-induced defects is of crucial importance in atomic energy and space applications. The main goal of this work was to study the radiation-induced defects in quantum-size heterostructures composed of GaAs and InAs. The changes introduced by radiation-induced defects have been evaluated in structures comprising quantum dots and quantum wells subjected to irradiation with electrons and protons.

The irradiation of the samples was performed either with electrons or with protons at three different places: the irradiation by 2 MeV electrons with fluences in the range from 2×10^{15} to 2×10^{17} cm^{-2} was performed at the University of Reading, United Kingdom; the irradiation by 180 keV protons with fluences in the range from 1×10^{11} to 1×10^{12} cm^{-2} was performed at the University of Nizhni Novgorod, Russia; and the irradiation by 2.4 MeV protons with fluences in the range from 1×10^{12} to 1×10^{14} cm^{-2} was performed at the Friedrich Schiller University of Jena, Germany. All irradiation procedures were performed at room temperature using Van de Graaff accelerators.

Figure 2.9 shows a simulation of the penetration of hydrogen atoms (protons with 2.4 MeV) in GaAs. The mean penetration depth (see figure 2.9) is ≈ 43 μm . This means that in the depth where the QDs are located (in the case of the samples examined, the QDs are located between 0.05 and 0.1 μm below the surface) only the defects created by the passage of the protons and not the protons themselves influence the optical properties of the QDs.

Energetic ions can transfer a much larger fraction of their energy to a target atom than it is possible with electrons. Ions are therefore capable of creating much more complicated defects, or defect clusters, in solids, whereas the electrons with energies up to approximately 10 MeV create only isolated point defects. Because the Coulomb interaction between the ionic or electronic projectiles and the atoms in the target lattice emphasizes the low-energy interactions, the average energy transferred is much smaller than the maximum possible one (see figure 2.7 for an example of the maximum and average energy transmitted to a silicon atom as a function of the incident energy for electrons, protons and neutrons).

A further difference between ion and electron irradiation damage arises from the substantial difference in the rates at which they lose energy in penetrating through a solid. For example, 1 MeV electrons would lose about 7 keV of their energy in penetrating to a depth of 10 μm in GaAs [Bichsel, 1972]. As a result of this low energy loss, the

concentration and distribution of defects is expected to be independent of depth. The rate of energy loss for ions in a given material is much greater than for electrons, leading to a much shorter range for ions than for electrons and to a significant variation in the concentration of defects as a function of depth. Also, since the average energy transfer decreases with depth, there may be a variation in the relative concentration of different defects with depth.

5.2 Radiation hardness of QDs and QWs

In order to study the differences in radiation hardness between QDs and QWs, three sets of samples have been studied. The samples prior to irradiation were investigated, and the sample description and results are presented in section 4.1. Before irradiation the samples were cut in eight pieces. An as-grown piece was kept non-irradiated and the other seven pieces were irradiated with fluences ranging from 2×10^{15} to 2×10^{17} e/cm².

After irradiation with 2 MeV electrons, these samples were investigated using optical techniques. Non-resonant and resonant PL (excited above and below the GaAs bandgap, respectively) clearly allowed establishing a higher radiation hardness of QDs.

The PL spectra of as-grown samples taken at the measurement temperature $T = 10$ K upon excitation with an Ar⁺ laser and their evolution versus irradiation fluence are shown in figure 5.1. Significant changes in the energy position upon electron irradiation have not been observed. This gives an indication that the electronic structure of the dots was not affected by irradiation. This behaviour was also observed for proton-irradiated [Leon et al., 2000] and hydrogen-passivated QDs [Le Ru et al., 2000]. With increasing irradiation fluence all samples exhibit a decrease of the PL intensity (figure 5.1). However, whereas in samples 1×QD and 5×QD, QD-related PL peaks could be observed up to fluences of 1×10^{17} and 2×10^{17} cm⁻², respectively, the QW-related PL in sample CQW was quenched already between $\Phi = 2 \times 10^{16}$ and 5×10^{16} cm⁻². This behaviour is essentially the same at 10, 77 and 300 K. For comparison, the PL of bulk n-GaAs with a doping level of 1×10^{17} cm⁻³ is completely suppressed at fluences $\Phi \geq 1 \times 10^{17}$ cm⁻² [Korshunov et al., 1992]. Thus, a much higher tolerance of QDs with respect to MeV electron irradiation as compared to bulk GaAs or QWs was observed. An analogous result was obtained with respect to proton irradiation [Leon et al., 2000]. The PL intensity, I_{PL} , across the QD samples area becomes more inhomogeneous with increasing radiation fluence. Whereas in the as-grown samples

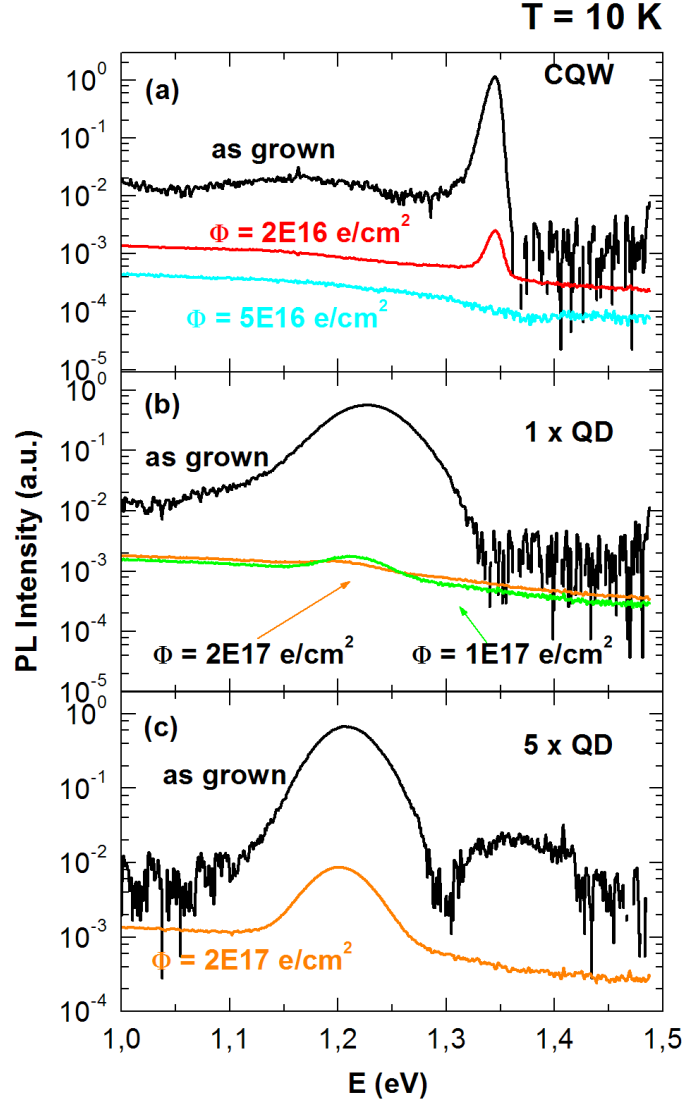


Figure 5.1: FTIR PL spectra of samples 1×QD, CQW and 5×QD measured at 10 K upon excitation with the 457.9 nm line of an Ar⁺ laser. The electron irradiation fluence Φ is indicated. The PL intensity is normalized to the excitation power. The latter did not exceed $\sim 10^{-2}$ W/cm² for the as-grown samples to avoid PL and detector saturation. For irradiated samples with a low PL intensity, the excitation power was increased to maximize the signal.

the lateral fluctuation of I_{PL} remains within a factor of two, in the samples subjected to $\Phi = (1-2) \times 10^{17} \text{ cm}^{-2}$ it can exceed ten. Obviously, this fact cannot be explained only by the lowering of the averaged concentration of photo-generated carriers due to creation of non-radiative recombination centres. It probably implies an interaction between mobile defect components created by irradiation, and QDs.

The quasi-resonant excitation by photons with energies below the barrier bandgap involves only a few relaxation processes which occur only within (and, possibly, between adjacent) QDs. These internal relaxation processes determine the important properties of QDs, which are essential for practical applications. In order to separate the defect related recombination processes in the GaAs barrier from those in the QDs and QWs themselves, the samples were investigated using resonant excitation by means of a Ti⁺-sapphire laser. Selected spectra taken at 12 K are shown in figure 5.2. The excitation energy 1.318 eV lies below the PL peak of the WL centred at 1.35–1.36 eV. As in the case of the above-bandgap excitation, the PL intensity degradation of the QW sample is much stronger than that of the QD samples.

Figure 5.3 shows plots of k/k_0 (see section 5.2.1) vs. electron irradiation fluence for the laser structure samples where different curves represent different temperatures. From these graphs it is clear that the measuring temperature does not influence the radiation hardness results. For the three samples studied, the results are very similar for temperatures between 10 and 300 K.

Figure 5.4 shows plots of k/k_0 vs. electron irradiation fluence for the laser structure samples, where different curves represent different samples. The measurement temperatures are indicated in each graph. Figure 5.4 clearly indicates a difference in the behaviour of the PL intensity with regard to the irradiation fluence. At 10 K (figure 5.4 (top panel)) the QW sample suffers a reduction of the PL intensity just after the second irradiation fluence ($5 \times 10^{15} \text{ cm}^{-2}$).

5.2.1 k/k_0 Representations

In order to obtain the results shown in figures 5.3 and 5.4, the integrated QD PL emission at 10, 77 and 300 K was determined as a function of excitation power for the low excitation regime. Figures 5.5 and 5.6 show an example of the method used to determine k . k is defined as the slope of the linear fit applied to the integrated PL intensity vs. excitation power. k_0 was defined as the value obtained for the as-grown sample. After acquiring the PL spectra for different excitation powers (see figure 5.5),

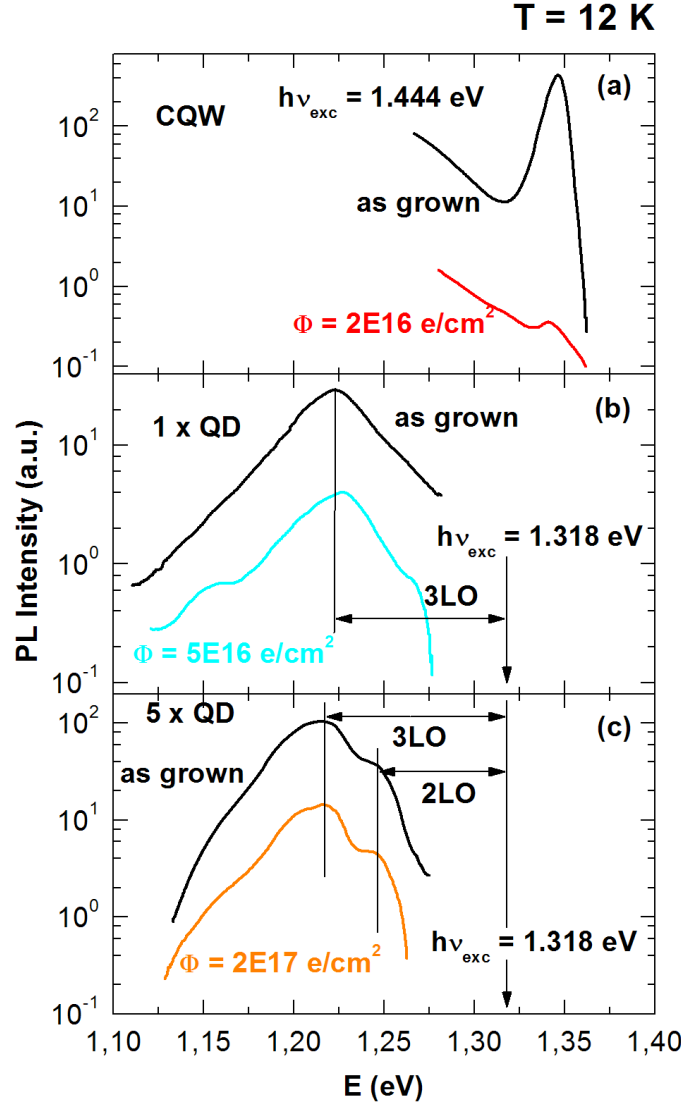


Figure 5.2: PL spectra of samples 1×QD, CQW and 5×QD measured at 12 K upon excitation with a Ti⁺-sapphire laser. The PL intensity is normalized to the excitation power. With the excitation energy $h\nu_{exc}$ being close enough to the QD PL band, resonances within the latter at energies being a multiple of the LO phonon energy can be observed, so that a subset of the QD ensemble defined by the ground state transition energy is probed [Heitz et al., 1997]. The energies of the phonons involved range from 29.6 meV (InAs LO phonon in the WL) to 37.6 meV (GaAs LO phonon in the strained barrier layers adjacent to the QDs) [Heitz et al., 1997]. This explains some variations of the energetic distance of the PL peaks with respect to the exciting laser line seen in (b) and (c). The selectivity is better pronounced in sample 5×QD with five QD planes than in sample 1×QD with only one plane.

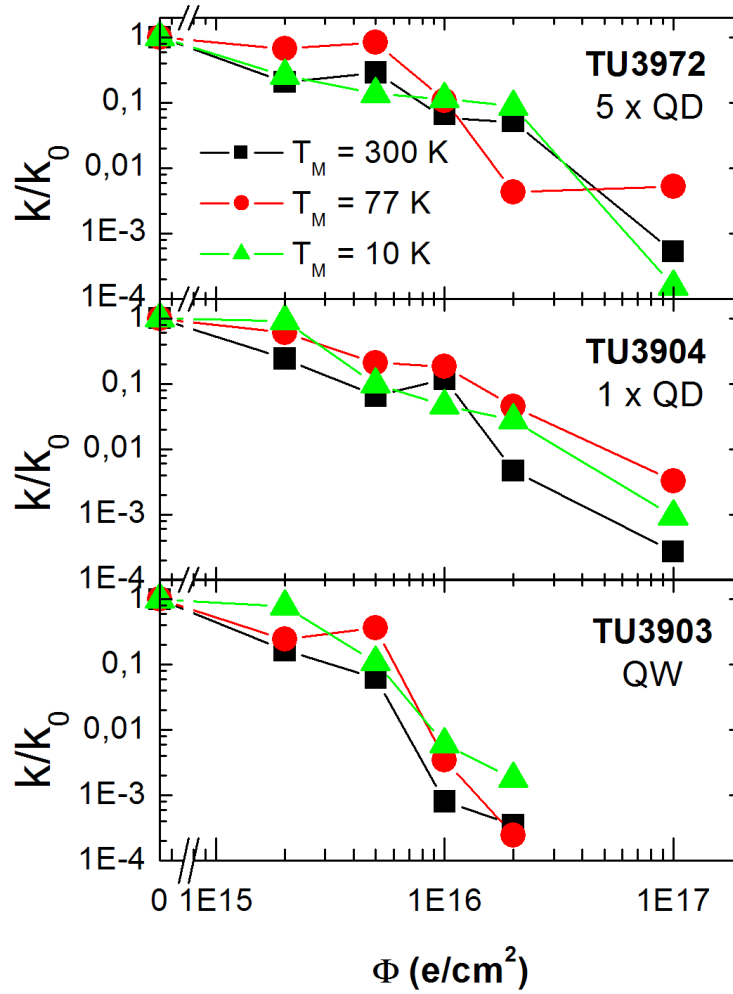


Figure 5.3: Plots of k/k_0 vs. electron irradiation fluence for the laser structure samples. Different curves represent different measurement temperatures as indicated in the figure. Each graph compares results at different temperatures for one and the same sample.

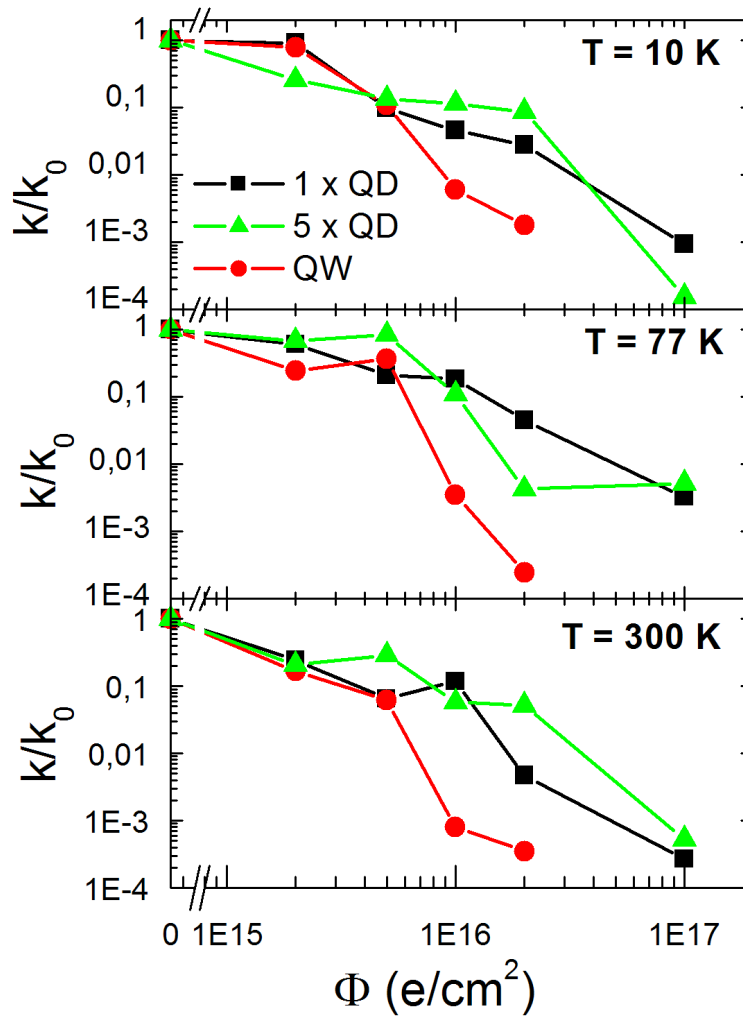


Figure 5.4: Plots of k/k_0 vs. electron irradiation fluence for the laser structure samples. Different curves represent different samples according to the legend. Each graph compares results obtained at one and the same temperature for different samples. The measurement temperatures are indicated in the graphs.

each spectrum was fitted using a Gaussian function. The use of the Gaussian function for the fitting was already discussed in section 4.1. Then, the integrated PL intensity was plotted as a function of the excitation power for each sample (for an example see figure 5.6). The value of k was then obtained by applying a linear fit to the data. The linear character of the PL intensity variation vs. excitation power was a proof of the absence of saturation effects that could distort the fluence dependence of the PL intensity.

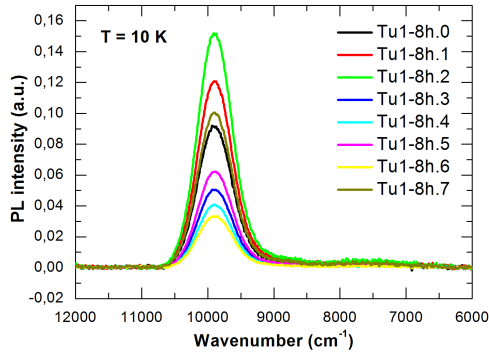


Figure 5.5: PL spectra of the as-grown sample TU3904 ($1 \times \text{QD}$) taken at 10 K for several excitation powers.

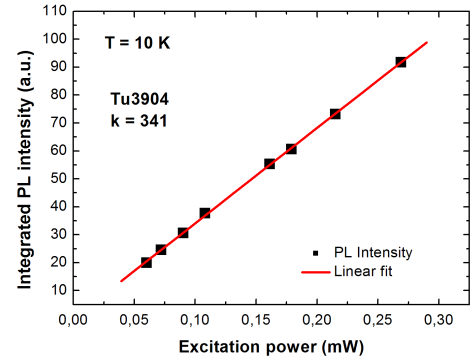


Figure 5.6: Linear fit of the integrated PL intensity vs. excitation power for the as-grown sample TU3904 in order to determine the parameter k .

5.3 Non-uniform WL thickness samples

Samples with non-uniform WL thickness are characterized and described in section 4.2. The irradiation of these samples with 2.4 MeV protons to fluences in the range from 1×10^{13} to $5 \times 10^{13} \text{ cm}^{-2}$ was carried out at RT using a Van de Graaff accelerator.

Figure 5.7 shows PL spectra of samples TU5330, as-grown and irradiated, taken at 10 K. The black vertical lines indicate the WL peak positions of the as-grown sample. The spectra clearly show the influence of radiation-induced defects on the PL spectrum of each sample. All the spectra were normalized to the QD PL emission band in order to emphasize the differences in the WL emission band intensity with the fluence. For the sample with $\Phi = 5 \times 10^{13} \text{ cm}^{-2}$ the ratio between QD and WL PL intensities decreases. In the figure it may look that for this sample, an increase in the WL emissions occurs which is not the case due to a decrease in the absolute intensities. Figure 5.7 clearly corroborates the higher radiation hardness of the QDs as compared to the WL.

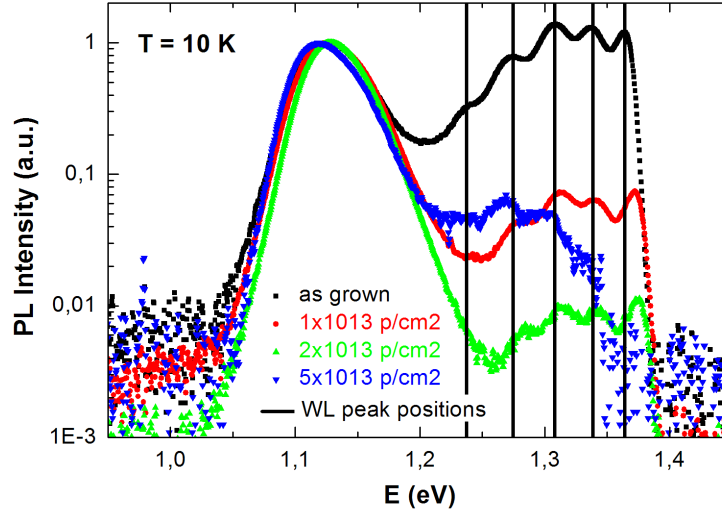


Figure 5.7: PL spectra of sample TU5330 taken at 10 K. Irradiation fluences are indicated in the figure. All spectra are normalized to the QD intensity maximum. The black vertical lines indicate the WL peak positions of the as-grown sample.

5.4 Mechanisms of radiation hardness

Possible processes leading to the quenching of PL intensity upon electron irradiation are:

- Capture and non-radiative recombination of photoexcited carriers at defects in the GaAs barrier. This process should influence the QW and QD luminescence to one and the same extent, provided a linear recombination regime (no saturation) is ensured. In fact, under these conditions the PL intensity of the k -th centre, I_k , is given by the expression:

$$I_k \propto \frac{g\sigma_k N_k}{\sum_i \sigma_i N_i} \quad (5.1)$$

where g is the carrier generation rate, σ_i the capture cross section and N_i the concentration of the i -th center, and the summation is made over all recombination channels. However, upon above-bandgap excitation with the Ar^+ laser we observed very different PL quenching rates for QD and CQW samples which had similar PL intensities prior to irradiation. This means that (i) there is an additional irradiation-induced “QW- and QD-internal” non-radiative recombination

channel that has a much greater cross section in the QW than in the QDs and (ii) that QDs can efficiently capture carriers directly from the barrier.

- If the QDs are fed by carriers also through the WL, the defect-induced non-radiative recombination in the WL should influence the quenching rate of the QD PL. Therefore, an experiment with QD PL excitation below the WL band edge is essential. The QD PL quenching observed upon sub-bandgap excitation confirms very well the existence of an internal defect-related recombination mechanism in the QDs and QW and its greater influence in the latter.
- The internal irradiation-induced non-radiative recombination mentioned above may occur at defects created inside the QW (WL) and QDs as well as at the interfaces QW(WL)/GaAs barrier, QD/QW and QD/GaAs barrier. The delocalization of carriers in the QW (WL) plane perpendicular to the growth direction makes them interact with a much greater number of defects than in QDs [Schoenfeld et al., 1998]. Thus, *a priori* a higher radiation hardness of the QD PL is expected. The role of inhomogeneous strain in defect trapping at interfaces with possible subsequent separation or annihilation has been recently discussed [Bai et al., 2010]. It can not be excluded that the differing strain gradients influence the defect reactions in the QW and QD to a different extent.
- Another mechanism of the “internal” defect-induced PL quenching proposed in [Sercel, 1995] is the carrier tunnelling out of the QW or QDs to defects created in the GaAs barrier. In fact, QDs and QWs have a different sensitivity to defects in the adjacent barrier regions. This is due to a different degree of the wavefunction penetration into the barrier. So, e.g. $\text{In}_{0.13}\text{Ga}_{0.87}\text{As}$ QWs start to “feel” a free surface located at distances less than about 20 nm [Chang et al., 1993]. The PL intensity of InAs/GaAs QDs, however, only degrades for a cap thickness of 9 nm or smaller [Fafard, 2000].

5.5 Conclusions

The current chapter is dedicated to the influence of particle irradiation on optical emissions from quantum dots and quantum wells. A comparison is made regarding the radiation hardness of such quantum heterostructures.

Photoluminescence experiments were performed and the results are presented and dis-

cussed within this chapter. A higher radiation hardness is clearly observed for quantum dots.

The influence of the 2 MeV electron and 2.4 MeV proton irradiation on the PL of InAs/GaAs QW and QD structures was compared. An enhanced radiation hardness of the QDs as compared to QWs was established. The dissimilarity was related to the different influence of defects created inside the QWs and QDs and in the adjacent GaAs barrier on these two quantum-size structures.

Bibliography

Bai, X.-M., Voter, A., Hoagland, R., M., N., and Uberuaga, B. (2010). *Science*, 327:1631.

Bichsel, H. (1972). *American Institute of Physics Handbook*. McGraw Hill, New York, 3rd ed. edition. The electron energy loss was estimated using stopping power data.

Chang, Y.-L., Tan, I.-H., Zhang, Y.-H., Bimberg, D., Merz, J., and Hu, E. (1993). *Journal of Applied Physics*, 74:5144.

Fafard, S. (2000). *Applied Physics Letters*, 76:2707.

Heitz, R., Veith, M., Ledentsov, N., Hoffmann, A., Bimberg, D., Ustinov, M., Kop'ev, P., and Alferov, Z. (1997). *Physical Review B*, 56:10435.

Korshunov, F., Prokhorenko, T., Sobolev, N., and Kudriavtseva, E. (1992). In *Mat Res Soc Symp Proc*, volume 262, page 603.

Le Ru, E., Sivers, P., and Murray, R. (2000). *Applied Physics Letters*, 77:2446.

Leon, R., Swift, G., Magness, B., Taylor, W., Tang, Y., Wang, K., Dowd, P., and Zhang, Y. (2000). *Applied Physics Letters*, 76(15):2074 – 2076.

Mares, J., Harben, J., Thompson, A., Schoenfeld, D., and Schoenfeld, W. (2008). *IEEE Transactions on Nuclear Science*, 55:763.

Piva, P., Goldberg, R., Mitchell, I., Labrie, D., Leon, R., Charbonneau, S., Wasilewski, Z., and Fafard, S. (2000). *Applied Physics Letters*, 77(5):624.

Ribbat, C., Sellin, R., Grundmann, M., Bimberg, D., Sobolev, N., and Carmo, M. (2001). *Electronic Letters*, 37:3.

Schoenfeld, W., Chen, C.-H., Petroff, P., and Hu, E. (1998). *Applied Physics Letters*, 73(20):2935 – 2937.

Sercel, P. (1995). *Physical Review B*, 51(20):14532.

Weisbuch, C. and Nagle, J. (1990). *Science and Engineering of 1D and 0D Semiconductor Systems*. NATO ASI Series B124. Beaumont SP, Plenum, New York.

Wellmann, P., Schoenfeld, W., Garcia, J., and Petroff, P. (1998). *Journal of Electronic Materials*, 27(9):1030.

BIBLIOGRAPHY

Chapter 6

Carrier recombination and intradot relaxation

6.1 Introduction

Possible tunnelling of captured charge carriers off the high-lying QD energy levels to neighbouring defects in the barrier material has been used to explain the absence of the phonon bottleneck in the carrier intradot relaxation [Sercel, 1995]. The most obvious way to check the existence of this mechanism is to vary the defect concentration in a sample and to investigate the resulting changes in the time-resolved photoluminescence (TRPL).

Irradiation creates defects with deep levels that act as non-radiative recombination centres. The existence of stable point defects created by atomic displacements at RT inside the In(Ga)As QDs or ultra-thin QWs has never been proven. Since the primary defects (vacancies and interstitial atoms) are mobile at RT in GaAs (see, e.g. [Pons and Bourgoin, 1985; Stievenard et al., 1986, 1990]) and, certainly, in InAs, it is very likely that they are captured at the interfaces (cf. [Sobolev et al., 1996]). Moreover, the defects increase the free energy of the crystal, so that it is only natural that the QDs expel mobile defect components into the matrix. On the other hand, it has been shown that some leakage of the wave function into the barrier leads to a carrier escape to adjacent defects, thus deteriorating the QW and QD luminescence intensity [Chang et al., 1993; Fafard, 2000].

A PL spectrum measured upon above-bandgap excitation involves QDs with different

ground-state (GS) transition energies, whereas in PLE a subset of the QD ensemble defined by the GS transition energy is probed. PLE is a powerful tool for the characterization of an inhomogeneous QD ensemble giving access to the shape non-uniformity of the islands, carrier relaxation processes and non-radiative recombination [Heitz et al., 1997].

6.2 Carrier dynamics

When talking about carrier dynamics, one must immediately consider the three major phenomena: carrier capture, energy relaxation, and radiative recombination [Bimberg, 1999]. In particular, the capture and energy relaxation are intrinsically connected. TRPL allows the study of carrier dynamics since all three mechanisms appear in the same TRPL experiment: the rise kinetics accounts for the carrier capture and energy relaxation, and the decay kinetics describes the carrier recombination [Bimberg, 1999].

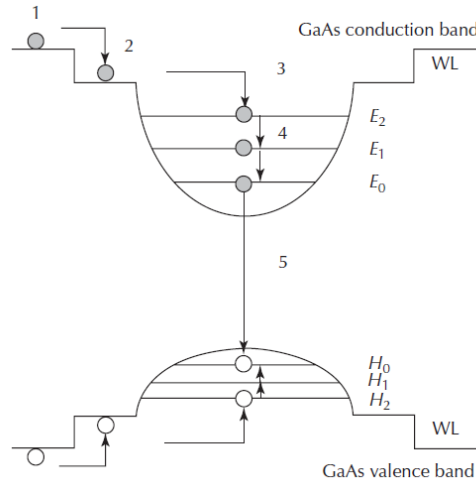


Figure 6.1: Schematic diagram illustrating carrier capture from GaAs barrier into a QD via the wetting layer and carrier relaxation within the QD [Clarke and Murray, 2008].

In order to observe luminescence at the energy of the GS or any other QD level, energy relaxation into that level is necessary (figure 6.1). For most device applications, carriers are either electrically injected or optically excited into the GaAs matrix surrounding the QDs (1). Carriers are then captured, via the wetting layer (WL) (2) or immediately into the QDs (3), and then rapidly relax to the ground state (4). Carrier capture and relaxation occurs on the order of ps. Once carriers reach the ground state E_0 , radiative recombination may take place (5) [Clarke and Murray, 2008]. Possible energy

relaxation mechanisms are the following ones: scattering by acoustic and/or optical phonons, Coulomb scattering and Auger processes, interaction with nearby deep levels and (infrared) optical inter-level transitions [Bimberg, 1999]. It has been shown that the intradot relaxation through acoustical phonons is totally inefficient since the energy mismatch between electron states is far too large [Benisty et al., 1991; Bockelmann and Bastard, 1990]. Auger recombination [Efros et al., 1995] and Coulomb scattering of free carriers [Bockelmann and Egeler, 1992; Pan, 1994] require a high density of hole states or large free-carrier concentrations in order to obtain sufficient high relaxation rates. At low excitation densities, both conditions are not given for small self-organized QDs [Grundmann et al., 1995], making phonons the most likely candidates to dissipate the energy in carrier relaxation. A strong coupling regime between electrons and LO-phonons was observed [Heitz et al., 1997] with the formation of everlasting polarons in InAs/GaAs QDs [Hameau et al., 1999].

The structural properties, in particular the shape and composition profile, of self-organized In(Ga)As/GaAs QDs strongly affect the exciton dynamics [Heitz et al., 2002]. The low symmetry and inhomogeneous strain provide in general for distinctively different electron and hole wave functions [Stier et al., 1999] and enable one to engineer the electron-hole overlap, i.e. the oscillator strength, as well as the local charge density, i.e. the polar exciton-LO-phonon coupling strength. The coupling strength, being proportional to the local charge density [Schmitt-Rink et al., 1987], depends on the difference of the electron and hole wave functions [Stier et al., 1999] and, thus on the particular structural properties of the QDs: the effect is pronounced for a pyramidal but strongly quenched for a flat shape. Thus, the ground state lifetime is expected to be shorter (large overlap integral) in the flat InGaAs QDs, whereas the stronger polar exciton-LO-phonon interaction (large local charge density) should provide for faster relaxation in the pyramidal InAs QDs. Depending on the QD shape, relaxation- or recombination-limited exciton dynamics should be observed.

6.3 Equipment and measurement conditions

The cw PL and PLE experiments were performed in a continuous-flow He cryostat at temperatures between 7 and 300 K. A tungsten lamp dispersed by a 0.27 m double-grating monochromator served as a low density, tunable light source. The emission was spectrally dispersed by a 0.3 m double-grating monochromator and detected with a cooled Ge diode using lock-in techniques. The measurement techniques and equipment

have been thoroughly discussed in sections 3.2.1 and 3.2.2.

The TRPL measurements were carried out at 2 K using a single photon counting technique. The exciting Ti^+ -sapphire laser system including an OPO, with spectrally narrow (<1 meV) pulses, operated at 790 nm (1.569 eV) for above-bandgap excitation or at 858 nm (1.445 eV) for resonant excitation with a pulse width of 2 ps. The emitted light was dispersed by a subtractive double-grating monochromator and detected with a multi-channel plate photomultiplier with an S1-cathode in the photon-counting mode. The time resolution of the detecting system was about 20 ps. The averaged excitation density within the pulse was 250 W/cm^2 . The experimental facilities and techniques are described in details in section 3.2.3.

6.4 Proton-irradiated samples

6.4.1 Samples

The samples used in the proton-irradiation studies (TU5411 and TU5330) were grown by metal-organic chemical vapour deposition and have the following structure: a GaAs buffer layer was grown on top of a GaAs substrate, the active layer together with GaAs cladding layers were placed between two AlGaAs barriers, with a GaAs capping layer on top of the whole structure. Sample TU5411 has an active layer composed by a QD layer, with a dot density of $(3-5) \times 10^{10} \text{ cm}^{-2}$, overgrown by a 2 nm $\text{In}_{0.25}\text{Ga}_{0.75}\text{As}$ QW. Sample TU5330 has a dot density of $\approx 10^9 \text{ cm}^{-2}$ in an active layer composed by a single QD layer. The irradiation by 2.4 MeV protons with fluences in the range from 1×10^{12} to $1 \times 10^{14} \text{ cm}^{-2}$ was performed at room temperature using a Van de Graaff accelerator. A more detailed characterization of these samples can be found in sections 4.2 and 4.3.

6.4.2 Results

Figure 4.15 shows the FTIR PL spectrum of the as-grown sample TU5411 taken at 10 K upon excitation with the 488 nm line of an Ar^+ laser. The energies assigned in the graph represent the detection and excitation energies used in TRPL measurements (see figure 6.2) on the same sample. For sample TU5411, kinetic curves were fitted using exponential functions including a rise and a decay time. Table 6.1 shows the rise and decay times obtained from the fitting as a function of irradiation fluence. For

Table 6.1: TRPL rise and decay times of proton-irradiated samples TU5411.

fluence p/cm ²	E_{exc} = 1.57 eV		E_{exc} = 1.14 eV		E_{exc} = 1.12 eV	
	τ_r , ps	τ_d , ps	τ_r , ps	τ_d , ps	τ_r , ps	τ_d , ps
as-grown	397	896	648	700	660	662
1×10^{13}	353	848	666	667	489	832
2×10^{13}	340	880	443	873	467	893
5×10^{13}	196	958	273	939	250	969
1×10^{14}	104	928	150	944	131	955

all samples the detection was performed at the ground state energy, $E = 1.04$ eV (see figure 4.15), and the excitation was performed at the following energies (see figures 4.15 and 6.3b): $E = 1.12$ eV (a sublevel of the first excited state), $E = 1.14$ eV (another sublevel of the first excited state) and $E = 1.57$ eV (above-GaAs bandgap excitation).

According to the results shown in figure 6.2 and table 6.1, the increasing defect concentration with increasing dose does not affect the lifetime of the ground state exciton, always showing a single-exponential decay. This is true both for above-GaAs bandgap and resonant excitation into the first excited state of QDs. A more or less constant decay time around 900 ps is observed. The data suggest tunnelling from the QD ground state to defect states to be negligible at the proton irradiation dose used here. The rise time is clearly affected by irradiation showing a decrease from around 400 ps to 100 ps as irradiation fluence increases. The long rise time in the reference sample is attributed to slowed down intradot relaxation [Heitz et al., 2001]. Carrier migration in the GaAs barrier is negligible for the rise time due to the AlGaAs diffusion barriers reducing the average diffusion length to below ~ 50 nm. If one looks at the change of the rise time as a function of the excitation energy, an increase can be seen going from above-bandgap excitation to the resonant excitation into excited states. This increase is more pronounced for the as-grown sample and vanishes for the heavier irradiated one. The reduced PL rise time and the decreased PL efficiency in the irradiated samples suggest tunnelling from excited QD states to defects. The increasing tunnelling probability with increasing defect concentration quenches the excitation efficiency and the rise time (see figures 6.2 and 6.3).

Figure 6.3a shows PL spectra of sample TU5411 for various proton irradiation fluences (as indicated in the figure) taken at 7 K. The PL intensity behaviour is the same as that observed for the electron-irradiated samples in chapter 5, viz., the intensity

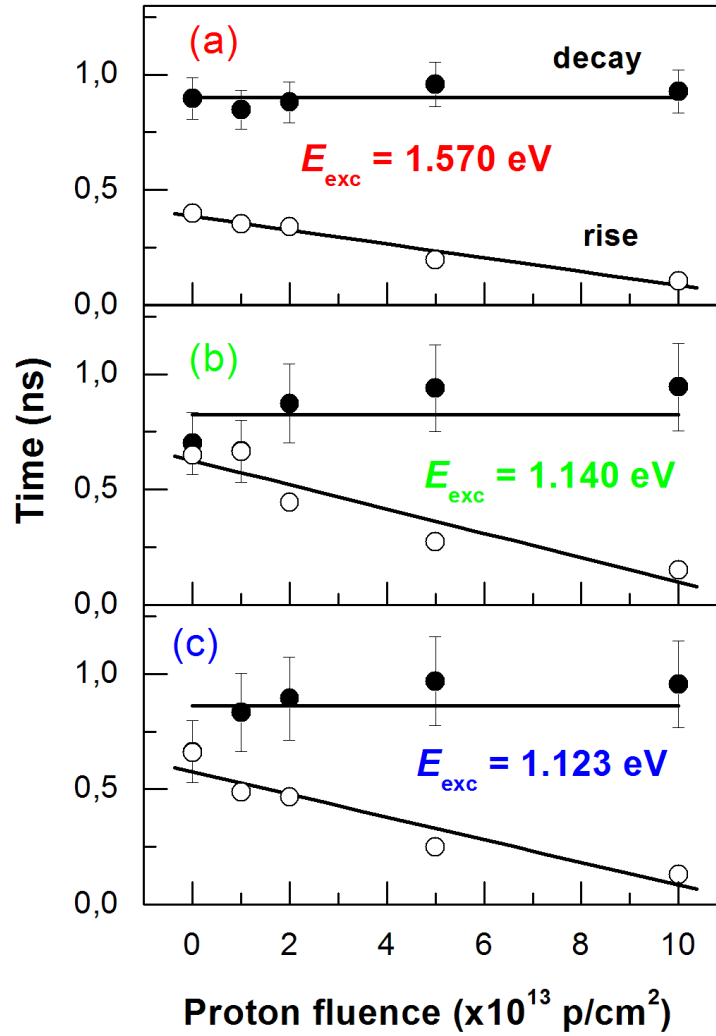


Figure 6.2: Rise (open circles) and decay (solid circles) times obtained from TRPL measurements of sample TU5411. The detection energy was at the ground state transition. The excitation energies are indicated in the graphs.

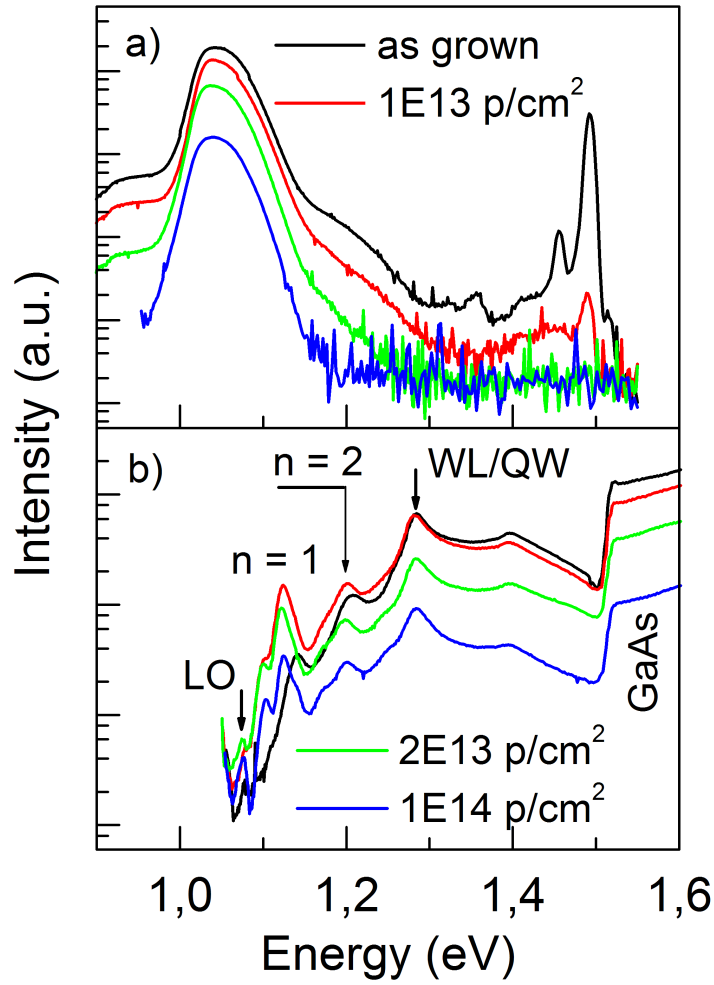


Figure 6.3: (a) PL and (b) PLE spectra of sample TU5411 for various proton irradiation fluences, measured at 7 K. The PLE spectra were recorded at the QD PL intensity maximum.

decreases as the irradiation fluence increases. Figure 6.3b represents PLE spectra of the same sample for various proton irradiation fluences. LO-phonon resonances, excited states and WL energy positions are indicated. The detection occurred at the QD PL maximum, $E_{det} = 1.04$ eV, the ground state energy position. An increase upon irradiation of the PLE intensity at energies corresponding to the low-lying QD excited states can be observed (figure 6.3b).

Figure 6.4a shows PLE spectra plotted vs. the excess excitation energy $\Delta E = E_{exc} - E_{det}$ of the as-grown sample TU5330 taken at different temperatures (as indicated in the graph). The detection was performed at the QD PL maximum. The spectra are normalized to the detection energy and to the second excited state intensity. Figure 6.4b presents PLE spectra of sample TU5330 for various proton fluences, recorded at the QD PL maximum at 7 K. The spectra are normalized to the intensity above the GaAs bandgap.

As referenced before, an increase of the PLE intensity at energies corresponding to the low-lying QD excited states is observed upon irradiation. The effect is particularly well seen in figure 6.4b, where the PLE intensities for all fluences have been normalized to that of the as-grown sample at energies exceeding the GaAs bandgap, and in the contour plots (figure 6.5). Qualitatively similar effects are observed when the temperature is increased (figure 6.4a) or a reverse bias is applied to a diode structure with the dots located in the space charged region [Guffarth et al., 2003, 2002]. The radiation defects shift the Fermi level towards the middle of the bandgap, thus emptying the low-lying QD states from spectator carriers allowing the resonant absorption to occur. The results (see figure 6.4a) unambiguously demonstrate a slow relaxation between the first excited and the ground state, which accelerates with increasing temperature supporting the notion of inelastic phonon scattering. In the case of a temperature increase, the important effect is the growth of the phonon density which accelerates the relaxation and helps overcome the phonon bottleneck [Heitz et al., 2001].

Figure 6.5 shows contour plots of the QD PL intensity as a function of the detection energy and the excess excitation energy $\Delta E = E_{exc} - E_{det}$ taken at 7 K for the as-grown and proton-irradiated samples TU5330 (the irradiation fluences are indicated in the graphs). The white lines denote PLE resonances from the excited states and LO-phonons. For the as-grown and the two lowest irradiation fluences samples, the first excited state resonance is not observed, appearing only for the highest irradiation fluence shown (see also figure 6.4).

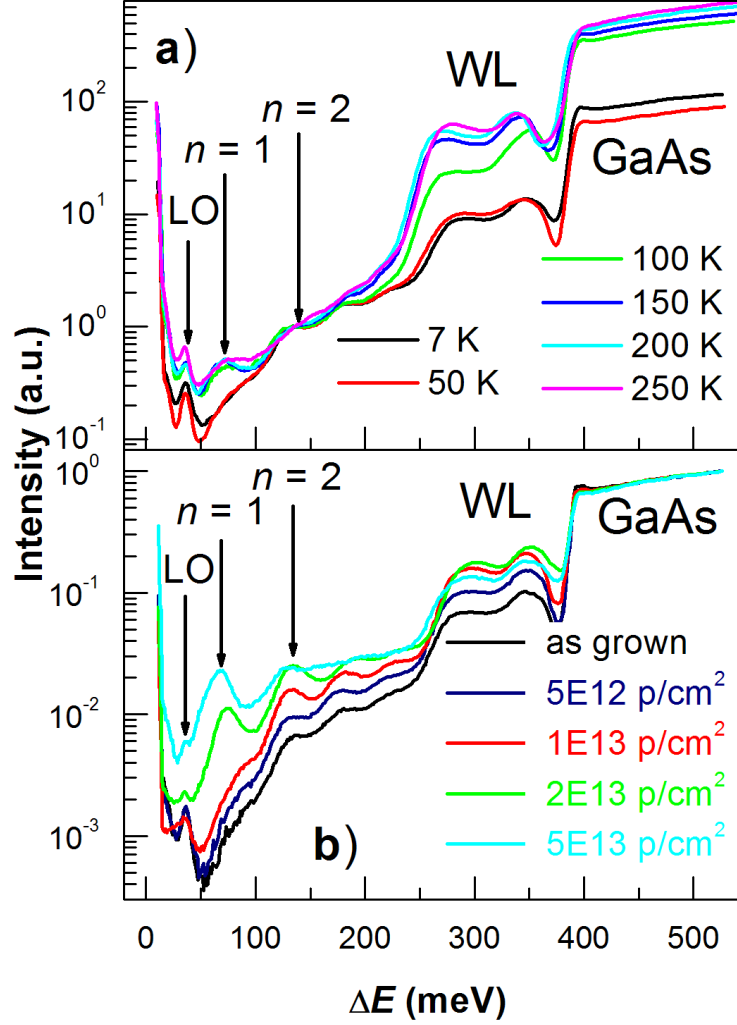


Figure 6.4: PLE spectra of sample TU5330. a) PLE spectra vs. the excess excitation energy $\Delta E = E_{exc} - E_{det}$ of the as-grown sample TU5330 taken at different temperatures. Detection was performed at the QD PL maximum. The spectra are normalized to the detection energy and to the second excited state intensity. b) PLE spectra of sample TU5330 for various proton fluences, recorded at the QD PL maximum at 7 K. The spectra are normalized to the intensity above the GaAs bandgap.

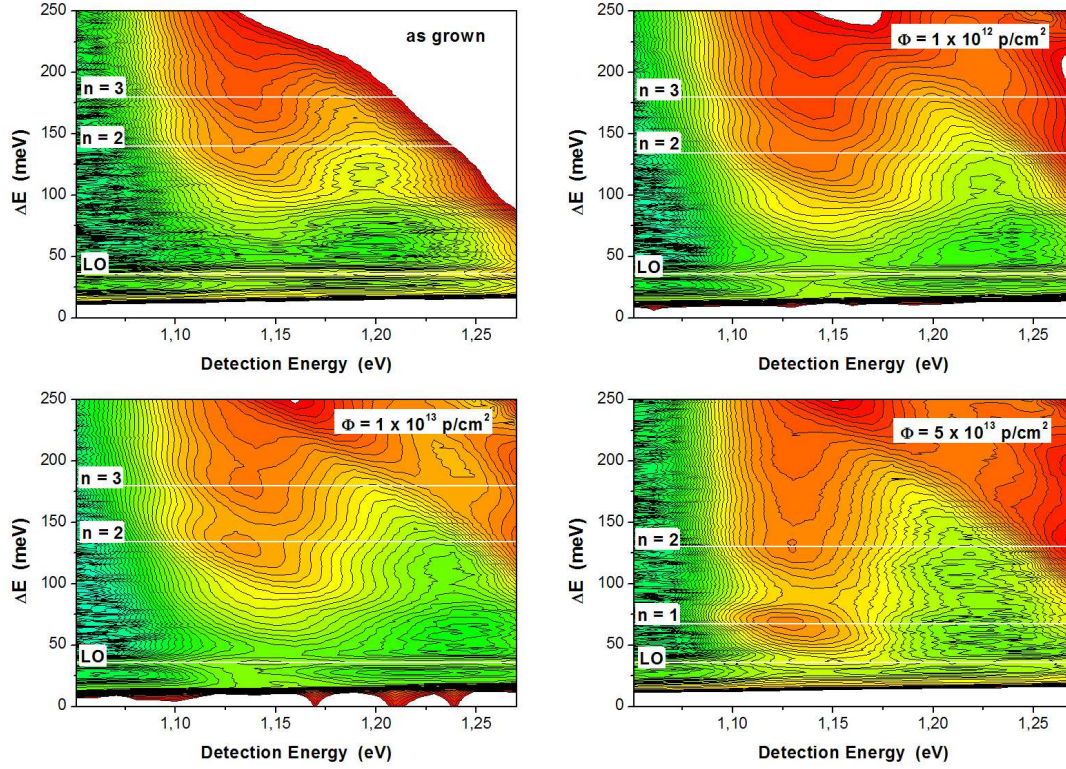


Figure 6.5: Contour plots of the QD PL intensity measured at 7 K as a function of the detection energy and the excess excitation energy $\Delta E = E_{exc} - E_{det}$ for the as-grown and proton-irradiated samples TU5330. The white lines denote PLE resonances from the excited states and LO-phonons. The irradiation fluences are indicated in the graphs.

Usually the defects reduce the lifetime of non-equilibrium carriers and, consequently, their diffusion length, thus limiting the carrier supply to the radiative recombination centres and quenching the PL intensity. However, because of the presence of the closely spaced AlGaAs barriers, the carrier capture by the QDs in the samples under study is not diffusion-limited. That is why no difference in the quenching factor of the PL intensity is observed at a given irradiation fluence for the above-bandgap and below-bandgap excitation for all energies above the $n = 2$ QD excited state (figure 6.3). Thus, the loss of carriers occurs mainly in the dots themselves. A probable reason of this effect is a tunnelling out of the dots to adjacent radiation-induced non-radiative recombination centres, as described in section 5.4.

6.4.3 Discussion

No influence of the irradiation on the PL decay kinetics from the ground state is observed (figure 6.2) since the decay times are essentially the same for the as-grown and irradiated samples, as well as for the above- and below-bandgap excitation. This situation is only possible if no defects are created inside the QDs, showing no alternative path for the carriers to recombine but through radiative recombination. These results agree with those shown in section 6.5 where a second decay component appearing after irradiation was ascribed to defects created close to or inside the QDs.

However, the rise time shortens by a factor of four for the maximum fluence used (1×10^{14} p/cm²), both for the excitation into the barrier (figure 6.2a) and into the sublevels of the first excited state at 1.140 eV and 1.123 eV (figure 6.2b and c). This means that the rise time shortening upon above-bandgap excitation is caused by a carrier (exciton) loss in the QDs and not by any reduction of the diffusion length in the barrier or the WL. The effect can be explained by the tunnel escape of the carriers to adjacent defects. The ground state, having a more localized wave function than the excited ones, remains essentially “undamaged”.

The rise time increases as the excitation energy decreases (see table 6.1), mainly for the as-grown sample. For the heavier irradiated sample this behaviour vanishes. The resonant excitation does not account for any kind of diffusion or transport, so this increase is related only to relaxation mechanisms, showing a more efficient path from the barrier than from the excited states to the ground state. If the relaxation process would depend on a cascade of events through the different intermediate states, a higher rise time for the barrier excitation would be expected. Since this is not the case, the existence of a bottleneck at the first excited state becomes a possible explanation. Moreover, the results for the irradiated samples show that an alternative path owing to the irradiation exists to overcome this bottleneck.

6.5 Electron-irradiated samples

6.5.1 Samples

Two types of samples were grown using MOCVD under identical conditions and subjected simultaneously to electron irradiation. The samples differed only with respect to the active region. In the sample 1×QD (TU3904), the active region consisted of

one layer layer of self-assembled InGaAs/GaAs QDs with density $5 \times 10^{10} \text{ cm}^{-2}$ on a thin wetting layer (WL). Sample CQW (TU3903) contained two coupled InAs/GaAs quantum wells separated by 1 nm. The active layer together with the GaAs cladding layers was placed between two $\text{Al}_{0.3}\text{Ga}_{0.7}\text{As}$ barriers (see figure 4.1). The samples are thoroughly characterized in section 4.1. The irradiation by 2 MeV electrons with fluences in the range of 2×10^{15} to $2 \times 10^{17} \text{ cm}^{-2}$ was performed at room temperature using a Van de Graaff accelerator.

6.5.2 Results

The results of the TRPL measurements on $1 \times \text{QD}$ and CQW samples, upon above-bandgap excitation ($E_{exc} = 1.569 \text{ eV}$), are shown in figure 6.6. The rise (τ_r) and decay (τ_d) times, obtained from the exponential fitting, are given in table 6.2. The transients prior to irradiation can be fitted with single values of τ_r and τ_d .

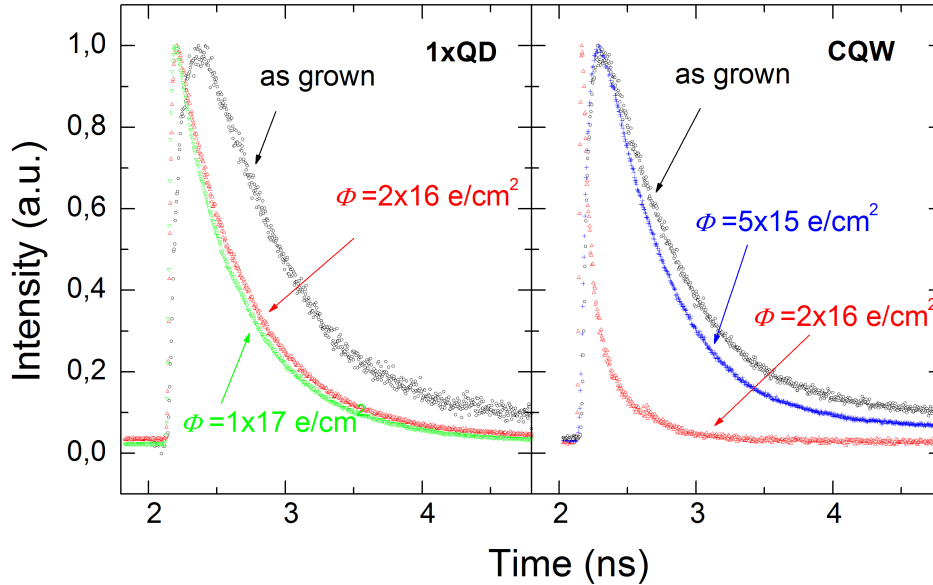


Figure 6.6: PL transients taken at 2 K of the as-grown and electron-irradiated CQW and $1 \times \text{QD}$ samples. Above-bandgap excitation occurred at an energy of 1.569 eV. Detection energy was 1.230 eV for $1 \times \text{QD}$ and 1.340 eV for CQW, respectively.

Table 6.2: TRPL rise (τ_r) and decay (τ_d) times of electron-irradiated samples CQW and 1×QD upon above-bandgap excitation.

Sample, fluence (e/cm ²)	τ_r , ps	τ_{d1} , ps	τ_{d2} , ps
CQW, as-grown	65	485	-
CQW, 5×10^{15}	50	440	-
CQW, 2×10^{16}	<20	220	-
1×QD, as-grown	105	565	-
1×QD, 2×10^{16}	<20	615	295
1×QD, 1×10^{17}	<20	600	230

In the irradiated CQW samples the PL kinetics can still be fitted with single values of τ_r and τ_d , but a reduction in both τ_r and τ_d can be observed as the irradiation fluence increases. τ_r decreases to values below the spectrometer resolution for the minimum fluence studied.

For the irradiated 1×QD samples the PL decay can only be described by at least two different τ_d values (see table 6.2). As in the case of the CQW sample, τ_r decreases to values lower than the spectrometer resolution for the minimum fluences studied.

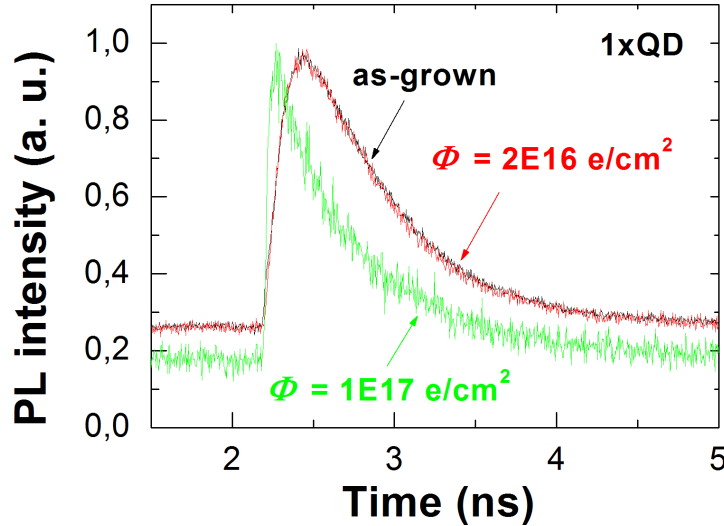


Figure 6.7: PL transients taken at 2 K of as-grown and electron-irradiated 1×QD samples. Below-bandgap excitation at an energy of 1.445 eV. Detection energy is 1.230 eV.

Figure 6.7 shows the transients of sample 1×QD upon resonant excitation below the GaAs bandgap, at 1.445 eV. The irradiation fluence is indicated in the figure. Table 6.3

Table 6.3: TRPL rise and decay times of electron-irradiated samples 1×QD upon resonant excitation.

Sample, fluence (e/cm ²)	τ_r , ps	τ_{d1} , ps	τ_{d2} , ps
1×QD, as-grown	117	522	-
1×QD, 2×10^{16}	113	489	-
1×QD, 1×10^{17}	<20	619	126

summarizes the time constants obtained from the exponential fitting to the data. As for the above-bandgap excitation, the curve for the as-grown sample was fitted using single rise and decay times and that for the heaviest irradiated sample with one rise time and two decay times. Comparing figure 6.6 with figure 6.7 and table 6.2 with table 6.3, a striking difference can be noted. Sample 1×QD with $\Phi = 2 \times 10^{16} \text{ cm}^{-2}$ presents a completely distinct behaviour when excited above and below the GaAs bandgap. While upon above-bandgap excitation, this sample exhibited a behaviour similar to that of the heavily irradiated sample, for below-bandgap excitation it behaves like the as-grown sample. This behaviour can be explained regarding the relation between the wave function penetration depth into the barrier and the distance between the dots and defects.

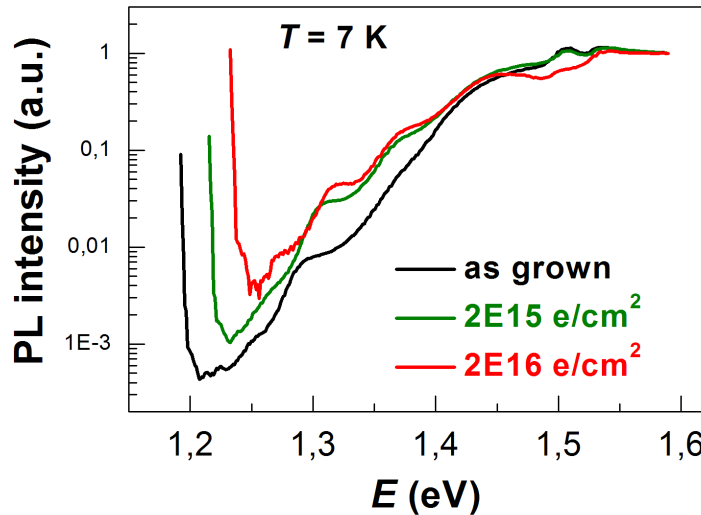
**Figure 6.8:** PLE spectra of sample 1×QD for various electron irradiation fluences, measured at 7 K. The PLE spectra were recorded at the QD PL maximum. The spectra are normalized to the intensity above the GaAs bandgap.

Figure 6.8 shows PLE spectra of sample 1×QD measured at 7 K for various electron irradiation fluences. The PLE spectra were recorded at the QD PL maximum and are normalized to the intensity at energies above the GaAs bandgap. A striking feature of the PLE spectra is the increase upon irradiation of the PLE intensity at energies corresponding to the low-lying QD excited states. The same behaviour was observed for the proton-irradiated sample (figure 6.4). These results indicate a higher probability of the non-radiative recombination of the photoexcited carriers in the barrier than inside the dots. The resonances observed in the PLE spectra (see figure 6.8) are attributed to excited state transitions, although the high QD density of these samples never allowed the observation of bands belonging to excited states in the nonresonantly excited PL spectra (see section 4.1). No resonance corresponding to the WL position could be observed for these samples, either.

6.5.3 Discussion

There is a clear impact of the introduced radiation defects on the rise and decay times in both CQW and QD samples (figures 6.6 and 6.7). The fast rise time is an indication of an effective carrier relaxation to the QD ground state. The decay time is reduced due to the increase of non-radiative recombination caused by the radiation-induced defects. The reduced PL rise time and the decreased PL efficiency in the irradiated samples suggest a tunnelling of the carriers/excitons from the dots to adjacent defects.

The electron irradiation with high fluences induces a second process with a shorter PL decay time. The higher τ_d characterizes the as-grown sample. Since not all QDs in a sample are disturbed by defects, the slow decay component is still observed even after irradiation. The shorter PL decay time that does not change with irradiation fluence is ascribed to the existence of QDs perturbed by defects inside or immediately adjacent to them.

The heaviest electron irradiation used in this work induces such a high concentration of defects that there is no way for the QDs to escape an interaction with the latter since the distance between QDs and radiation-induced defects decreases with increasing fluence. For the medium irradiation dose, the radiation hardness depends on the excitation wavelength due to the wave function penetration depth of the energy levels involved.

Qualitatively the same behaviour has been observed upon resonant (below bandgap) excitation for the CQW sample. However, a poor signal-to-noise ratio and a strong substrate PL impeded a reliable quantitative evaluation.

6.6 Conclusions

The influence of high-energy electron and proton irradiation on the time-resolved photoluminescence and the photoluminescence excitation spectra of quantum dot and quantum well InGaAs/GaAs structures is reported and discussed. A clear interaction of the created defects and the quantum dot structures is observed for both types of particle irradiation. The results suggest expulsion of the defects by the dots, resulting in a high radiation hardness of the latter.

For proton-irradiated samples, only the rise kinetics is affected by irradiation. The decay kinetics remains unchanged probably due to the fact that QDs have the ability, due to strain fields, of expelling mobile defects. The PL rise time gets shorter with increasing irradiation fluence owing to carrier escape out of the excited QD states to adjacent radiation-induced defects.

For the electron-irradiated samples, the decay kinetics of the as-grown QWs and QDs can be described by a single time constant. The irradiated QWs still exhibit the single exponential decay, however, with a shorter time constant, whereas the second, faster component appears in the PL decay of QDs along with the component present prior to irradiation. Thus, an interaction of confined carriers with radiation-induced defects located inside or very close to the QDs was observed. An influence of the energy level wave function penetration depth was found on the carrier dynamics in irradiated samples.

For the sample configuration used (two AlGaAs diffusion barriers surrounding the QD plane), the main part of the carrier loss due to introduced radiation damage occurs in the dots, even for the excitation of the GaAs barrier.

The decreasing PL intensity upon irradiation reflects the decreasing excitation efficiency originating from 1) tunnelling out of excited QD states due to slow relaxation at low temperatures and 2) efficient non-radiative recombination in the barrier, when carriers escape thermally from the QDs at elevated temperatures.

The difference in the radiation fluences between the electron and proton irradiations is of three orders of magnitude for the heaviest irradiated samples. According to figure 2.7 the difference in average energy transmitted to an atom at MeV energies is less than an order of magnitude for electrons when compared to protons. So, the heavily electron-irradiated samples probably have, at least, two orders of magnitude more defects than the proton-irradiated ones. This is why a second decay time is not observed for the

proton-irradiated samples.

Bibliography

- Benisty, H., Sotomayor-Torres, C., and Weisbuch, C. (1991). *Physical Review B*, 44(19):10945.
- Bimberg, D. (1999). *Semiconductors*, 33(9):951.
- Bockelmann, U. and Bastard, G. (1990). *Physical Review B*, 42:8947.
- Bockelmann, U. and Egeler, T. (1992). *Physical Review B*, 46:15574.
- Chang, Y.-L., Tan, I.-H., Zhang, Y.-H., Bimberg, D., Merz, J., and Hu, E. (1993). *Journal of Applied Physics*, 74:5144.
- Clarke, E. and Murray, R. (2008). *Handbook of Self Assembled Semiconductor Nanostructures for Novel Devices in Photonics and Electronics*, chapter 3 – Optical Properties of In(Ga)As/GaAs Quantum Dots for Optoelectronic Devices, page 84. Elsevier, The Netherlands.
- Efros, A., Kharchenko, V., and Rosen, M. (1995). *Solid State Communications*, 93:281.
- Fafard, S. (2000). *Applied Physics Letters*, 76:2707.
- Grundmann, M., Stier, O., and Bimberg, D. (1995). *Physical Review B*, 52:11969.
- Guffarth, F., Heitz, R., Geller, M., Kapteyn, C., Born, H., Hoffmann, A., Bimberg, D., Sobolev, N., and Carmo, M. (2003). *Applied Physics Letters*, 82:1941.
- Guffarth, F., Heitz, R., Kapteyn, C., Heinrichsdorff, F., and Bimberg, D. (2002). *Physica E*, 13:278.
- Hameau, S., Guldner, Y., Verzelen, O., Ferreira, R., Bastard, G., Zeman, J., Lemaître, A., and Gérard, J. (1999). *Physical Review Letters*, 83:4152.
- Heitz, R., Born, H., Guffarth, F., Stier, O., Schliwa, A., Hoffmann, A., and Bimberg, D. (2001). *Physical Review B*, 64:241305(R).
- Heitz, R., Born, H., Guffarth, F., Stier, O., Schliwa, A., Hoffmann, A., and Bimberg, D. (2002). *Physica Status Solidi A*, 190:499–504.

- Heitz, R., Veith, M., Ledentsov, N., Hoffmann, A., Bimberg, D., Ustinov, M., Kop'ev, P., and Alferov, Z. (1997). *Physical Review B*, 56:10435.
- Pan, J. (1994). *Physical Review B*, 49:2536.
- Pons, D. and Bourgoin, J. (1985). *Journal of Physics C: Solid State Physics*, 18:3839.
- Schmitt-Rink, S., Miller, D., and Chemla, D. (1987). *Physical Review B*, 35:8113.
- Sercel, P. (1995). *Physical Review B*, 51(20):14532.
- Sobolev, N., Korshunov, F., Sauer, R., Thonke, K., König, U., and Presting, H. (1996). *Journal of Crystal Growth*, 167:502.
- Stier, O., Grundmann, M., and Bimberg, D. (1999). *Physical Review B*, 59(8):5688–5701.
- Stievenard, D., Boddaert, X., and Bourgoin, J. (1986). *Physical Review B*, 34:4048.
- Stievenard, D., Boddaert, X., Bourgoin, J., and von Bardeleben, H. (1990). *Physical Review B*, 41:5271.

Chapter 7

Influence of defects on the temperature dependence of the PL intensity

7.1 Introduction

In most QD applications, the devices are expected to work at room temperature or even higher. However, the luminescence is often quenched at temperatures significantly below 300 K, cf. chapter 4. Understanding the temperature dependence of the QD emission and the factors influencing it is important to building efficient and temperature insensitive lasers. There is a consensus in the literature that the quenching phenomenon observed in PL spectra is linked to thermal escape of carriers from the QDs to the surrounding matrix, followed by non-radiative recombination [Bacher et al., 1991; Brusafferri et al., 1996; Le Ru et al., 2003; Polimeni et al., 1999; Wasilewski et al., 1999]. Point defects and defect clusters in the matrix are suspected to be responsible for the trapping of escaped carriers. In fact, they serve as local non-radiative recombination centres for electron-hole pairs, and thus reduce the luminescence efficiency of optical devices. Understanding the real role of defects in the performance of QD devices and the optimization of the defect concentration for achieving the best QD emission stability is a challenging task. It has been shown in ref. [Baidus et al., 2005] that elimination of defects via growth treatment using tetrachloromethane eliminates the quenching of PL at room temperature.

In this chapter, we have extended the investigations to the case of samples containing a

well-defined amount of intentionally introduced defects. These defects were introduced in a controlled way by proton or electron irradiation.

7.2 Equipment and measurement conditions

Photoluminescence (PL) was measured at sample temperatures ranging from 10 to 300 K in a closed-cycle or continuous-flow cryostat. The PL was excited either with an Ar^+ laser (488 nm) or a He-Ne laser (632.8 nm). The spectra were recorded with a Fourier-transform infrared (FTIR) spectrometer with a cooled Ge detector or with a Spex grating monochromator and an InGaAs photodiode using standard lock-in technique. The experimental facilities and techniques are described in detail in section 3.2.1.

7.3 Experimental results

7.3.1 Laser structures

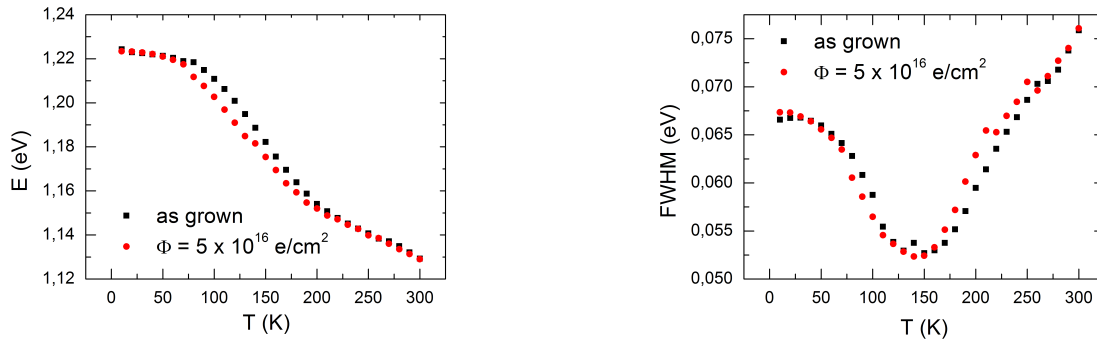


Figure 7.1: Temperature dependence, from 10 to 300 K, of the PL of samples 1×QD (TU3904), as-grown and irradiated. The irradiation fluence is indicated in the graph. Left: QD PL energy peak position; right: full width at half maximum (FWHM) of the QD PL band.

Three types of samples were grown using MOCVD under identical conditions according to the layer sequence shown in figure 4.1. The samples differ only with respect to the active region: sample 1×QD (TU3904) is composed of one layer of self-assembled InAs/GaAs QDs on a thin WL; sample CQW (TU3903) is formed by two coupled InAs QWs separated by 1 nm GaAs; sample 5×QD (TU3972) contains five QD layers

separated by 20 nm GaAs. The active layer together with the GaAs cladding layers are placed between two $\text{Al}_{0.3}\text{Ga}_{0.7}\text{As}$ barriers. The structure was grown on top of a GaAs substrate and a GaAs buffer layer. The samples are thoroughly characterized in section 4.1. The irradiation by 2 MeV electrons with fluences in the range from 2×10^{15} to $2 \times 10^{17} \text{ cm}^{-2}$ was performed at room temperature using a Van de Graaff accelerator.

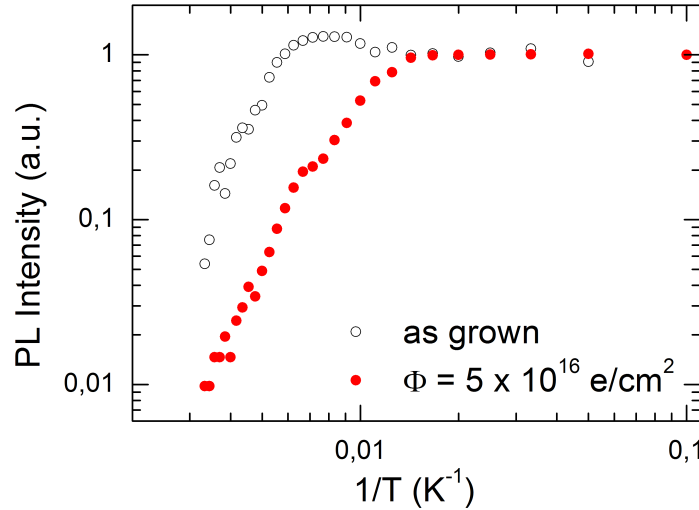


Figure 7.2: Arrhenius plots of the PL intensity for samples $1 \times \text{QD}$ (TU3904), as-grown and irradiated. The irradiation fluence is indicated on the graph.

Figure 7.1 shows the QD PL band energy position (on the left) and full width at half maximum (FWHM) (on the right) as a function of temperature for the as-grown and for an irradiated sample $1 \times \text{QD}$ (TU3904). The irradiation fluence was equal to $5 \times 10^{16} \text{ e/cm}^2$. No significant differences have been observed for the temperature dependences of the PL band energy position or the FWHM with increased concentration of radiation defects (see figure 7.1). For a more detailed description of these dependences see section 4.1. Figure 7.2 shows an Arrhenius plot of the PL intensity for the same samples. Here the difference between the as-grown and irradiated samples is clearly visible.

7.3.2 Samples subjected to CCl_4 treatment

InAs/GaAs QD heterostructures were grown by Atmospheric Pressure Metal-Organic Vapor Phase Epitaxy (AP-MOVPE). Two kinds of samples were prepared. Samples

NN4190 with no treatment with tetrachloromethane (CCl_4) were grown in standard conditions. Samples NN4184 were subjected, during the growth process, to a treatment with tetrachloromethane (CCl_4), which had been shown to decrease the defect concentration in the GaAs matrix [Karpovich et al., 2004]. For a more detailed description of these samples see section 4.5. The irradiation by 180 keV protons with fluences ranging from 10^{11} to 10^{12} p/cm² was performed at RT using a Van de Graaff accelerator.

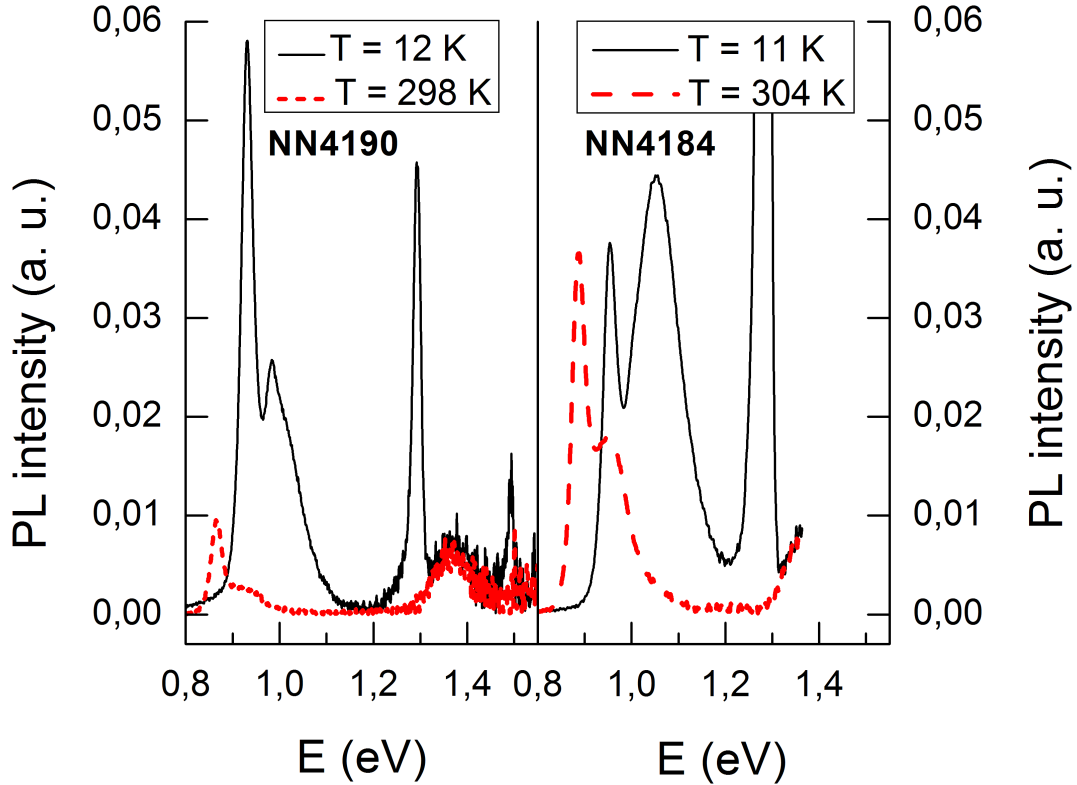


Figure 7.3: PL spectra of two QD/QW heterostructures, left: NN4190, and right: NN4184, taken at two different temperatures. The units are indicated in the plots and are the same for all spectra. The most important bands are identified.

Samples NN4190 and NN4184 were found to show different trends in the variation of the PL intensity with measurement temperature. The temperature dependence of the QD PL intensity from sample NN4190 exhibits a typical quenching at room temperature. Figure 7.3 (left) shows two PL spectra of sample NN4190 recorded at 12 and 298 K. At 12 K, emission bands from the QDs, QW and GaAs can be observed. The rather low inhomogeneous broadening observed for the QD emission band is an indication of a narrow QD size dispersion. Beyond the main peak of the QD emission, the spectrum shows a band slightly above 1 eV that originates from excited states in the dots. In

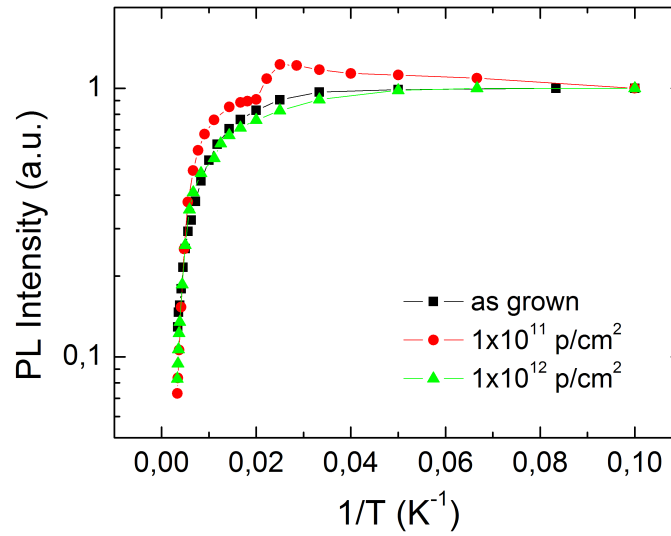


Figure 7.4: Temperature dependence of the integrated PL intensity (normalized to the low-temperature value) for an as-grown and two proton-irradiated NN4190 samples. Irradiation fluences are indicated on the plot.

contrast, the decrease in the PL intensity of the QD ground state emission peak is very small for sample NN4184 (see figure 7.3, right), less than by a factor of 2 up to room temperature.

Figure 7.4 shows the experimental temperature dependence of the integrated PL intensity for an as-grown and two proton-irradiated NN4190 samples. The intensity values are all normalized to the low-temperature value. The irradiation fluences are indicated on the plot.

Figure 7.5 shows the experimental temperature dependence of the integrated PL intensity for an as-grown and two proton-irradiated NN4184 samples. The intensity values are all normalized to the low-temperature value. The irradiation fluences are indicated on the plot. The blue asterisks show the temperature dependence of the PL emission band of the as-grown QW sample.

Figure 7.6 shows the experimental temperature dependence of the integrated QD PL intensity for two values of the beam power of the Ar^+ laser as indicated in the plot. The estimated power densities on the sample are 1 mW/cm^2 and 1 W/cm^2 , respectively. The results are for the as-grown sample NN4190.

These results being experimental were included here but are discussed in section 7.6

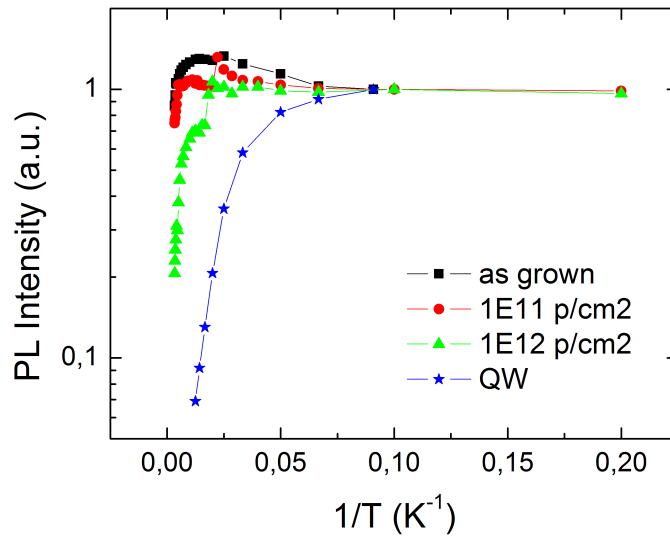


Figure 7.5: Temperature dependence of the integrated PL intensity (normalized to the low-temperature value) for an as-grown and two proton-irradiated NN4184 samples. The irradiation fluences are indicated on the plot. The blue asterisks show the temperature dependence of the PL emission band of the as-grown QW sample.

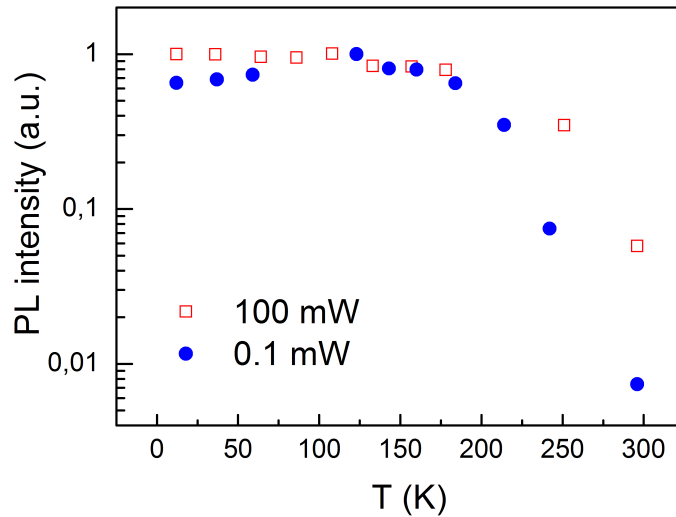


Figure 7.6: Experimental temperature dependence of the integrated QD PL intensity for two values of the beam power of the Ar^+ laser as indicated in the plot (estimated power density on the sample $1 \text{ mW}/\text{cm}^2$ and $1 \text{ W}/\text{cm}^2$, respectively). Results are for the as-grown sample NN4190.

together with the calculated results presented in section 7.5.

7.4 Model

The work has been performed in collaboration with Prof. Dr. M. Vasilevskiy from the University of Minho. The main objective of the described model is to explain the trends of the ground-state emission from the QDs.

Assumptions:

- Just one electron energy level, $E_c - E_{QD}^e$;
- Just one hole energy level, $E_v - E_{QD}^h$;
- The dots are embedded in a QW with
 - The lowest possible electron energy, $E_c - E_{QW}^e$;
 - The lowest possible hole energy, $E_v - E_{QW}^h$;
- The GaAs matrix is considered intentionally doped with acceptors, and their ionization energy is E_a .
- The modulation doping affects the confinement potential profiles, but it is assumed that this effect is taken into account in the characteristic energies introduced above.

The model band structure is presented in figure 7.7. Besides the energies referenced above, it includes also the Fermi level (E_F), the quasi-Fermi level (F) and the trap energy level (E_t). As usual, the bandgap energy is denoted by E_g , the conduction band minimum by E_c and the valence band maximum by E_v .

7.4.1 Heterostructure in equilibrium

At equilibrium, the majority carriers (holes in this case) are distributed between acceptors, GaAs barriers, QDs and QW. In order to achieve an analytical solution, an effective homogeneous system representing the heterostructure is considered. This implies the use of an effective three-dimensional (3D) concentration of QDs,

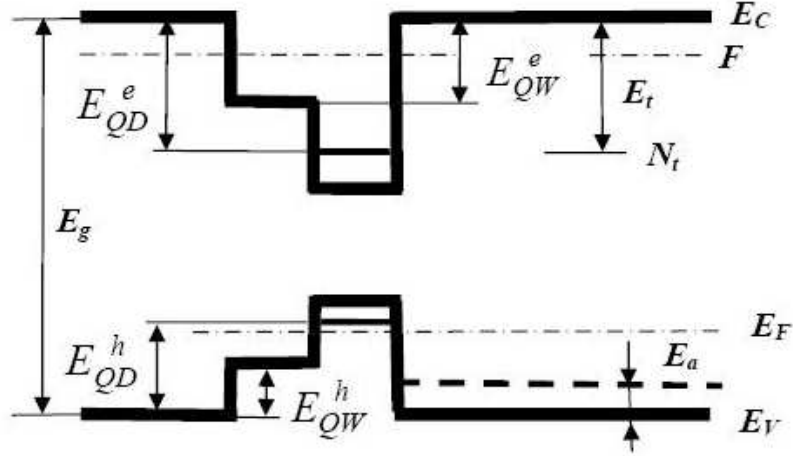


Figure 7.7: Model band structure of the GaAs/GaInAs(QW)/InAs(QD) heterostructure.

$$N_{QD}^{(3D)} = \frac{N_{QD}^{(2D)}}{w} \quad (7.1)$$

where $N_{QD}^{(2D)}$ is the usual two-dimensional dot density referred in sample description, and w is a characteristic thickness of the system at equilibrium. w is of the order of the overall thickness of the buffer and capping layers, or the Debye length, whichever is smaller. Similarly to the QDs, an effective 3D density of states for the QW is introduced,

$$N_{QW}^{(3D)} = \frac{1}{w} \frac{m^* kT}{\pi \hbar^2}, \quad (7.2)$$

where m^* is the effective mass of the carriers. Then, hole concentrations in the QDs, QW, and GaAs matrix are given by the standard statistical relations:

$$p_{QD} = N_{QD}^{(3D)} \left[\beta_{QD}^h \exp \left(\frac{E_F + E_g - E_{QD}^h}{kT} \right) + 1 \right]^{-1}, \quad (7.3)$$

$$p_{QW} = N_{QW}^{(3D)} \ln \left[\exp \left(\frac{-E_F - E_g + E_{QW}^h}{kT} \right) + 1 \right], \quad (7.4)$$

$$p_M = N_V F_{1/2} \left(-\frac{E_F + E_g}{kT} \right), \quad (7.5)$$

where E_F is the Fermi level position with respect to the bottom of the GaAs conduction band (E_c), E_g is the bandgap energy of GaAs, β_{QD}^h is the degeneracy factor of the QD hole level, and

$$N_V = \frac{[(m_{hh} + m_{lh}) kT]^{\frac{3}{2}}}{\sqrt{2}\pi^{\frac{3}{2}}\hbar^3}, \quad (7.6)$$

where m_{hh} and m_{lh} are heavy and light hole effective masses, respectively, $N_{QW}^{(3D)}$ is given by equation 7.2 with $m^* = m_{hh}$, and $F_{1/2}$ is the Fermi integral. The Fermi level position can be found from the neutrality equation

$$p_{QD} + p_{QW} + p_M = N_a \left[1 + \frac{1}{4} \exp \left(\frac{E_a - E_F - E_g}{kT} \right) \right]^{-1}, \quad (7.7)$$

where N_a is the acceptor concentration and, the degeneracy factor of the acceptor level has been taken equal to 4.

7.4.2 Heterostructure under illumination

The assumption of relatively low excitation intensity shall be considered now in order to be possible to consider the majority carriers at equilibrium and described by the same (true) Fermi level.

It is also assumed that the photogenerated minority carriers (electrons) are distributed between QDs, QW, and GaAs matrix, and that the equilibrium between the QD, QW, and matrix states is established much faster than the recombination occurs, meaning it is reached within the photocarrier's lifetime. This last assumption is hardly realistic at low temperatures. The experimental results (see figures 7.4 and 7.5) show that the major differences occur for $T \geq 100$ K. This is the temperature range where the model is expected to work. In this temperature region, phonon-assisted processes of carrier capture, relaxation, and excitation into higher energy states can be fast enough to justify the (pseudo-) equilibrium assumption. It is also assumed, for simplicity, that the electrons in the matrix are non-degenerate.

It is now possible to introduce a quasi-Fermi level (F) for the electrons and express the (3D) electron concentrations in different states using relations analogous to equations (7.3), (7.4) and (7.5) (and in close analogy to what has been done in ref. [Baidus et al., 2005]),

$$n_M = N_C \exp\left(\frac{F}{kT}\right), \quad (7.8)$$

$$n_{QW} = \tilde{N}_{QW}^{(3D)} \ln \left[1 + \exp\left(\frac{F + E_{QW}^e}{kT}\right) \right], \quad (7.9)$$

$$n_{QD} = \tilde{N}_{QD}^{(3D)} \left[1 + \frac{1}{\beta_{QD}^e} \exp\left(-\frac{F + E_{QD}^e}{kT}\right) \right]^{-1}, \quad (7.10)$$

where, $\tilde{N}_{QW}^{(3D)}$ is given by equation (7.2) with $m^* = m_e$, and

$$N_C = \frac{(m_e kT)^{\frac{3}{2}}}{\sqrt{2\pi} \hbar^3}. \quad (7.11)$$

Depending on the type of excitation (above or below bandgap), the photocarriers can be generated:

1. Everywhere in the heterostructure, if $\hbar\omega > E_g$,
2. Only in the QW/QD layer, if $E_g' < \hbar\omega \leq E_g$, where $E_g' = E_g - E_{QW}^e - E_{QW}^h$.

In case (1), as shown in Appendix A, the photocarriers are generated in a near-surface layer of a typical thickness equal to $(\alpha^{-1} + L_n)$, where α is the absorption coefficient of GaAs and L_n the electron diffusion length. In case (2), the effective thickness of the system should be taken equal to the QW width (d). Taken this into account,

$$\tilde{N}_{QW}^{(3D)} = \frac{m_e kT}{\pi \hbar^2} \frac{1}{\tilde{w}}, \quad \tilde{w} = \begin{cases} d, & E_g' < \hbar\omega \leq E_g \\ (\alpha^{-1} + L_n), & \hbar\omega > E_g \end{cases}, \quad (7.12)$$

and

$$\tilde{N}_{QD}^{(3D)} = \frac{N_{QD}^{(2D)}}{\tilde{w}}, \quad \tilde{w} = \begin{cases} d, & E_g' < \hbar\omega \leq E_g \\ (\alpha^{-1} + L_n), & \hbar\omega > E_g \end{cases}. \quad (7.13)$$

7.4.3 Recombination channels

The following recombination channels for the photocarriers are considered:

1. radiative recombination in the QDs,
2. radiative recombination in the QW,
3. nonradiative recombination in the GaAs matrix.

As shown in Appendix B, with some approximations, it is possible to introduce effective (ensemble-averaged) radiative lifetimes for the minority carriers in the QDs and QW. The classical Shockley-Read-Hall theory allows introducing a corresponding lifetime parameter for the non-radiative recombination through trapping centres [Sze, 2004]. So, the following balance equation can be written for the minority carriers:

$$\frac{dn}{dt} = g - \frac{n_{QD}}{\tau_{QD}} - \frac{n_{QW}}{\tau_{QW}} - \frac{n_M}{\tau_{nr}} \quad (7.14)$$

where $n = n_M + n_{QD} + n_{QW}$ and g is the generation rate of electron-hole pairs. The (ensemble-averaged) radiative recombination lifetimes in the QDs and the QW are given by

$$\tau_{QW} = \tau_r^0 \left(\frac{m_e E_g}{\mu E'_g} \right) \frac{1}{K_{QW}^2} \exp \left[\frac{E_F + E_g - E_{QW}^h}{kT} \right], \quad (7.15)$$

$$\tau_{QD} = \tau_r^0 \left(\frac{E_g}{E''_g} \right) \frac{1}{K_{QD}^2} \exp \left[\frac{E_F + E_g - E_{QD}^h}{kT} \right], \quad (7.16)$$

where τ_r^0 is a material parameter given by equation B.16 of Appendix B, μ is the reduced electron-heavy-hole mass, $E''_g = E_g - E_{QD}^e - E_{QD}^h$ and K_{QW} and K_{QD} are the overlap integrals of the electron and hole envelope wave functions in the QW and QD, respectively. Note that these radiative recombination lifetimes depend on temperature due to the (temperature dependent) redistribution of the majority carriers between the different available states (QD, QW, M, and acceptor levels). The non-radiative lifetime in the matrix is given by the Shockley-Read-Hall expression [Fafard et al., 1999]

$$\tau_{nr} = \tau_{nr}^0 \left(1 + \frac{n_1}{p_0} \right), \quad (7.17)$$

$$\tau_{nr}^0 = \frac{1}{\Gamma N_t}, \quad (7.18)$$

where Γ is the trapping coefficient,

$$n_1 = N_C \exp\left(-\frac{E_t}{kT}\right), \quad (7.19)$$

where $(E_C - E_t)$ is the trap energy level and p_0 the equilibrium hole concentration in the matrix. Since $\tau_{nr}^0 \propto N_t^{-1}$, it can formally be written

$$\tau_{nr}^0 = \tau_r^0 \left(\frac{N^*}{N_t}\right), \quad (7.20)$$

where N^* is some quantity of the dimension of concentration that incorporates several material parameters and also Γ . It is a free parameter in our model. In principle, N^* can be determined by measuring the trap concentration and τ_{nr}^0 independently.

7.4.4 Steady-state excitation conditions

Equation (7.14) can be rewritten as

$$g\tau_r^0 = \xi n_M + \eta_{QD} n_{QD} + \eta_{QW} n_{QW}, \quad (7.21)$$

where ξ , η_{QD} and η_{QW} are functions of temperature and the (true) Fermi level,

$$\xi = \frac{\tau_r^0}{\tau_{nr}^0} \left(1 + \frac{n_1}{p_0}\right)^{-1}, \quad (7.22)$$

$$\eta_{QD} = \left(\frac{E_g''}{E_g}\right) \frac{1}{K_{QD}^2} \exp\left[-\frac{E_F + E_g - E_{QD}^h}{kT}\right], \quad (7.23)$$

$$\eta_{QW} = \left(\frac{\mu E_g'}{m_e E_g}\right) \frac{1}{K_{QW}^2} \exp\left[-\frac{E_F + E_g - E_{QW}^h}{kT}\right]. \quad (7.24)$$

Equations (7.8), (7.9), (7.10) and (7.21), (7.22), (7.23), (7.24) determine the quasi-Fermi level F as a function of T , concentration of traps, doping level and other parameters of the heterostructure.

The aim of getting an analytical solution as referred in the beginning of the model description was not achieved, and the equations cited above were numerically solved,

after obtaining E_F from equation (7.7).

The generation rate has been evaluated as

$$g = \frac{(1 - R) \alpha(\omega) W}{\hbar\omega}, \quad (7.25)$$

where W is the excitation (laser beam) power per unit area of the sample surface, ω is the incident photon frequency, and R is the reflectivity. If the excitation is not resonant, it implies an additional temperature dependence, since the absorption coefficient (at a given ω) depends on the temperature because of the variation of the bandgap energy. This has been taken into account in the following way:

$$\alpha(T) = \alpha_0 \sqrt{\frac{\hbar\omega - E_g(T)}{\hbar\omega - E_g(T_0)}}, \quad \hbar\omega \geq E_g(T), \quad (7.26)$$

where $\alpha_0 = \alpha(T_0)$ and T_0 is a temperature for which the absorption coefficient is known, e.g. RT. The Varshni empirical formula [Varshni, 1967] was used for the temperature dependence of E_g ,

$$E_g(T) = 1.519 - \frac{5.405 \times 10^{-4}T}{T + 204}. \quad (7.27)$$

7.5 Calculated results

The PL intensity is proportional to the thickness in which the photocarriers are generated, the electron concentration in the QDs or QW, and the radiative recombination probability.

By using the parameters from table 7.1, and taking the overlap integrals in equations (7.23) and (7.24) equal to unity, the PL intensities for the QDs and QW were calculated for different values of N_t (since N^* is a free parameter in our model, all the values of N_t used are proportional to the N^* values that were chosen rather arbitrarily), N_a , and excitation power (we found it convenient to express the latter in terms of $g_0\tau_r^0$ with g_0 corresponding to T_0). For a relatively high excitation power corresponding to the Ar⁺ laser, the variation of I_{QD} with T is shown in figure 7.8 for different trap concentrations ranging from 10^{13} to 10^{17} cm⁻³. Since this plot presents the PL intensities normalized by the maximum value in each case, we should note that the maximum PL intensity

Table 7.1: Material parameters used in the calculations.

electron effective mass m_e/m_0	0.067 ^a
heavy-hole effective mass m_{hh}/m_0	0.47 ^a
light-hole effective mass m_{lh}/m_0	0.08 ^a
GaAs absorption coefficient (at RT) (cm^{-1})	4×10^4 ($\lambda = 632 \text{ nm}$) ^b 2×10^5 ($\lambda = 488 \text{ nm}$) ^b
radiative lifetime τ_r^0 (s)	10^{-9} ^c
electron diffusion coefficient (cm^2s^{-1})	200 ^d
QD sheet density $N_{QD}^{(2D)}$ (cm^{-2})	10^{10}
E_t (eV)	0.65
N^* (cm^{-3})	10^{10}
E_a (eV)	0.03
E_{QD}^e (eV)	0.35 ^e
E_{QD}^h (eV)	0.20 ^e
E_{QW}^e (eV)	0.15 ^e
E_{QW}^h (eV)	0.05 ^e

^a[Basu, 1997]^b[Casey et al., 1975]^c[Fiore et al., 2000]^d[Stillmann et al., 1970]^e[Skolnick and Mowbray, 2004]

at a certain T decreases monotonically with N_t in this regime of high excitation power and high concentration of trapping centres. One can see from figure 7.8 that there is an exponential decrease in the QD emission intensity with the increase of the temperature above $\approx 200 \text{ K}$, as expected.

The calculations also show that the quenching appears at lower temperatures for higher defect concentrations. This is a typical situation corresponding to the most of the experimental data reported in the literature and also to sample NN4190 (see figure 7.4).

An increase in the excitation power apparently diminishes the quenching effect (see figure 7.9) because the electron's quasi-Fermi level is pushed up. However, this influence appears only above a certain threshold (note that the curves in figure 7.9, corresponding to $g_0\tau_r^0 = 10^{13}$ and 10^{14} cm^{-3} , practically coincide). The threshold is associated with the complete filling of the ground state of the QDs, as it can be seen from the inset in

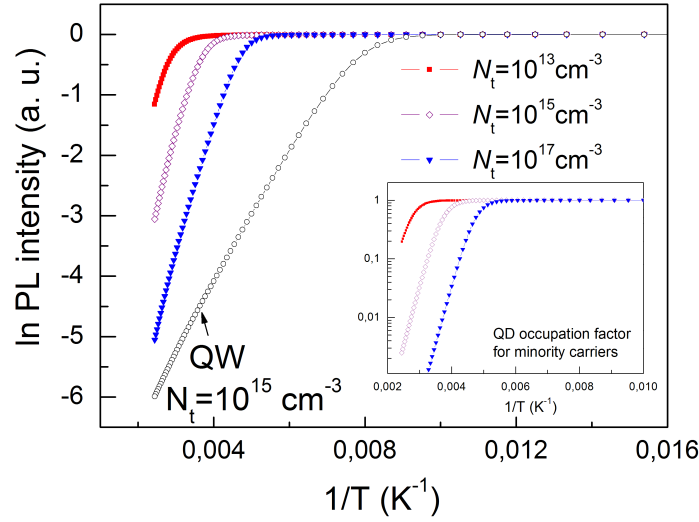


Figure 7.8: Temperature dependence of I_{QD} and I_{QW} calculated for several defect concentrations (as indicated on the plot) for the Ar^+ laser excitation with $g_0\tau_r^0 = 3 \times 10^{14} \text{ cm}^{-3}$. The acceptor concentration is $N_a = 10^{17} \text{ cm}^{-3}$. The inset shows the temperature dependence of the electron population of the QDs, $n_{QD}/\tilde{N}_{QD}^{(3D)}$.

figure 7.9.

The decay of I_{QD} and I_{QW} at higher temperatures is caused not only by the decrease of n_{QD} (see inset in figure 7.8) and n_{QW} in this regime, but also by the increase in the radiative recombination lifetimes (which occurs because of the transfer of holes from the QD and QW states back to the acceptors and to the barriers as the temperature increases). Accordingly, the quenching should be less pronounced for higher N_a , and this is confirmed by the calculations presented.

If the trap concentration is very low, around 10^{10} cm^{-3} , the situation is different. This is probably the case of the as-grown sample NN4184. The exponential decrease of the QD emission occurs at higher temperatures compared to the previous case, but the effect of the excitation power is the opposite (see figure 7.10). The quenching starts at lower temperatures for higher $g_0\tau_r^0$. In this regime, $n_{QD} \approx \tilde{N}_{QD}^{(3D)}$, and the quenching is almost entirely determined by the increase in τ_{QD} . The steady growth of I_{QD} taking place at intermediate temperatures is caused by the increase of the absorption coefficient (equation (7.26)). At the same time, the QW emission, very low compared to that of the QDs, raises with temperature because of the growth of n_{QW} . Recombination through traps plays little role in this regime. The maximum QD PL intensity grows with $g_0\tau_r^0$ slower than linearly above $\approx 10^{12} \text{ cm}^{-3}$ because

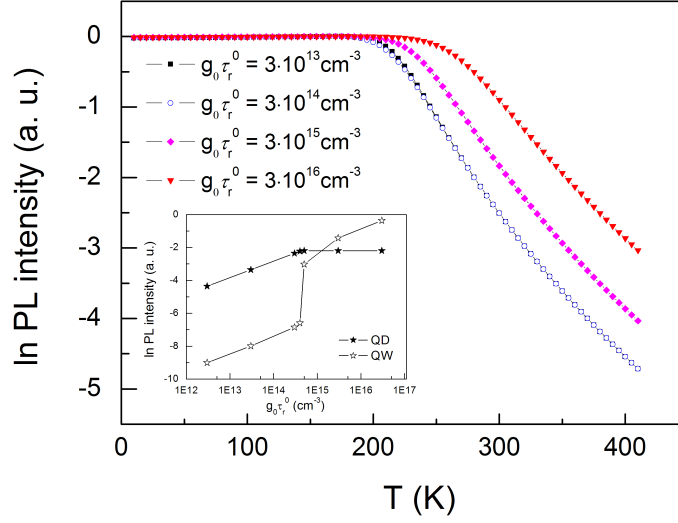


Figure 7.9: Temperature dependence of I_{QD} and I_{QW} calculated for different excitation intensities. The inset shows the dependence of the maximum values of the QD and QW emission intensities on the normalized excitation power density. $N_t = 10^{16} \text{ cm}^{-3}$ and $N_a = 10^{17} \text{ cm}^{-3}$.

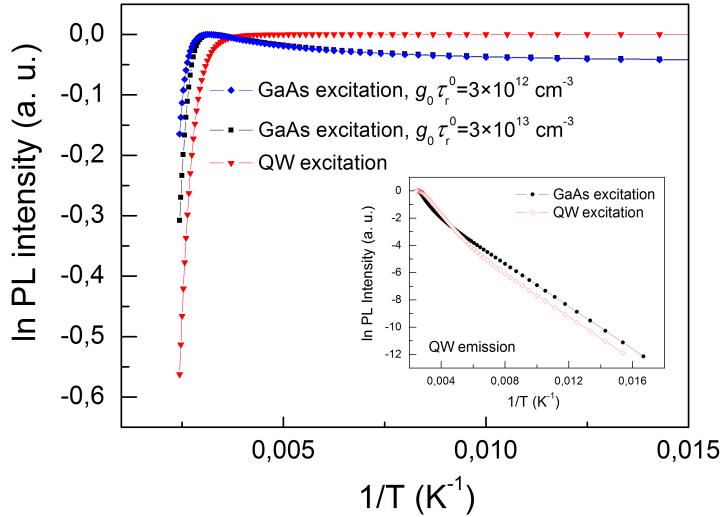


Figure 7.10: Temperature dependence of I_{QD} calculated for two different excitation powers of a He-Ne laser and for resonant excitation through the QW ($g_0 \tau_r^0 = 3 \times 10^{13} \text{ cm}^{-3}$). In all cases, $N_t = 10^{10} \text{ cm}^{-3}$ and $N_a = 10^{16} \text{ cm}^{-3}$. The inset shows the corresponding temperature dependence of the QW emission ($g_0 \tau_r^0 = 3 \times 10^{13} \text{ cm}^{-3}$).

the electrons start filling the QW. The apparent shift of the quenching temperature to a lower value, when $g_0\tau_r^0$ increases from 3×10^{12} to $3 \times 10^{13} \text{ cm}^{-3}$ (see figure 7.10), occurs due to the slightly different scaling of these two curves (the maximum appears at slightly different temperatures). The third curve in this plot corresponds to resonant excitation through the QW. As explained in the previous section, this corresponds to an effectively higher 3D concentration of the QDs. Therefore, for the same generation rate, the average population of the QDs is significantly lower than unity in this case where the photocarriers are created directly in the QW. The quasi-Fermi level lies below the bottom of the QW states and the quenching starts at lower temperatures because of the significant thermally activated escape of the electrons from the QDs to the QW. Indeed, this effect has been demonstrated experimentally in ref. [Baidus et al., 2005] by using a semiconductor laser for the PL excitation through the QW.

7.6 Discussion

The exponentially decreasing temperature dependence in the QD PL intensity, observed for sample TU3904 (see figure 7.2) and for sample NN4190 (see figure 7.4) is quite common and it has been modelled in several publications [Altieri et al., 2002; Brusafferri et al., 1996; Chang et al., 2005; Le Ru et al., 2003; Lee et al., 2008; Wasilewski et al., 1999; Wei et al., 2005] using simple functions of the type

$$I_{QD}(T) \propto \left[1 + \sum_i A_i \exp \left(-\frac{E_{ac}^{(i)}}{kT} \right) \right]^{-1}, \quad (7.28)$$

with some coefficients A_i and activation energies $E_{ac}^{(i)}$ attributed to different escape mechanisms of the minority carriers from the QDs [Hsieh et al., 2006; Le Ru et al., 2003; Lee et al., 2008; Sanguinetti et al., 1999, 2000]. This situation is represented by the calculated results of figures 7.8 and 7.9. It should be noted that a simple description is possible for the minority carrier concentration but not for the QD emission intensity. For example, the activation energy of the electron's escape, determined as

$$E_{ac} = k \frac{\partial \ln n_{QD}}{\partial (1/T)} \quad (7.29)$$

from the curves presented in the inset of figure 7.8, levels off at 175 meV, independently of the trap concentration. However, if we do the same for the $I_{QD}(T)$ dependences

shown in the same figure, we do not obtain any reasonable set of activation energies, because E_{ac} defined before varies continuously and never levels off. This is probably the reason why the activation energies determined using equation (7.29) can vary by an order of magnitude [Chahboun et al., 2006; Le Ru et al., 2003] for InAs/GaAs QDs with similar characteristics, and they are difficult to relate to the energies of the electron and hole states in the heterostructure. The PL quenching is not determined only by the minority carrier distribution between the different states, even though this mechanism is important indeed. In this regime, the QW emission is quenched even stronger than that of QDs (see figures 7.8 and 7.5 for calculated and experimental results, respectively).

The calculated results (figure 7.9) point to a significant growth of the quenching temperature for the same sample with increasing generation rate. An experiment with the as-grown sample NN4190 (see figure 7.6) was performed in order to verify this trend by measuring the temperature dependent PL spectra excited by the same 488 nm Ar⁺ laser line but with excitation power varying by three orders of magnitude. The normalized temperature dependence of the QD ground state emission changed with the excitation power in agreement with the theoretical prediction. In this case, the higher temperature stability of the QD emission under higher excitation is associated with the state filling effect.

In the case of heterostructures with low concentrations of trapping centres characteristic of the as-grown sample NN4184, for which the CCl₄ treatment during the growth was used, the PL intensity is almost constant up to RT [Baidus et al., 2005]. It is known that the introduction of CCl₄ during the growth leads to a *p*-type doping of the sample [Karpovich et al., 2004]. However, the major effect is the reduction of the concentration of InAs-rich dislocated clusters in the capping layer [Karpovich et al., 2004] and, consequently, the decrease of the concentration of non-radiative recombination centres. Indeed, the trends observed in figure 7.10 are different from those seen in figures 7.8 and 7.9, and correspond to the different temperature dependences experimentally observed for samples NN4184 and NN4190, respectively. We believe that the principal cause of the PL quenching observed for sample NN4190 and its suppression, i.e., shift to higher temperatures, for sample NN4184 is the different dominating recombination channel. The non-radiative recombination in the matrix starts to play a role when the concentration of deep traps increases above a certain threshold value. The capture of the minority carriers by the trapping centres occurs through the matrix (it was concluded in chapter 6 that photoexcited carriers can escape also via tunnelling from

excited QD states to radiation-induced defects below $T = 100$ K). In the framework of the model, we assume that defects are created predominantly in the GaAs matrix and do not include any excited QD states. Therefore, the escape channel via the latter is not considered here, although it should play a role at low temperatures. These statements are supported by two facts. First, the intentional introduction of defects in sample NN4184 by irradiation leads to the reappearance of the PL quenching at RT, but only if the irradiation fluence is high enough. Secondly, a systematic study of the PL spectra from InAs QD heterostructures with both p - and n -type doping of the GaAs barriers (both the capping and buffer layers) has been performed. The results (see figure 4.27) show a higher PL intensity for the p -type doped samples as compared to the n -type doped ones with the same layer thickness, although no direct effect of the doping type and level (in the range from 10^{16} – 10^{17} impurities/cm³ in the buffer layer) on the type of temperature dependence (see figure 4.29) of the PL intensity was found. The asymmetry, in terms of the QD PL intensity, between heterostructures that are different just by the type of doping is naturally explained by the deeper QD confinement potential for electrons compared to holes [Marko et al., 2005]. However, both n - and p -type samples may or may not, depending on other factors, show PL quenching at RT. Moreover, as explained in the end of the previous section, this can even depend on the wavelength of the radiation used to excite the emission [Baidus et al., 2005]. Of course, the doping level also influences the details of the temperature dependence of the PL intensity and even the shape of the spectra [Park et al., 2004] through the distribution of the majority carriers between the different states in the QDs and the barriers.

Through the effective thickness parameters w and \tilde{w} , the model presented in section 7.4 indirectly takes into account non-uniform distribution of the majority and minority carriers in the heterostructure. We believe that it can be useful for a qualitative understanding of more complex temperature dependences of the PL intensity observed for more sophisticated InAs/GaAs QD/QW heterostructures incorporating additional layers [Hsieh et al., 2006; Kryzhanovskaya et al., 2007] and the nontrivial effect of the CL thickness on the QD PL [Karpovich et al., 2004]. For instance, the two-stage exponential decrease of the QD PL intensity taking place in the irradiated samples (figures 7.2 and 7.5) can be understood in the framework of our model as being due to two different non-radiative recombination processes, with the second one associated with defects located directly in the QD/QW layer [Gonschorek et al., 2006]. This point has been discussed in chapter 6, following to the recombination and relaxation results ob-

served. However, the quantitative explanation of such features would probably require a more sophisticated modelling involving an explicit treatment of the drift, diffusion, capture, and thermal escape processes as well as taking into account the correlation effect in the electron and hole populations of the QDs [Grundmann and Bimberg, 1997; Sanguinetti et al., 2006].

7.7 Conclusions

This chapter is dedicated to the influence of defects on the temperature dependence of the PL in the dots-in-a-well structure. The deterioration of the emission properties with the increasing irradiation fluence is related to traps generated by the irradiation in the matrix, which reduce the overall concentration of the photoexcited carriers. A model describing the role of defects on the temperature dependence of the PL in the above-mentioned structure has been developed and experimentally tested.

It has been shown that defects in the GaAs matrix of a QD/QW heterostructure, created during the sample growth or through its irradiation, influence the temperature dependence of the QD PL intensity in a nontrivial way. By introducing non-radiative recombination pathways for photocarriers confined in the dots, the defects not only diminish the absolute value of the emission intensity but also affect the PL quenching temperature and its dependence on the type and intensity of the PL excitation. A rather simple model for the carrier statistics out of equilibrium is presented which reproduces quite well the experimentally established trends. The calculated results demonstrate that the QD PL quenching with increasing temperature is determined by two factors: a) minority carrier redistribution between the QDs, QW, and GaAs barriers and b) decrease in the radiative recombination rate related to the temperature dependence of the Fermi level of the majority carriers. It has been concluded that the simple exponential description of the PL temperature dependence usually applied in the literature is possible for the minority carrier concentration but not for the QD emission intensity.

Bibliography

Altieri, P., Gurioli, M., Sanguinetti, S., Grilli, E., Guzzi, M., Fiogeri, P., and Franchi, S. (2002). *The European Physical Journal B*, 28:157.

- Bacher, G., Schweizer, H., Kovac, J., and Forchel, A. (1991). *Physical Review B*, 43:9312.
- Baidus, N., Chahboun, A., Gomes, M., Vasilevskiy, M., Demina, P., Uskova, E., and Zvonkov, B. (2005). *Applied Physics Letters*, 87(5):053109.
- Basu, P. (1997). *Theory of Optical Processes in Semiconductors*. Clarendon, Oxford.
- Brusaferri, L., Sanguinetti, S., Grilli, E., Guzzi, M., Bignazzi, A., Bogani, F., Carraresi, L., Colocci, M., Bosacchi, A., Frigeri, P., and Franchi, S. (1996). *Applied Physics Letters*, 69:3354.
- Casey, H., Sell, D., and Wecht, K. (1975). *Journal of Applied Physics*, 46:250.
- Chahboun, A., Baidus, N., Demina, P., Zvonkov, B., Gomes, M., Cavaco, A., Sobolev, N., Carmo, M., and Vasilevskiy, M. (2006). *Physica Status Solidi A*, 203.
- Chang, K., Yang, S., Chuu, D., Hsiao, R., Chen, J., Wei, L., Wang, J., and Chi, J. (2005). *Journal of Applied Physics*, 97:083511.
- Fafard, S., Wasilewski, Z., Allen, C., Picard, D., Spanner, M., McCaffrey, J., and Piva, P. (1999). *Physical Review B*, 59:15368.
- Fiore, A., Borri, P., Langbein, W., Hvam, J., Oesterle, U., Hourdé, R., Stanley, R., and Illegems, M. (2000). *Applied Physics Letters*, 76:3431.
- Gonschorek, M., Schmidt, H., Bauer, J., Benndorf, G., Wagner, G., Cirlin, G., and Grundmann, M. (2006). *Physical Review B*.
- Grundmann, M. and Bimberg, D. (1997). *Physical Review B*, 55:9740.
- Hsieh, T.-P., Chiu, P.-C., Chyi, J.-I., Chang, H.-S., Chen, W.-Y., Hsu, T., and Chang, W.-H. (2006). *Applied Physics Letters*, 89:053110.
- Karpovich, I., Zvonkov, B., Baidus, N., Tikhov, S., and Filatov, D. (2004). *Trends in Nanotechnology Research*, chapter Tuning the energy spectrum of the InAs/GaAs Quantum dot structures by varying the thickness and composition of a thin double GaAs/InGaAs cladding layer, page 173. Nova Science, New York.
- Kryzhanovskaya, N., Gladyshev, A., Blokhin, S., Vasil'ev, A., Semenova, E., Zhukov, A., Maximov, M., Ledentsov, N., and Ustinov, V. (2007). *International Journal of Nanoscience*, 6:287.

- Le Ru, E., Fack, J., and Murray, R. (2003). *Physical Review B*, 67:245318.
- Lee, E.-K., Tsybeskov, L., and Kamins, T. (2008). *Applied Physics Letters*, 92:033110.
- Marko, I., Massé, N., Sweeney, S., Andreev, A., Adams, A., Hatori, N., and Sugawara, M. (2005). *Applied Physics Letters*, 87:211114.
- Park, Y., Park, Y., Kim, K., Shin, J., Song, J., Lee, J., and Yoo, K.-H. (2004). *Journal of Crystal Growth*, 271:385.
- Polimeni, A., Patané, A., Henini, M., Eaves, L., and Main, P. (1999). *Physical Review B*, 59:5064.
- Sanguinetti, S., Colombo, D., Guzzi, M., Grilli, E., Gurioli, M., Scravalli, L., Frigeri, P., and Franchi, S. (2006). *Physical Review B*, 74:205302.
- Sanguinetti, S., Henini, M., Alissi, M., Capizzi, M., Frigeri, P., and Franchi, S. (1999). *Physical Review B*, 60:8276.
- Sanguinetti, S., Padovani, M., Gurioli, M., Grilli, E., Guzzi, M., Vinattieri, A., Colocci, M., Frigeri, P., and Franchi, S. (2000). *Applied Physics Letters*, 77:1307.
- Skolnick, M. and Mowbray, D. (2004). *Physica E*, 21:155.
- Stillmann, G., Waife, C., and Dimmock, J. (1970). *Journal of Physics and Chemistry of Solids*, 31:1199.
- Sze, S. (2004). *Physics of Semiconductor Devices*. Wiley.
- Varshni, Y. (1967). *Physica (Amsterdam)*, 34:1499.
- Wasilewski, Z., Fafard, S., and McCaffrey, J. (1999). *Journal of Crystal Growth*, 201:1131.
- Wei, Z., Xu, S., Duan, R., Li, Q., Wang, J., Zeng, Y., and Lin, H. (2005). *Journal of Applied Physics*, 98:084305.

Chapter 8

Conclusions and Outlook

8.1 Summary

In this thesis, a study of radiation-induced defects in semiconductor quantum-size structures is presented. Strained III-V QDs in the (In,Ga)As/GaAs system, fabricated using the Stranski-Krastanow growth mode in connection with self-organization phenomena, have been chosen as the main research object. Irradiations with electrons and protons were undertaken on various types of samples, and differences have been pointed out.

In chapter 1 the problem is presented and the topic chosen for this work justified. This chapter includes a brief description of the structure of the thesis.

In chapter 2 the state of the art is presented. The properties of the InAs/GaAs QD heterostructures are reviewed, highlighting the differences/similarities between QDs, bulk semiconductors and atoms. The main physical properties of GaAs and InAs are also presented in this chapter. The density of states as a function of the structure's dimensionality is here briefly discussed. The different possible band offsets for semiconductor heterostructures are presented and discussed. A second part of this chapter is related to radiation defects in III-V semiconductors, including the mechanisms of energy deposition in elastic and inelastic collisions, and the influence of radiation-induced defects on the device performance. Specific issues related to irradiation of quantum-size structures are then presented. Finally, the mechanisms of electron and proton interaction with matter are discussed.

Chapter 3 is devoted to the sample growth methods and experimental techniques.

Self-organization phenomena in crystal structures are discussed, and some peculiarities of the InGaAs system approached. The Stranski-Krastanow growth mode and the MOCVD technique are described as well as the influence of the temperature and amount of deposited material on the sample quality. Finally, the facilities used to grow the samples studied in this work are briefly referred. A second part of this chapter presented the experimental techniques used to characterize the samples under study, namely PL, PLE, TRPL and resonantly excited PL. Different schemes of the experimental equipment are also included.

The characterization of the samples prior to irradiation is presented and discussed in chapter 4. Samples having laser structures, samples with non-uniform WL thickness, samples with different cap layer thicknesses and samples subjected to a CCl_4 treatment during the growth were investigated. The work performed with these samples allowed to study a set of properties that were expected to change upon irradiation. The differences between QDs and QWs and the influence of the WL thickness, of the cap layer thickness, and of the defect concentration in the as-grown state are analysed and discussed.

It is Chapter 5 in which the radiation hardness of the QD heterostructures is presented. The influence of 2 MeV electron and 2.4 MeV proton irradiation on the PL in InAs/GaAs QW and QD structures is compared. An enhanced radiation hardness of the QDs has been established and related to the different influence of defects created inside the QWs and QDs and in the adjacent GaAs barrier within a tunnelling distance. The methodology of presenting the PL intensity versus irradiation fluence is described. The influence of radiation-induced defects on the PL emission of samples with non-uniform WL thickness is also included. The different possible mechanisms of radiation hardness are discussed.

In chapter 6, the TRPL of QD and QW heterostructures of InGaAs/GaAs subjected to high-energy electron and proton irradiation is investigated in order to better understand the influence of defects on the relaxation of photoexcited charge carriers. An interaction of confined carriers with radiation-induced defects inside or near the QDs was observed. It has been concluded that the QDs have the ability, due to strain fields, of expulsing mobile defects into the matrix. Thus, the ground state of the confined carriers/excitons remains essentially undamaged up to rather high concentrations of defects in the matrix due to the weak penetration of the wave function into the barrier.

The influence of radiation defects on the PLE of InGaAs/GaAs QDs heterostructures

has been investigated to further deepen the understanding of the carrier relaxation and escape processes. For the sample configuration used (two AlGaAs diffusion barriers surrounding the QD plane), the main part of the carrier loss due to the introduced radiation damage occurs in the dots, even for the excitation of the GaAs barrier. The tunnel escape of carriers to neighbouring defects occurs out of the excited states having a stronger penetration of the wave function into the matrix.

The results presented in chapter 7 show that defects in the GaAs matrix of a dots-in-a-well heterostructure, created during the sample growth or through its irradiation, influence the temperature dependence of the QD PL intensity in a nontrivial way. By introducing non-radiative recombination pathways for carriers confined in the dots, the defects not only diminish the absolute value of the emission intensity, but also affect the PL quenching temperature and its dependence on the type and intensity of the PL excitation. The developed model includes the analysis of carrier statistics for the heterostructure in equilibrium and under illumination; analysis of possible recombination channels, and analysis of steady-state excitation conditions. The model reproduces quite well the experimentally established trends. The calculated results demonstrate that the QD PL quenching with increasing temperature is determined by two factors: minority carrier redistribution between the QDs, QW, and GaAs barriers and decrease in the radiative recombination rate related to the temperature dependence of the Fermi level of the majority carriers.

8.2 Outlook

Naturally, when an experimentally driven work like this is started, several competing pathways can be followed. The choice of the right one is not always an easy task. Which experimental technique to use, or is the chosen technique the one that will give the answer to the question posed, are questions that sometimes arise.

An obvious way to go in the future is an extension of the research to emerging QD-based devices. Besides, a lot of fundamental questions regarding the properties, evolution and interaction of defects confined in quantum-size heterostructures in comparison to those created in bulk materials remain for the future research.

Appendix A

Spatial distribution of the minority carriers

In order to introduce an appropriate thickness of the effective homogeneous system to which the statistical relations of section 7.4 should be applied out of equilibrium, let us consider the distribution of the minority carriers in the heterostructure when its surface is impinged by photons with $\hbar\omega > E_g$. Neglecting for a while the recombination through the QW and QDs, the electrons in the GaAs matrix are described by

$$\frac{\partial n_M}{\partial t} = g + D_n \frac{\partial^2 n_M}{\partial z^2} - \frac{n_M}{\tau_{nr}}, \quad (\text{A.1})$$

where the z axis has been chosen perpendicular to the surface, $g = G \exp(-\alpha z)$ is the generation rate and D_n is the diffusion coefficient. Under stationary conditions, equation A.1 can be rewritten as

$$n_M'' - L_n^{-2} n_M + \left(\frac{G}{D_n} \right) \exp(-\alpha z) = 0 \quad (\text{A.2})$$

where $L_n = \sqrt{D_n \tau_{nr}}$ is the diffusion length. By solving equation A.2 with the boundary conditions $n_M'(0) = 0$ and $n_M(\infty) = 0$ one obtains

$$n_M(z) = \frac{G \tau_{nr}}{1 - \alpha^2 L_n^2} \left[\exp(-\alpha z) - (\alpha L_n) \exp\left(-\frac{z}{L_n}\right) \right]. \quad (\text{A.3})$$

By using equation A.3, we can introduce the effective thickness of the layer where the minority carriers are generated,

$$\tilde{w} = \frac{1}{n_M(0)} \int_0^\infty n_M(z) dz = \frac{1}{\alpha} + L_n \quad (\text{A.4})$$

Appendix B

Radiative recombination rates

This calculation was performed and kindly made available by Prof. Dr. M. Vasilevskiy, University of Minho.

This appendix intends to show how the radiative recombination rates can be expressed in the simple form of equation 7.14 and deduce the relations 7.16 and 7.15 for the radiative lifetimes. The probability of spontaneous emission (per second) due to interband transitions is given by [Basu, 1997]

$$W_e(\omega) = 2 \left(\frac{2\pi e}{m_0 \eta} \right)^2 \frac{1}{V\omega} \frac{2P^2 K^2}{3} \sum_{\vec{k}} \delta \left[E_c(\vec{k}) - E_v(\vec{k}) - \hbar\omega \right] \times f_e \left[E_c(\vec{k}) \right] f_h \left[E_v(\vec{k}) \right] \quad (\text{B.1})$$

where m_0 is the free electron mass, η is the refraction index, V is the volume, P is the (Kane's) interband transition matrix element, $K = \int_V \Psi_h \Psi_e d\vec{r}$ is the overlap integral of the electron and hole envelope wave functions, $E_c(\vec{k})$ and $E_v(\vec{k})$ denote the electron energies for the conduction and valence bands, and f_e and f_h are the electron and hole distribution functions, respectively. If a nanostructure is considered, (e.g. with a QW or a QD), \vec{k} should be replaced by appropriate quantum numbers. For example, for a QW,

$$E_c(\vec{k}_{||}) = \frac{\hbar^2 k_{||}^2}{2m_e} - E_{QW}^e \quad (\text{B.2})$$

$$E_v(\vec{k}_{||}) = \frac{\hbar^2 k_{||}^2}{2m_{hh}} + E_{QW}^h - E_g \quad (\text{B.3})$$

Within the approximation using quasi-Fermi levels for electrons and holes (F_e and F_h),

$$f_e \left[E_c(\vec{k}) \right] = f_0 \left[E_c(\vec{k}), F_e \right], \quad (\text{B.4})$$

$$f_h \left[E_v(\vec{k}) \right] = 1 - f_0 \left[E_v(\vec{k}), F_h \right], \quad (\text{B.5})$$

where f_0 is the Fermi-Dirac function. By assuming that $f_0 \left[E_c(\vec{k}), F_e \right] \approx 1$ and $f_0 \left[E_v(\vec{k}), F_h \right] \approx 0$ (weak excitation), it follows

$$f_e \left[E_c(\vec{k}) \right] f_h \left[E_v(\vec{k}) \right] \cong \exp \left[\frac{F_e - E_c(\vec{k}) - F_h + E_v(\vec{k})}{kT} \right]. \quad (\text{B.6})$$

By introducing $E(\vec{k}) = E_c(\vec{k}) - E_v(\vec{k})$, making the standard replacement

$$2 \sum_{\vec{k}} \rightarrow V \int dE g_j(E) \quad (\text{B.7})$$

and performing the integration in equation B.1, one obtains

$$W_e(\omega) = \frac{8\pi^2 e^2 P^2 K^2}{3m_0^2 \eta^2 \omega} g_j(\hbar\omega) \exp \left(\frac{F_e - F_h - \hbar\omega}{kT} \right), \quad (\text{B.8})$$

where g_j is the joint (electron-hole) density of states. For a QW,

$$g_j(E) = \frac{1}{w} \frac{\mu}{\pi \hbar^2} \theta(E - E'_g), \quad (\text{B.9})$$

where μ is the electron-hole reduced mass, E'_g is the effective gap in the QW and θ the Heaviside step function. Similarly, for a QD,

$$g_j(E) = N_{QD}^{(3D)} \delta(E - E''_g). \quad (\text{B.10})$$

The recombination rate is obtained by integrating $W_e(\omega)$ given by equation B.8 over all possible photon frequencies and subtracting the part compensated by the thermal generation of electron-hole pairs,

$$\tilde{R} = \frac{8\pi^2 e^2 P^2 K^2 V}{3m_0^2 \eta^2} \int_0^\infty \frac{g_j(\hbar\omega)}{\omega} \exp \left(-\frac{\hbar\omega}{kT} \right) \times \left[\exp \left(\frac{F_e - F_h}{kT} \right) - 1 \right] \rho_0(\hbar\omega) d(\hbar\omega), \quad (\text{B.11})$$

where

$$\rho_0(\hbar\omega) = \frac{\omega^2 \eta^3}{\pi^2 \hbar c^3} \quad (\text{B.12})$$

is the photon density of states. By assuming the Boltzmann statistics, equation B.11

simplifies to

$$\tilde{R} = \gamma(np - n_0p_0)V, \quad (\text{B.13})$$

where n and p are the electron and hole concentrations out of equilibrium, and n_0 and p_0 are those at equilibrium, and

$$\gamma = \frac{8\eta e^2 P^2 K^2}{3m_0^2 \hbar^2 c^3 n_0 p_0} \int_0^\infty (\hbar\omega) g_j(\hbar\omega) \exp\left(-\frac{\hbar\omega}{kT}\right) d(\hbar\omega). \quad (\text{B.14})$$

For a heavily doped semiconductor, e.g. of p -type, it is possible to introduce a recombination lifetime by writing the recombination rate in the following way:

$$\frac{\tilde{R}}{V} \cong \gamma \Delta n p_0 = \frac{\Delta n}{\tau_r} \cong \frac{n}{\tau_r}, \quad (\text{B.15})$$

where $\Delta n = n - n_0$, $p \approx p_0$ and $\tau_r = \frac{1}{\gamma p_0}$. Substituting into equation B.14 the joint density of states given by equations B.9 and B.10, we obtain the expressions 7.15 and 7.16 for the QW and QDs, respectively, with

$$\frac{1}{\tau_r^0} = \frac{8\eta e^2 P^2 E_g}{3m_0^2 \hbar^2 c^3}. \quad (\text{B.16})$$

Bibliography

Basu, P. (1997). *Theory of Optical Processes in Semiconductors*. Clarendon, Oxford.

